

Contents

2	1 Introduction	3
3	2 Pixel detectors	5
4	2.1 Signal formation	5
5	2.2 Charge Coupled Devices	7
6	2.3 Hybrid pixels	7
7	2.4 CMOS MAPS and DMPAS	9
8	2.4.1 DMAPS: large and small fill factor	10
9	2.4.2 A modified sensor	11
10	2.5 Analog front end	13
11	2.5.1 Preamplifier	13
12	2.6 Readout logic	14
13	3 Use of pixel detectors	17
14	3.1 Tracking in HEP	17
15	3.1.1 Hybrid pixels at LHC and at SuperKEKB	18
16	3.1.2 First attempts to MAPS	21
17	3.2 Other applications	23
18	3.2.1 Applicability to FLASH radiotherapy	23
19	4 TJ-Monopix1	28
20	4.1 The sensor	29
21	4.2 Front end	31
22	4.2.1 ALPIDE-like	32
23	4.3 Readout logic	33
24	5 Arcadia-MD1	37
25	5.1 The sensor	37
26	5.2 Readout logic and data structure	38
27	5.2.1 Matrix division and data-packets	38
28	6 Characterization	41
29	6.1 TJ-Monopix1 characterization	41
30	6.1.1 Threshold and noise: figure of merit for pixel detectors	41
31	6.1.2 Linearity of the ToT	45
32	6.1.3 Calibration of the ToT	47
33	6.1.4 Changing the bias	50
34	6.1.5 Measurements with radioactive sources	51

35	6.1.6	Dead time measurements	54
36	6.2	ARCADIA-MD1 characterization	57
37	7	Test beam measurements	60
38	7.1	Apparatus description	60
39	7.1.1	Accelerator	61
40	7.1.2	Mechanical carriers	62
41	7.2	Measurements	62
42	7.2.1	MIP spectrum using cosmic rays as source	67
43	A	Pixels detector: a brief overview	68
44	A.1	Radiation damages	68
45	Bibliography		71
46	Characterization of monolithic CMOS pixel sensors for charged particle detectors and		
47	for high intensity dosimetry		

⁴⁸

Chapter 1

⁴⁹

Introduction

⁵⁰ Since the 1980s, when the fabrication of device with very small electrodes (50-100 μm)
⁵¹ became a practical possibility, pixel detectors have been widely employed for imaging and
⁵² tracking charged particles in the vertex region of experiments at accelerators. Thanks to
⁵³ their excellent spatial resolution, today even better than 10 μm , they allow for true three
⁵⁴ dimensional space-point determination even at high particle fluxes and in particular for
⁵⁵ the identification of secondary vertices of short-lived particles such as τ and B mesons.
⁵⁶ Requirement imposed by accelerators are stringent and they will become even more so
⁵⁷ with the increase of luminosity; in this scenario CMOS Monolithic Active Pixel Sensors
⁵⁸ (MAPS), based on the technology of CMOS cameras, are being developed to improve
⁵⁹ the performance of the hybrid pixel detectors, which currently constitute the state-of-art
⁶⁰ for large scale pixel detector, in particular by reducing the amount of material, power
⁶¹ consumption and pixel dimension. Indeed, while hybrid pixels are made by two parts, the
⁶² sensor and the electronics, welded together through microconnections, the MAPS integrate
⁶³ them all on the same wafer.

⁶⁴ Experiments such as ALICE at LHC and STAR at RHIC have already introduced the
⁶⁵ CMOS MAPS technology in their detectors. ALICE Tracking System (ITS2), upgraded
⁶⁶ during the LHC long shut down in 2019-20, was the first large-area ($\sim 10 \text{ m}^2$) silicon vertex
⁶⁷ detector based on CMOS MAPS. Thanks to the reduction of the material budget, ITS2,
⁶⁸ which uses the ALPIDE chip developed by ALICE collaboration, obtained an amazing im-
⁶⁹ provement both in the position measurement and in the momentum resolution, improving
⁷⁰ the efficiency of track reconstruction for particle with very low transverse momentum (by
⁷¹ a factor 6 at $p_T \sim 0.1 \text{ GeV}/c$). Further advancements in CMOS MAPS technology are
⁷² being aggressively pursued for the ALICE ITS3 and the Belle II vertex detector upgrades
⁷³ (both foreseen around 2026-27), and by the R&D53 collaboration for the upgrade at HL-
⁷⁴ LHC, with the goals of further reducing the sensor thickness and improving the readout
⁷⁵ speed of the devices, while keeping power consumption at a minimum.

⁷⁶ Beside tracking, the development of pixel detectors is a very active field with many
⁷⁷ applications: a noteworthy example of detector originally used in particle physics and later
⁷⁸ employed for medical imaging, in space detectors and for art authentication, is Medipix,
⁷⁹ a hybrid system developed at CERN within the Medipix collaboration. Among medical
⁸⁰ applications, a possible use of CMOS MAPS could be in dosimetry: in the last few years
⁸¹ the search of radiotherapy oncological treatments with high intensity beams (FLASH
⁸² mode) is requiring new dosimeters, both for the therapies as well as new beam-monitors
⁸³ (especially for focused very high energy electron beams), which are capable of deal with

84 extreme dose rate (up to 40 Gy/s).

85 I have studied the characteristics of two ALPIDE-like CMOS MAPS chips and tested
86 them under different front end configuration. The first chip, the TJ-Monopix1 from the
87 Monopix series, is a TowerJazz MAPS fabricated in 180 nm CMOS technology with an
88 active area of $1 \times 2 \text{ cm}^2$ (448×224 pixels) and is one of the prototypes for the Belle II vertex
89 detector upgrade. The second chip, called Main Demonstrator-1, has an active area of
90 $1.28 \times 1.28 \text{ cm}^2$ (512×512 pixels) is produced by LFoundry in 110 nm CMOS technology
91 and designed by the ARCADIA (Advanced Readout CMOS Architectures with Depleted
92 Integrated sensor Arrays) group; it is intended to be a general purpose device with possible
93 use in medical scanners, space experiments, future lepton colliders and also possibly X-ray
94 applications with thick substrates. The main differences between the two chips are in the
95 output signal type and in the readout sequence of the matrix. Concerning the former,
96 TJ-Monopix1 returns an analog output information, that is the time over threshold of the
97 pulse, which can be related with the charge released by the particle in the sensor, while
98 MD1 returns only a digital information; regarding the latter, instead, TJ-Monopix1 has
99 a completely sequential readout, while MD1 roughly combines the information of the hits
100 before the readout in order to reduce the data transmission time.

101 I have set up the test systems for the two chips in the INFN clean laboratories and char-
102 acterized the devices electrically and with radioactive sources in terms of threshold, noise,
103 dead time and analog response. The mean minimum stable threshold evolved through
104 different generation of chips and nowadays it is less than 500 e^- , allowing thinner sensors
105 with smaller signals: TJ-Monopix1 has proven to be in agreement with this trend, having
106 a threshold of $\sim 400 \text{ e}^-$, to be compared with the 2000 e^- signal expected for a minimum
107 ionizing particle in an epitaxial layer of $25 \mu\text{m}$. Moreover, since one of the main challenges
108 of MAPS are the differences between pixels due to process parameters variation across
109 the wafer, which make the sensor response nonuniform, I have measured the threshold
110 and noise dispersion across the matrix, which I found to be 40 e^- and 2 e^- respectively. I
111 have also studied the response of the analog signal recorded by TJ-Monopix1, that is the
112 time over threshold, and performed a calibration of its absolute value using a Fe55 X-ray
113 source. All these measurements are important to verify the design parameters of the chip
114 and to validate the chip simulation.

115 As conclusion of the measurement campaign, we have tested TJ-Monopix1 at very
116 high intensity using the electron beam of the new ElectronFlash accelerator designed for
117 both medical research and R&D in FLASH-radiotherapy and recently installed at Santa
118 Chiara hospital in Pisa. I have participated in the design of the setup needed for testbeam
119 measurement and I am currently working on the analysis of the data collected.

₁₂₀ **Chapter 2**

₁₂₁ **Pixel detectors**

₁₂₂ Pixel detectors are semiconductor detectors which are segmented in two dimensions: this
₁₂₃ distinguish them from the strip detectors, such that a single plane of detector already
₁₂₄ provides both the coordinates of impact of the detected particle. Their operation is based
₁₂₅ on the p-n junction (fig. 2.1). A p-n junction is built by bringing in contact two n
₁₂₆ and p doped silicon crystals. At the boundary, recombination of both charge carriers
₁₂₇ occurs forming a region, the depletion zone, which is free of charge carriers. The charged
₁₂₈ donors⁺ and acceptor⁻, that remain ionised in the n-type and p-type regions, features a
₁₂₉ space charge and create an electric field across the junction, causing a drift current in the
₁₃₀ opposite direction to the diffusion one, through which the junction reaches an equilibrium
₁₃₁ state. Assuming a constant space change, the electric field is linear and reach a maximum
₁₃₂ at the boundary of the *p* and *n* layers.

₁₃₃ **2.1 Signal formation**

₁₃₄ When a charged particle passes through a pixel and loses energy by ionization only a
₁₃₅ part of that energy is used to generate electron-hole pairs, since another part is used for
₁₃₆ other processes, as lattice excitation. The average energy needed to create a pair at 300 K
₁₃₇ in silicon is $w_i = 3.65 \text{ eV}$, that is more than the mean ionization energy because of the
₁₃₈ interactions with phonon, since for a minimum ionizing particle (MIP) the most probable
₁₃₉ value (MPV) of charge released in the semiconductor is $0.28 \text{ keV}/\mu\text{m}$, hence the number
₁₄₀ of electrons-vacuum pairs is:

$$\langle \frac{dE}{dx} \rangle \frac{1}{w_i} \sim 80 \text{ e/h} \sim \frac{1.28 \cdot 10^{-2} fC}{\mu\text{m}} \quad (2.1)$$

₁₄₁ Because of the splitting of the energy depositon between the two different processes, the
₁₄₂ number $N_{e/h}$ of couples generated undergoes fluctuations that usually follow a Poisson
₁₄₃ distribution; thus the fluctuations of $N_{e/h}$ is equal to $\sigma_{e/h} = \sqrt{N_{e/h}}$. Under the constraint
₁₄₄ of complete absorption of a particle, the energy resolution improves of a factor \sqrt{F} , where
₁₄₅ F is called the Fano factor and determines the ultimate limit of energy resolution for
₁₄₆ semiconductors. F is a function of the material and temperature and for silicon is equal
₁₄₇ to ~ 0.115 .

₁₄₈ In order to avoid a loss signal, it is fundamental that pairs e/h are produced in the
₁₄₉ depleted region of the semiconductor, where the probability of recombination with charge
₁₅₀ carriers is low. For this reason pixel detectors are commonly reverse biased: a positive
₁₅₁ bias is given to the *n* electrode and a negative to the *p* in order to grow the depletion zone

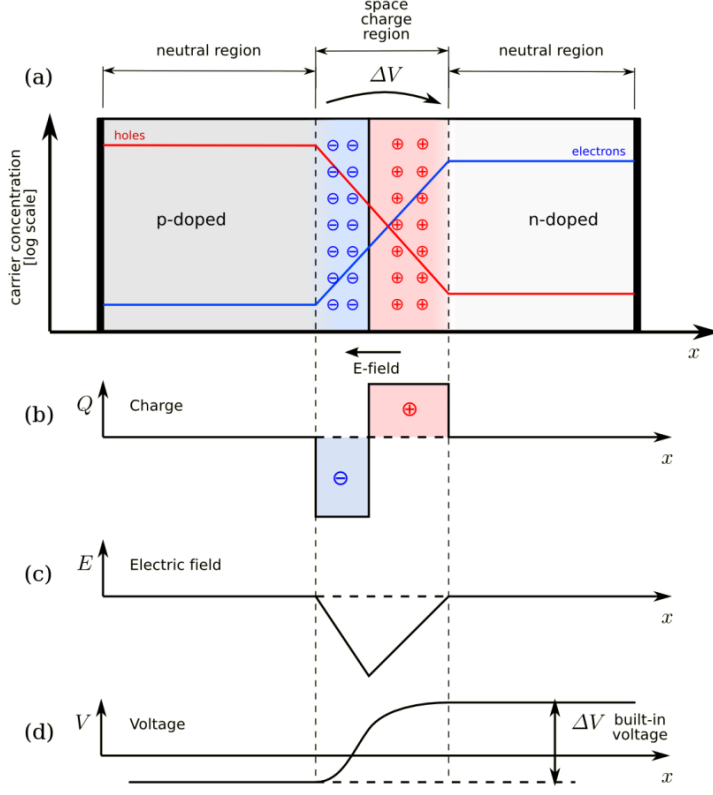


Figure 2.1: The structure of a p-n junction. (a) structure, (b) space charge density, (c) electric field distribution and (d) potential distribution.

in the epitaxial layer within the bulk. The width of the depletion region depends on the external bias V_{ext} , the resistivity ρ and also with the dopant:

$$d_n \sim 0.55 \sqrt{\frac{\rho}{\Omega cm} \frac{V_{ext}}{V}} \mu m \quad d_p \sim 0.32 \sqrt{\frac{\rho}{\Omega cm} \frac{V_{ext}}{V}} \mu m \quad (2.2)$$

Thus, high resistivity wafers ($100 \Omega cm - k\Omega cm$) are typically preferred because they allow bigger depletion zone with smaller voltage bias.

The charges created within the sensor are separated by an electric field and collected at their respective electrodes (p for holes and n for electrons)¹; by the drift of these charges, a signal i_e is generated on the electrode e as stated by the Shockley-Ramo's theorem:

$$i_e(t) = -q v(t) E_{WF,e} \quad (2.3)$$

where $v(t)$ is the instantaneous velocity of the charge q and E_{WF} is the weighting field, that is the field obtained biasing the electrode e with 1V and all the others with 0V. The drift velocity of the charge depends on the electric field and on the mobility of the particle:

$$v = \mu(E) E \quad (2.4)$$

where $\mu(E)$ is a function of the electric field and is linear in E only for small E : at higher values the probability of interactions with optical phonons increases, the mobility drops

¹Even if in principle both the electrode can be used to read the signal, for pixel detectors, where the number of channel and the complexity of readout are high, only one is actually used. In strip and pad detectors, instead, is more common a dual-side readout

164 and this leads to a saturation of the velocity (fig. 2.2). Typical values for electrons and
 165 holes mobility in silicon at room temperature are $\mu_n \sim 1450 \text{ cm}^2/\text{Vs}$, $\mu_h = 500$.

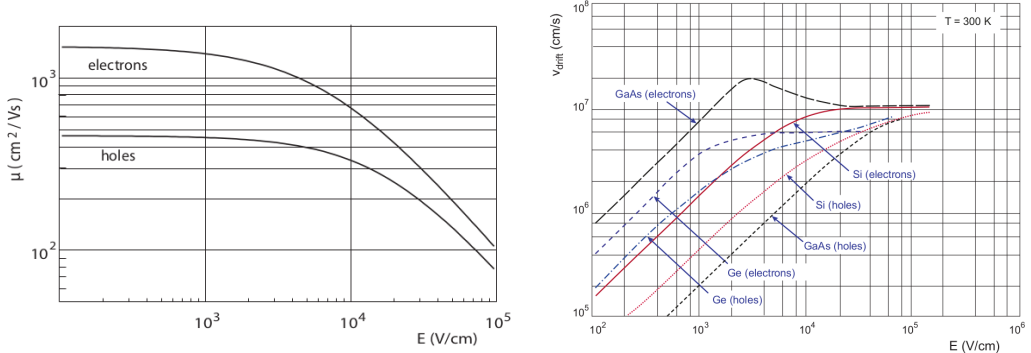


Figure 2.2: (a) Dependence of the mobility on the electric field. (b) Drift velocity at room temperature in different semiconductors

166 2.2 Charge Coupled Devices

167 In CCDs the charge is created in a very thin active epitaxial layer (typically 10 μm ,
 168 maximally about 30 μm) and then locally stored in a potential minimum which is created
 169 by a MOS structure. The size of the CCD cells is typically in the range 10 μm to 20 μm
 170 such that spatial resolutions are of the order of a few micrometres. The collected charges
 171 are moved stepwise from electrode to electrode (thus so called 'bucket chain') by applying a
 172 potential with a clock with frequency of \sim MHz; despite of such high frequency, the readout
 173 chain is completely sequential and this makes the entire process comparatively slow (tens
 174 of ms). A particular type of CCD, the pnCCDs, are typically used to detect low energy
 175 (<10 keV) x-ray photons for their homogeneous spatial detection efficiency of photons.
 176 The pnCCDs have a sideward depletion similar to silicon drift chambers that makes the
 177 electric field stronger, compared with the normal CCDs. The pnCCDs designed for photon
 178 imaging are often fabricated with high Z materials, to increase absorption efficacy.

179 2.3 Hybrid pixels

180 Hybrid pixels, which currently are the state-of-art technology for large scale pixel detectors
 181 in most particle physics experiments, are made of two parts welded together through
 182 microconnection (bump bond): the sensor and the electronics (fig. 2.3a). They provide a
 183 practical system where the sensor and the ASIC (application specific integrated circuit)
 184 can be optimized separately, which makes them really fast, capable of handling with rate
 185 up to GHz. However a disadvantage of hybrid pixels is that they must be connected before
 186 testing. For reasons related with the historical development, the n⁺-in-n sensors were the
 187 first to be used; they demanded double-sided processing which guarantees the detector
 188 functionality both before and after the type inversion of the n⁻ doped bulk into p-type
 189 after high quantity of radiation. The pn-diode is initially on the unstructured backside
 190 of the sensor, while after, the depletion zone grows from the electrode side into the bulk.
 191 This ensures that the signal can be sensed on the pixels even if the substrate is no longer
 192 fully depleted, even though the bias voltage required for a sufficient depletion increases,

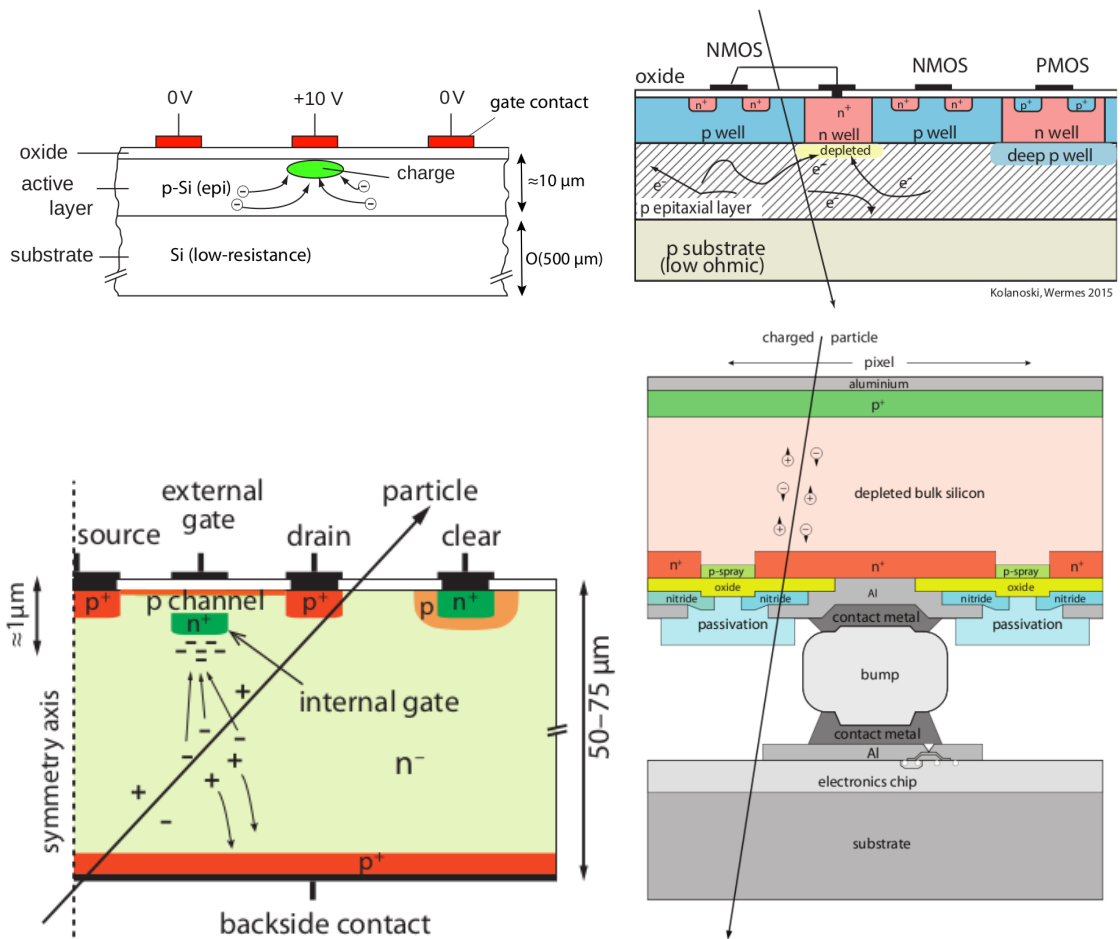


Figure 2.3: Concept cross-section of hybrid pixel (a) and of a DEPFET (b)

193 liming the detector lifetime up to a few years. With the availability of high quality p-
194 substrate material ($\gtrsim 2 \text{ k}\Omega\text{cm}$) the fabrication of n-in-p type sensors, which does not invert
195 anymore, became the preferred choise leading also a huge advance in cost reduction due
196 to no more need of double sided. However, the particular and sophisticated procedure to
197 bond sensor and ASIC makes them difficult to produce, delicate (especially when exposed
198 to high levels of radiation) and also expensive.

199 DEPFET are the first attempt towards the integration of the front end (FE) on the
200 sensor bulk: they are typically mounted on a hybrid structure but the sensor also in-
201 tegrates the first amplification stage. Each pixel implements a MOSFET (metal-oxide-
202 semiconductor field-effect transistor) transistor (a p-channel in fig. 2.3b): a hole current
203 flows from source to drain which is controlled by the external gate and the internal gate
204 together. The internal gate is made by a deep $n+$ implant towards which electrons drift
205 after being created in the depletion region; the accumulation of electrons in the region
206 underneath the n implant changes the gate potential and controls the transistor current;
207 the removal of the signal charge from the internal gate is called "Clear". DEPFET typ-
208 ically have a good S/N ratio: this is principally due to the amplification on-pixel, which
209 guarantees any charge losses, and to the large depletion region. They can be operated in-
210 dividually or integrated in the readout nodes of other detectors, as for example silicon drift
211 chambers, but they always need to be connected to an ASIC with a readout circuit on it.
212 In recent years, the sensor development was driven by an intensive R&D and prototyping
213 for x-ray imagers and the ILC vertex detector.

214 2.4 CMOS MAPS and DMPAS

215 Monolithic active pixels accommodate on the same wafer both the sensor and the FE
216 electronics, with the second one implanted on top within a depth of about $1 \mu\text{m}$ below
217 the surface. MAPS have been first proposed and realized in the 1990s and their practical
218 usage has been enabled by the development of the electronic sector, which guarantees the
219 halving of CMOS transistors dimension at least every two years, as stated by the Moore's
220 law. As a matter of fact the dimension of components, their organization on the pixel
221 area and logic density are important issues for the design and for the layout. Compared
222 to CCDs, the readout time is dramatically reduced by the in-pixel amplification and
223 discrimination, typically followed by a sparsified readout not requiring the signal to be
224 transported anymore over thousands of pixels; as aside effect, the radiation tolerance is
225 also greatly increased by sensing the signal charge directly within its own pixel.

226 A critical parameter for accelerator experiments is the material budget, which repre-
227 sents the main limit factor for momentum measurement resolution in a magnetic field;
228 since hybrid pixels are thicker (\sim hundreds of μm) than monolithic ones (even less than
229 $100 \mu\text{m}$). Using the latter the material budget can be down by a third: typical values for
230 hybrid pixels is 1.5 % X_0 per layer, while for monolithic 0.5 % X_0 . Compared to MAPS,
231 among other disadvantages of hybrid pixels there is the bigger power consumption, that
232 requires also a bigger cooling system, leading to a futher increase of material.

233 Monolithic active pixel can be distinguished between two main categories: MAPS and
234 depleted MAPS (DMPAS). MAPS (figure a ??) have typically an epitaxial layer in a from
235 range $1 \mu\text{m}$ to $20 \mu\text{m}$ and, since they are not depleted, the charge is mainly collected by
236 diffusion rather than by drift. This makes the path of charges created in the bulk longer
237 than usual, making them slow (of order of 100 ns). Moreover, the collection can be partial,

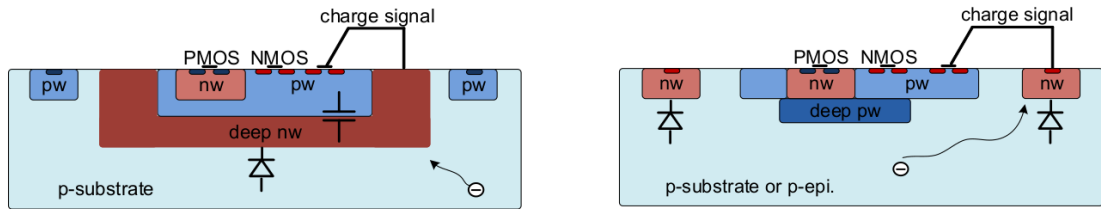


Figure 2.4: Concept cross-section with large and small fill factor

238 especially after irradiation of the detector (look at A for radiation damages), when the
 239 trapping probability becomes higher. In figure ?? it is shown as example of CMOS MAPS:
 240 the sensor implements an n well as collection diode; to prevent the others n wells (which
 241 contain PMOS transistor) of the electronic circuit competing in charge collection and to
 242 shield the CMOS circuit from the substrate, additional underlying deep p well are needed.
 243 DMAPS are instead MAPS depleted with d typically in $\sim 25 \mu\text{m}$ to $150 \mu\text{m}$ (eq. 2.2) which
 244 extends from the diode to the deep p-well, and sometimes also to the backside (in this
 245 case if one wants to collect the signal also on this electrode, additional process must be
 246 done).

247 2.4.1 DMAPS: large and small fill factor

248 There are two different sensor-design approaches (figure 2.4) to DMAPS:

- 249 • large fill factor: a large collection electrode that is a large deep n-well and that host
 250 the embedded electronics
- 251 • small fill factor: a small n-well is used as charge collection node

252 To implement a uniform and stronger electric field, DMAPS often uses large electrode
 253 design that requires multiple wells (typically four including deep n and p wells); with this
 254 layout the total capacity of the sensor increases because of the addition of a new term
 255 (fig. 2.5), which contributes to the total amplifier input capacity ($\sim 100 \text{ fF}$). In addition
 256 to the capacity between pixels (C_{pp}) and between the pixel and the backside (C_b), a non-
 257 negligible contribution comes from the capacities between wells (C_{SW} and C_{WW}) needed
 258 to shield the embedded electronics. These capacities affect the thermal and 1/f noise of
 259 the charge amplifier and the τ_{CSA} too:

$$260 \quad ENC_{thermal}^2 \propto \frac{4 kT}{3 g_m \tau_{sh}} \frac{C_D^2}{261} \quad \tau_{CSA} \propto \frac{1}{g_m} \frac{C_D}{C_f} \quad (2.5)$$

262 where g_m is the transconductance, τ_{sh} is the shaping time. Among the disadvantages coming
 263 from this large input capacity there is a coupling between the sensor and the electronics
 264 resulting in cross talk noise on neighbouring electrodes; indeed, since digital switching in
 265 the FE electronics does a lot of oscillations, this problem is especially connected with the
 266 intra wells capacities. So, larger charge collection electrode sensors provide a uniform electric
 267 field in the bulk that results in short drift path and so in good collection properties,
 268 especially after irradiation, when trapping probability can become an issue.

269 The small fill-factor variant, instead, benefits from a small capacity (5 fF to 20 fF), but
 270 suffers from a non uniform electric field and from all the issue related to that (slowness
 271 and high trapping probability). As we'll see these two different types of sensor require

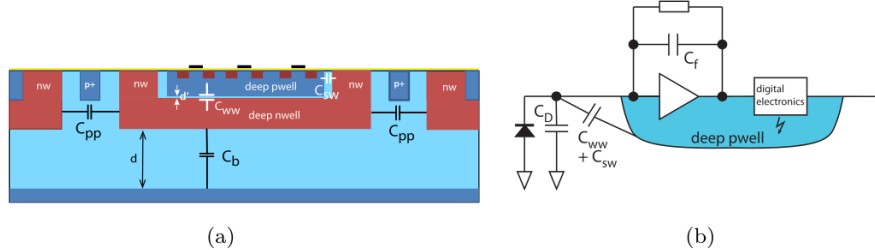


Figure 2.5: C_{pp} , C_b , C_{WW} , C_{SW}

	small fill factor	large fill factor
small sensor C	✓ (< 5 fF)	✗ (~ 100 200 fF)
low noise	✓	✗
low cross talk	✓	✗
velocity performances	✓	✗ (~100 ns)
short drift paths	✗	✓
radiation hard	✗	✓

Table 2.1: Small and large fill factor DMAPS characteristics

270 different amplifier: the large electrode one is coupled with a charge sensitive amplifier,
271 while the small one with a voltage amplifier (sec 2.5.1).

272 2.4.2 A modified sensor

273 A process modification, developed by CERN in collaboration with the foundries, which
274 has become the standard solution to combine the characteristics of a small fill factor
275 sensor (small input amplifier capacity) and of a large fill factor sensor (uniform electric
276 field), is the one carried out for ALICE upgrade about ten years [1]. A compromise
277 between the two sensors could also be making smaller pixels, but this solution requires
278 reducing the electronic circuit area, so a completely new pixel layout should be though.
279 The modification consists in inserting a low dose implant under the electrode and one of
280 its advantage lies in its versatility: in fact, both standard and modified sensor are often
281 produced for testing.

282 Before the process modification, the depletion region extends below the diode towards
283 the substrate, and it does not extend much laterally, even if a high bias is applied to the
284 sensor (fig. 2.6). After the modification, two distinct pn junctions are built: one between
285 the deep p well and the n⁻ layer, and the other between the n⁻ and the p⁻ epitaxial
286 layer, extending to the whole area of the sensor. Since deep p well and the p-substrate are
287 separated by the depletion region, the two p electrodes can be biased separately² and this
288 is beneficial to enhance the vertical electric field component. The doping concentration is
289 a trimmer parameter: it must be high enough to be greater than in the epitaxial layer in
290 order to prevent the punchthrough between p-well and the substrate, but it must also be
291 low enough to allow the depletion for reasonable bias values.

²This is true in general, but it can be denied if other doping characteristics are implemented, and we will see that this is the case of TJ-Monopix1

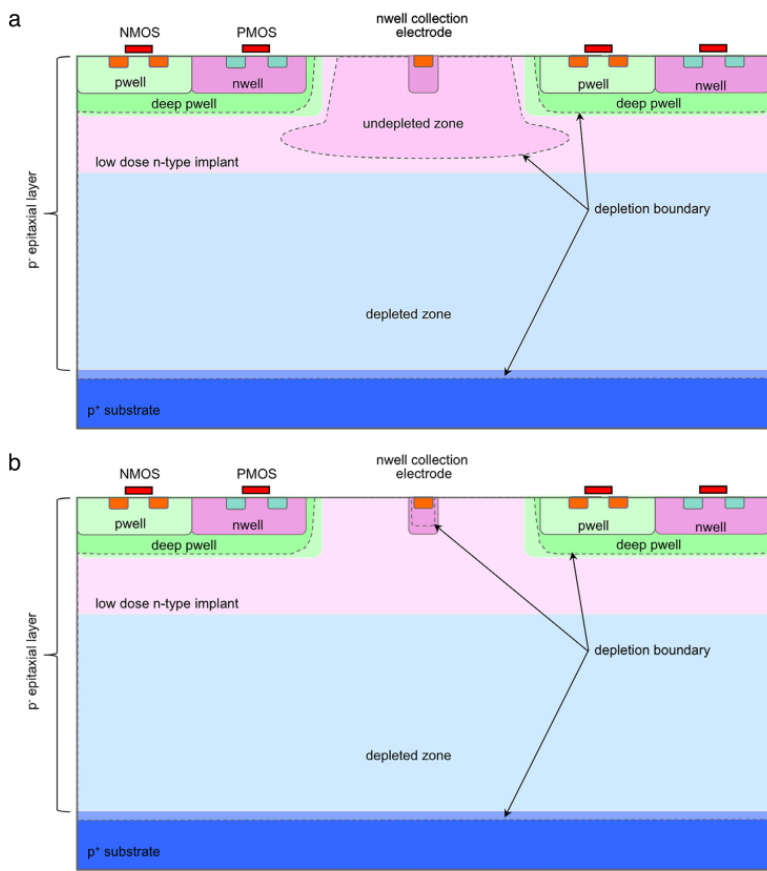


Figure 2.6: A modified process for ALICE tracker detector: a low dose n implant is used to create a planar junction. In (a) the depletion is partial, while in (b) the pixel is fully depleted.

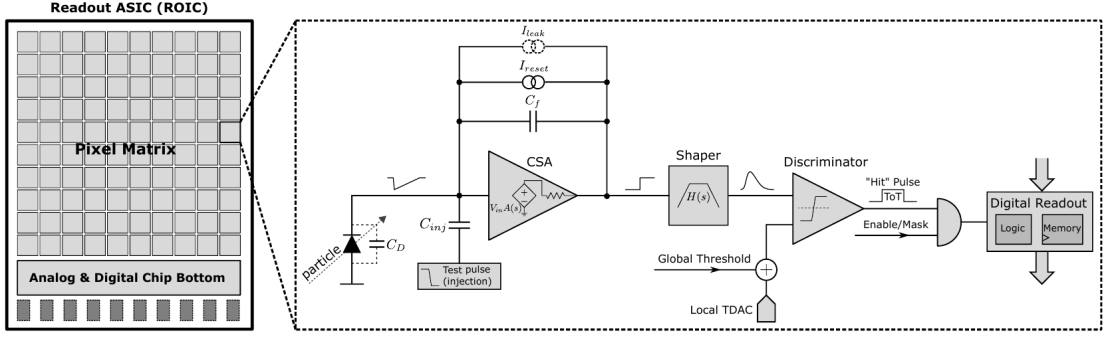


Figure 2.7: Readout FE scheme: in this example the preamplifier is a charge sensitive one (CSA) but changing the capacitive feedback into a resistive one, this can be converted in a voltage or current amplifier.

2.5 Analog front end

After the creation of a signal on the electrode, the signal enters the front end circuit (fig.2.7), ready to be molded and transmitted out of chip. Low noise amplification, fast hit discrimination and an efficient, high-speed readout architecture, consuming as low power as possible, are the goal of the readout integrated electronics (ROIC). The main parts of the analog front end chain are a preamplifier (that often is the only amplification stage) with a reset to the baseline mechanism and a leakage current compensation, a shaper (a band-pass filter) and finally a discriminator. The whole chain must be optimized and tuned to improve the S/N ratio. It is very important both not to have a large noise before the amplification stage in order to not multiply that noise, and chose a reasonable threshold of the discriminator to cut noise-hits much as possible.

2.5.1 Preamplifier

Even if circuits on the silicon crystal are only constructed by CMOS, a preamplifier can be processed as an operational amplifier (OpAmp) where the gain is determined by the input and feedback impedance (first step in figure 2.7):

$$G = \frac{v_{out}}{v_{in}} = \frac{Z_f}{Z_{in}} \quad (2.6)$$

Depending on whether a capacity or a resistance is used as feedback, respectively a charge or a voltage amplifier is used: if the voltage input signal is large enough and has a sharp rise time, the voltage sensitive preamplifier is preferred. Consequently, this flavor doesn't suit to large fill factor MAPS whose signal is already high enough: $v_{in} = Q/C_D \approx 3 \text{ fC}/100 \text{ pF} = 0.03 \text{ mV}$, but it's fine for the small fill factor ones: $v_{in} = Q/C_D \approx 3 \text{ fC}/3 \text{ pF} = 1 \text{ mV}$.

In the case of a resistor feedback, if the signal duration is longer than the discharge time ($\tau = R_S C_D$) of the detector the system works as current amplifier, as the signal is immediately transmitted to the amplifier; in the complementary case (signal duration longer than the discharge time) the system integrates the current on the C_D and operates as a voltage amplifier.

318 2.6 Readout logic

319 The readout logic includes the part of the circuit which takes the FE output signal, pro-
 320 cesses it and then transmit it out of pixel and/or out of chip; depending on the situation
 321 of usage different readout characteristics must be provided. To store the analogical in-
 322 formation (i.e. charge collected, evolution of signal in time, ...) big buffers and a large
 323 bandwidth are needed; the problem that doesn't occur, or better occur only with really
 324 high rate, if one wants record only digital data (if one pixel is hit 1 is recorded, and if not
 325 0 is recorded).

326 A common compromise is to store the time over threshold (ToT) of the pulse in clock
 327 cycle counts; this needs of relatively coarse requirement as the ToT can be trimmed down
 328 to use only a dozen bits but, being correlated (and hopefully linear) with the deposited
 329 charge, it provides a sufficient information. The ToT digitalization usually takes advantage
 330 of the distribution of a clock (namely BCID, bunch crossing identification) on the pixels'
 331 matrix. The required timing precision is better than ~ 25 ns, that corresponds to the period
 332 between bunch collisions at LHC; for such reason a reasonable BCID-clock frequency for
 pixels detector is 40 MHz.

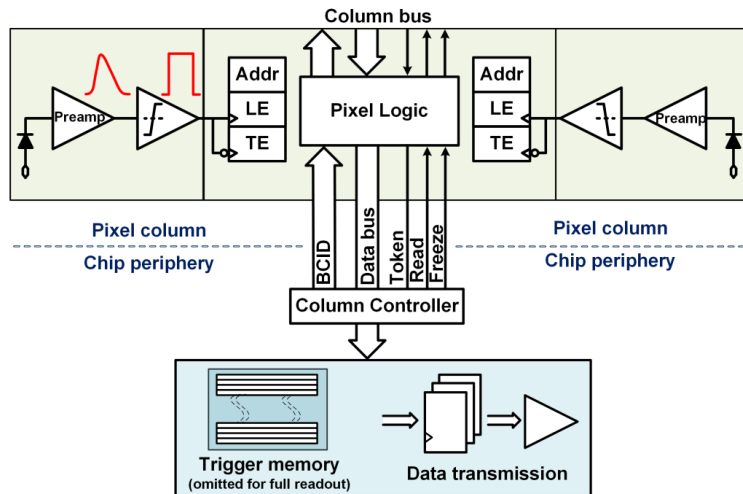


Figure 2.8: Column drain R/O scheme where ToT is saved

333 Moreover, the readout architecture can be full, if every hit is read, or triggered, if a
 334 trigger system decides if the hit must be stored or not. On one hand the triggered-readout
 335 needs buffers and storage memories, on the other the full readout, because there is no
 336 need to store hit data on chip, needs an high enough bandwidth. A triggered readout is
 337 fundamental in accelerator experiments where the quantity of data to store is very large
 338 and some selection has to be applied by the trigger: to give an order of magnitude, at LHC
 339 more than 100 TBit/s of data are produced, but the storage limit is about 100 MBit/s
 340 [2](pag. 797). Typically, the trigger signal is processed in a few μs , so the pixel gets it
 341 only after a hundred clock cycles from the hit arrival time: the buffer depth must be able
 342 to handle such high trigger latency.

344 After having taken out the data from the pixel, it has to be transmitted to the end
 345 of column (EoC) where a serializer delivers it out of chip, typically to an FPGA. There
 346 are several ways of transmitting data from a pixel to the EoC: one of the most famous
 347 is the column-drain read out, developed for CMS and ATLAS experiments [3]. All the

348 pixels in a double-column share a data bus and only one pixel at a time, according to
 349 a priority chain, can be read. The reading order circuit is implemented by shift register
 350 (SR): when a hit arrives, the corresponding data, which can be made of timestamp and
 351 ToT, is temporarily stored on a RAM until the SR allows the access to memory by data
 352 bus. Even if many readout architectures are based on the column-drain one, it doesn't suit
 353 for large size matrices. The problem is the increasing number of pixels on a column would
 354 also raise the number of pixels in the priority chain, which would result in a slowdown of
 355 the readout.

356 If there isn't any storage memory, the double-column behaves as a single server queue
 357 and the probability for a pixel of waiting a time T greater than t , with an input hit rate
 358 on the column μ and an output bandwidth B_W is [4]:

$$P(T > t) = \frac{\mu}{B_W} e^{-(B_W - \mu)t} \quad (2.7)$$

359 To avoid hit loss (let's neglect the contribution to the inefficiency of the dead time τ due
 360 to the AFE), for example imposing $P_T > t \sim 0.001$, one obtains $(B_W - \mu) t_t \sim 6$, where
 361 t_t is the time needed to transfer the hit; since t_t is small, one must have $B_W \gg \mu$, that
 means a high bandwidth [4].

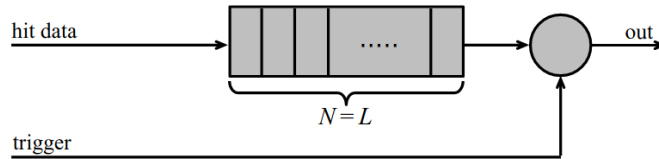


Figure 2.9: Block diagram of a pipeline buffer: N is the dimension of memory buffer and L is the trigger latency expressed in BCID cycles

362 Eq.2.7 is actually an approximation, since each pixel sees a different bandwidth de-
 363 pending on the position on the queue: the first one sees the full bandwidth, while the next
 364 sees a smaller one because it can be occasionally blocked by the previous pixel. Then,
 365 the bandwidth seen by the pixel i is $B_i = B - \sum_j \mu_j$, where μ_j is the hit rate of the j th
 366 pixel. The efficiency requirement on the bandwidth and the hit rate becomes: $B_{W,i} > \mu_i$,
 367 where the index i means that the constraint is for a single pixel; if all the N pixels on a
 368 column have the same rate $\mu = N\mu_i$, the condition reduces to $B_W > \mu$. The bandwidth
 369 must be chosen such that the mean time between hits of the last pixel in the readout chain
 370 is bigger than that. In order to reduce the bandwidth, a readout with zero suppression
 371 on pixel is typically employed; this means that only information from channels where the
 372 signal exceeds the discriminator threshold are stored.

374 If, instead, the signal is locally stored until a trigger signal arrives, the input rate to
 375 column bus μ' is reduced compared to the hit rate μ as: $\mu' = \mu \times r \times t$, where r is the
 376 trigger rate and t is the bunch crossing period. In this situation there is a more relaxed
 377 constraint on the bandwidth, but the limiting factor is the buffer depth: the amount of
 378 memory designed depends both on the expected rate μ and on the trigger latency t as
 379 $\propto \mu \times t$, which means that the higher the trigger latency the lower the hit rate to cope
 380 with.

381 In order to have an efficient usage of memory on pixels' area it's convenient grouping
 382 pixels into regions with shared storage. Let's compare two different situations: in the first
 383 one a buffer is located on each pixel area, while in the second one a core of four pixels

³⁸⁴ share a common buffer (this architecture is commonly called FE-I4).

Consider a 50 kHz single pixel hits rate and a trigger latency of 5 μs , the probability of

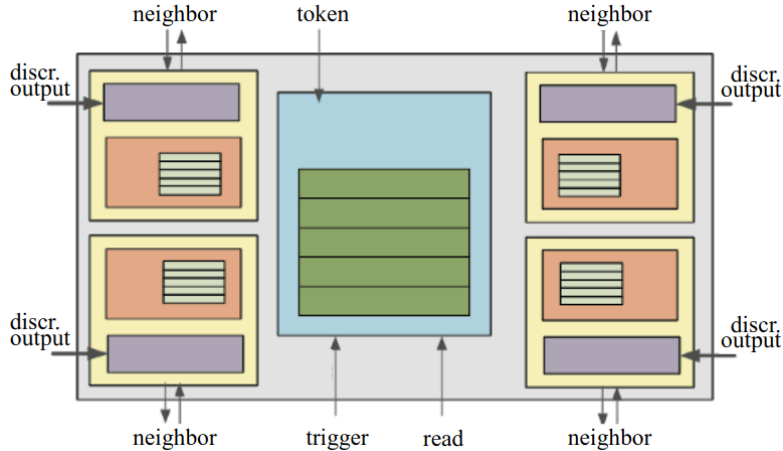


Figure 2.10: Block diagram of the FE-I4 R/O. Read and memory management section is highlighted in light blue; latency counters and trigger management section are highlighted in green; hit processing blocks are highlighted in purple; ToT counters and ToT management units are highlighted in orange

³⁸⁵

³⁸⁶ losing hits is:

$$P(N > 1|\nu) = 1 - P(N = 0|\nu) - P(N = 1|\nu) = 1 - e^{-\nu}(1 + \nu) \approx 2.6\% \quad (2.8)$$

³⁸⁷ where I have assumed a Poissonian distribution with mean $\nu = 0.25$ to describe the counts
³⁸⁸ N.

³⁸⁹ To get an efficiency ϵ greater than 99.9 % a 3 hit depth buffer is needed:

$$P(N > 3|\nu) = 1 - \sum_{i=0}^3 P(N = i|\nu) < 0.1\% \quad (2.9)$$

³⁹⁰ Consider the second situation: if the average single pixel rate is still 50 kHz, grouping four
³⁹¹ pixels the mean number of hits per trigger latency is $\nu = 0.25 \times 4 = 1$. To get an efficiency
³⁹² of 99.9% (eq. 2.9) a buffer depth of 5 hits in the four-pixels region, instead of 3 per pixels,
³⁹³ is needed.

394 **Chapter 3**

395 **Use of pixel detectors**

396 The relation between the development of cameras and that of pixel detectors dates back
397 to 1969, when the idea of CCDs, for which Boyle and Smith were awarded the Nobel Prize
398 in Physics in 2009, revolutionized photography allowing light to be captured electronically
399 instead of on film. Even though the CMOS technology already existed at the time the
400 CCDs spread, the costs of productions were too high to allow the diffusion of these sensors
401 for the following 20 years. From that moment on, the fast diffusion of CMOS was mainly
402 due to the less cost than CCD, and the less power supply required. Nowadays CCDs
403 are still preferred over MAPS in astronomy, where the astronomical sources' rate are low
404 enough to cope with slow readout time (tens of ms).

405 The principal use cases of pixel detectors are particle tracking and imaging: in the
406 former case individual charged particles have to be identified, in the latter instead an
407 image is obtained by the usually un-triggered accumulation of the impinging radiation.
408 Also the demands on detectors performance depends on their usage, in particular tracking
409 requires high spatial resolution, fast readout and radiation hardness.

410 **3.1 Tracking in HEP**

411 At first the physics world overlooked the CCDs, and all pixel in general, as against the
412 gaseous detector for tracking: there was no need to replace these ones which had a sufficient
413 good resolution ($100\text{ }\mu\text{m}$). Since 1974, with the measurement of the invariant mass of the
414 J/Psi and the affirmation of the quark model, all experiments start to look for better
415 spatial resolutions in order to achieve the possibility of reconstructing short lived particle.

416 Historically, the first pixel detector employed in particle physics was a CCD: it was
417 installed in the spectrometer at the CERN's Super Proton Synchrotron (SPS) by the
418 ACCMOR Collaboration (Amsterdam, CERN, Cracow, Munich, Oxford, RAL) at mid
419 1980s, with the purpose of studying the (at the time) recently-discovered charm particles.
420 The second famous usage of CCDs took place at SLAC in the Large Detector (SLD) during
421 the two years 1996-98, where the CCD technology was adopted instead of the microstrip
422 detectors for their excellent spatial resolution (cell size $22\times 22\text{ }\mu\text{m}^2$ giving a resolution of
423 $\sim 5\text{ }\mu\text{m}$) thanks to the sufficient time for readout between two successive collisions (160 ms).

424 From that period on particle tracking in experiments have been transformed radically:
425 it was mandatory for HEP experiments to build an inner vertex detector, where the general
426 tasks are:

- 427 • pattern recognition with the identification of particle tracks at large backgrounds and

428 pile-up

- 429 • measurement of vertices (primary and secondary)
- 430 • multi-track and vertex separation in the core of jets
- 431 • measurement of specific ionization
- 432 • momentum measurement combining with other detectors informations

433 In 1991, the more demanding environments led to the development of hybrid pixel
434 detectors: a dedicated collaboration, RD19, was established at CERN with the specific goal
435 of defining a semiconductor micropattern detector with an incorporated signal processing
436 at a microscopic level. In those years a wide set of prototypes of hybrid pixel has been
437 manufactured; among the greatest productions a mention goes to the huge ATLAS and
438 CMS vertex detectors. From the middle of 2013 a second collaboration, RD53, has been
439 established with the new goal of finding a pixel detector suitable for phase II future
440 upgrades of those experiments. Even if the collaboration is specifically focused on design
441 of hybrid pixel readout chips (aiming to 65 nm tecnique so that the electronics fits within
442 the pixel area), also other options have been taken in account and many test have been done
443 on MAPS. Requirements imposed by HL-LHC will become tigher in time: for example, a
444 dose and radiation of 5 Mrad and 10^{16} NIEL are exepected after 5 years of operation. Time
445 resolution, material budget and power consumption are also issues for the upgrade: to
446 distinguish different events from different bunches a time resolution better than 25 ns for
447 a bunch crossing frequency of 40 MHz is required, and also a material budget lower than
448 2% and a power consuption lower than 500 mW/cm² are required.

449 Amidst the solutions proposed 3D silicon detector, invented by Sherwood Parker in
450 1995, and MAPS are the most promising. In 3D sensors the electrode is a narrow column
451 of n-type implanted vertically across the bulk instead of being implanted on the wafer's
452 surface. The charge produced by the impinging particle is then drifted transversally within
453 the pixel, and, as the mean path between two electrode can be soufficent low, the trap
454 probability is not an issue. Even if 3D detector are adequately radiation hard and are a
455 strong contender for hybrid pixel modules, especially in the innermost pixel detector layer,
456 the fabrication process is currently low volume, making them unlikely to cover large areas.

457 3.1.1 Hybrid pixels at LHC and at SuperKEKB

458 **ATLAS**

459 With CMS, ATLAS is one of two general-purpose detectors at the LHC and has the largest
460 volume detector ever constructed for a particle collider (46 m long and 25 m in diameter).
461 The Inner Tracker (ITk) consists of three different systems all immersed in a magnetic
462 field parallel to the beam axis whose main components are: the pixel, the micro-strips and
463 transition radiation trackers. Concerning the pixel detector, they installed a 3-layer hybrid
464 pixel detector in 2007 and an additional one inserted within the original detector envelope
465 and therefore called insertable B-layer (IBL) in 2014. 92 million pixels are divided in 4
466 barrel layers and 3 disks in each end-cap region, covering a total area of 1.9 m² and having
467 a 15 kW of power consumption.

468 As stated by the ATLAS collaboration the pixel detector is exposed by an extreme
 469 particle flux: "By the end of Run 3¹, the number of particles that will have hit the
 470 innermost pixel layers will be comparable to the number it would receive if it were placed
 471 only a few kilometres from the Sun during a solar flare". Considering that the particle
 472 density will increase even more with HL-LHC, radiation hardness is definitively target to
 473 achieve. The most ambitious goal is employ a MAPS-based detector for the inner-layer
 474 barrels, and for this reason the RD53 collaboration is designing many MAPS prototypes
 475 (as for example TJ-Monopix1, which I will talk about in chapter 4) and performing test.
 476 Up to now this possibility will be eventually implemented during the second phase of the
 477 HL-LHC era, as at the start of high-luminosity operation the selected option is the hybrid
 478 one. The sensor will be bonded with ITkPix, the first full-scale 65 nm hybrid pixel-readout
 479 chip developed by the RD53 collaboration. Regarding the sensor, a valuable option is
 480 using 3D pixels, which have already proved themselves in ATLAS, for the IBL, where they
 481 were introduced in a limited acceptance range and introduced a new readout integrated
 482 circuit called FE-I4. Also the complexity of the readout will be raised, as the number of
 483 pixels will be increased of a factor about 7, passing from 92 millions to 6 billion.

484 CMS

485 The CMS hybrid pixel detector has been upgraded in 2017, when, with the replacement
 486 of a piece of the beam pipe, a layer has been added to the detector at 3 cm from it.
 487 124 million pixels are divided between the barrel pixel detector (BPIX) and the forward
 488 disks (FPIX), with sensors which are different from each other and produced by different
 489 foundries. The sensors have an area equal to 100 μm by 150 μm and have been produced
 490 on 285 μm to 300 μm thick wafers.

491 The time resolution is 25 ns, and the information coming from the detector are stored on
 492 chip for the Level-1 trigger latency ($\sim 4 \mu\text{s}$). The upgrade baseline ROIC was redesigned for
 493 the outer 3 layers, replacing analog signal readout with on-chip ADCs and digital readout
 494 at higher rate. reads out the pulse height information for each pixel.

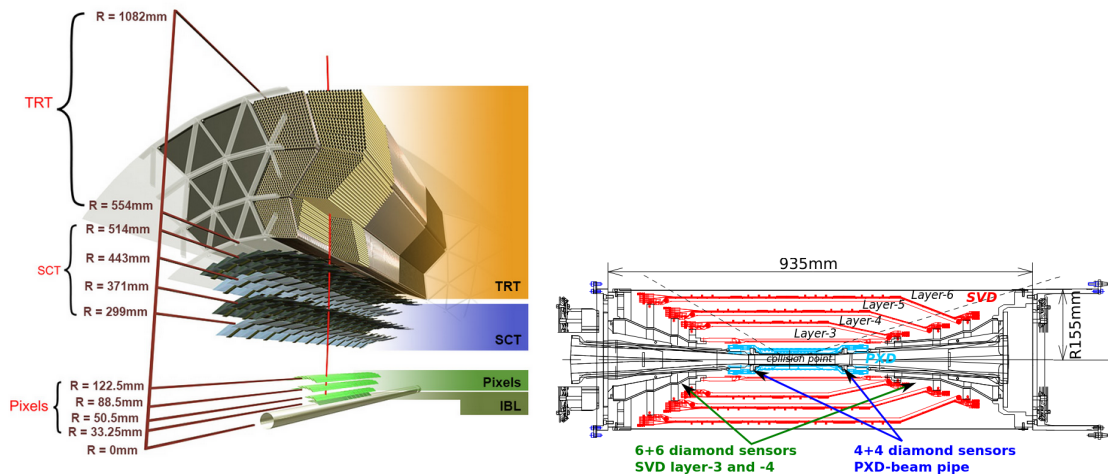


Figure 3.1: (a), (b) Since an accidental beam background enhancement can damage the VXD, diamond detectors are installed in order to monitoring it.

¹Run 3 start in June 2022

495 **LHCb**

496 LHCb is a dedicated heavy-flavour physics experiment that exploits pp interactions at
497 14 TeV at LHC. It was the last experiment to upgrade the vertex detector, the Vertex
498 Locator (VELO), replacing the silicon-strip with 26 plane pixel detector (beacause of the
499 fixed target geometry) in May 2022. As the instantaneous luminosity in Run3 is increased
500 by a factor $\lesssim 10$, much of the readout electronics and of the trigger system have been
501 developed in order to cope with the large interaction rate. To place the detector as close as
502 possible to the beampipe and reach a better track reconstruction efficiency and resolution,
503 the VELO has a surprising feature: during the injection of LHC protons it is parket at
504 3 cm from the beams and only when the stability is reach it is moved at ~ 5 mm. Readout
505 speed is a priority for the detector that use a triggerless readout at 40 MHz collision rate,
506 producing 20 Gbps per ROIC. The Velopix, which is the hybrid system designed for LHCb,
507 is made bonding sensors, each measuring 55×55 micrometers, 200 μm -thick to a 200 μm -
508 thick ASIC specially developed for LHCb and coming from the Medipix family (sec. ??),
509 which can handles hit rates up to 900 MHz per chip. Since the detector is operated under
510 vacuum near the beam pipe, the heat removal is particularly difficult and evaporative CO₂
511 microchannel cooling are used.

512 **BelleII**

513 Due to the high background level coming from the nanobeam used at SuperKEKB in order
514 to achieve a such high luminosity ($4.7 \times 10^{34} \text{1/cm}^2/\text{s}$), silicon strip cannot be used in the
515 inner layer of the tracker. The occupancy is too high to allow the usage of strips up to
516 40 mm from the beam pipe. Moreover for a precise reconstruction of B-decay vertices, the
517 usage of thin detector is mandatory at the low energy (4 GeV to 7 GeV) of the beam, in
518 order to minimize the multiple scattering of particles.

519 The current vertex detector of BelleII, VXD, is made of a pixel detector (PXD), fab-
520 ricated with 2 layers of DEPFET-based pixels, and 4 layers of a double-sided silicon strip
521 detectors (SVD)[5]. Due to the small capacitance of the collection node, DEPFET presents
522 a high signal-to-noise ratio (in 30-50) thanks to the low instrinsic noise and to the large
523 signal achieved with he fully depleted bulk: pixels are thinned to 75 μm in the active
524 region, then a MIP is supposed to create a signal of $\sim 6000 e^-$, while the typical noise of
525 DEPFET is around 200 e^- . The ASIC read out is still based on a rolling shutter logic,
526 with an integration time of 20 μs . In order to reduce the data-storage memory PXD hits
527 are only used to improve spatial resolution of tracks: the SVD informations are used by
528 the High Level Trigger (HLT) to look for regions of interest in the pixel ladders just by
529 extrapolating back the tracks found in the tracker detector, and this method allows to
530 store only data belonging to these areas; the PXD hits are then used in offline track fit to
531 improve the vertex resolution.

532 MAPS have been proposed for the replacement of VXD during the Long Shut Down
533 2 (LSD2) foreseen around 2026-27; the new vertex detector, VTX, should be made of 5
534 layers fabricated by the optimized Belle II pixel sensor (OBELIX), a detector based on
535 TJ-Monopix have been selected (look at chapter ??). The main advantages VTX should
536 bring are a obvious improving in the track and vertex resolution (14 μm before upgrade,
537 $\lesssim 10 \mu\text{m}$ expected after upgrade) and a reduction in the X_0 (da.. a..), a higher background
538 tolerance because of the smaller sensor than strips dimension and a low bandwidth due to
539 the on-chip sparsification.

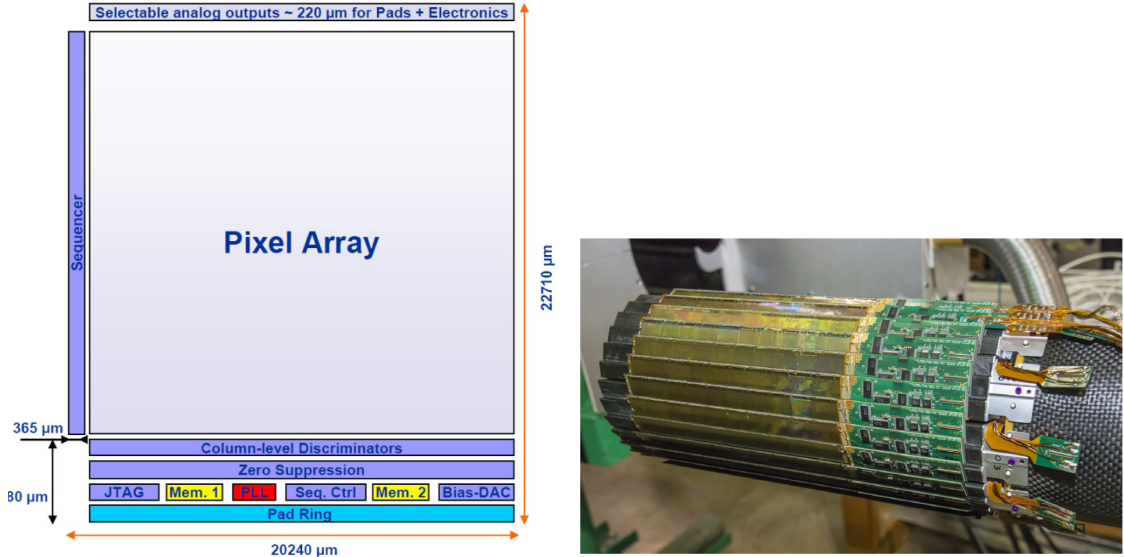


Figure 3.2: (a) The HFT PXL detector; (b) Block-diagram of the ULTIMATE-2 sensor

540 3.1.2 First attempts to MAPS

541 MIMOSA at EUDET and STAR

542 MIMOSA [6][7] (standing for Minimum Ionizing MOS Active pixel sensor), designed in
 543 2008, prefigured the architecture of MAPS for coming vertex detector being the first large
 544 scale sensor to be employed as detector. MIMOSA-26 equiped the final version of EUDET
 545 high resolution beam telescope both at CERN-SPS and at DESY while the MIMOSA-
 546 28 devices are used for the first MAPS-based vertex detector at the STAR experiment.
 547 MIMOSA-26 is fabricated in a 350 nm, and a module features 1152 columns, split into
 548 18 indipendent groups, and 576 rows, with square pixels having a side of 18.4 μm lenght;
 549 the epitaxyal layer is not fully depleted and the charge collection is mostly by diffusion,
 550 resulting in charge sharing between pixels and collection time bigger than 100 ns.

551 The readout is done in a rolling shutter mode and it is the first MAPS integrating on
 552 chip the zero supresion: the chip is an Active Pixels (APS) and therefore it incorporates
 553 the amplification on pixel, while the signal discrimination and zero-suppression logic are
 554 placed at the EoC, where is also placed a memory. The chip is an Active Pixels (APS)
 555 and therefore it incorporates the amplification on pixel, while the signal discrimination
 556 and zero-suppression logic are placed at the EoC: the readout is done in a rolling shutter
 557 mode with a frame integration time that can be lowered down to 85 ms, and a memory
 558 allowing to store up to six hits is.

559 The EUDET telescope, equipped with six sensor planes, requires highly granular and
 560 thin pixel detectors in order to achieve an excellent track resolution (around 2 μm) even at
 561 the rather low particle energies of up to 6 GeV. The STAR experiment at the Relativistic
 562 Heavy Ion Collide (RHIC) accelerator at the Brookhaven National Laboratory (BNL) is
 563 the first to include MAPS in the vertex detector[8]. The main tracking detector in STAR is
 564 a TPC with radii 60-190 cm embedded in a 0.5 T solenoidal magnetic field, that provides
 565 a pointing resolution of approximately 1 mm. The pixel detector, PXL, is a part of a
 566 3-detector system, Heavy Flavor Tracker (HFT), that has been added to the pre-existing
 567 STAR apparatus just before the 2014 Run in order to improve the impact parameter

resolution and to enable the direct reconstruction of hadronic decays of heavy flavor mesons and baryons. The Heavy Flavor Tracker (HFT) is composed by the Silicon Strip Detector (SSD), the Intermediate Silicon Tracker (IST) and the Pixel Detector (PXL); the first one is placed at 22 cm from the beam pipe and consists of double sided strips with 95 μm inter-strip pitch, the second one, placed at 14 cm, is made of single sided silicon pads with $600 \mu\text{m} \times 6 \text{ mm}$ pitch and the last one made by two layers is placed at 2.8 cm and 8 cm fabricated with ULTIMATE2 (also known as MIMOSA-28), a successor of MIMOSA-26 sensor, with pitch 20.7 μm and thinned down to 50 μm . An area of 0.16 m^2 are covered by 400 MAPS sensor, corresponding to 356 millions of pixels divided into array size of 928×960 . Each pixel includes circuitry for readout, amplification, and Correlated Double Sampling (CDS) for signal extraction and noise subtraction and the frame integration time is 185.6 μs ; after the subtraction the signal to noise ratio is ~ 30 , with a noise between 10-12 electrons and a signal of 1000 e^- . Thanks to the HFT system and the PXL, STAR achieved a track pointing resolution 46 μm for 750 MeV/c kaons, and better than 30 μm for particle momenta bigger than 1 GeV/c: this performance enabled the study of D-meson production with a high significance signal.

584 ALPIDE at ALICE

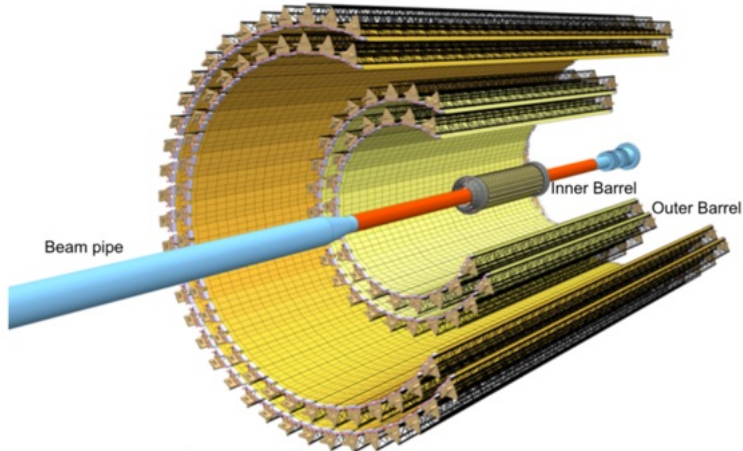


Figure 3.3

585 ALICE (A Large Ion Collider Experiment) is a detector dedicated to heavy-ion physics
 586 at the LHC. The tracking detector consists of the Inner Tracking System (ITS), the gaseous
 587 Time Projection Chamber (TPC) and the Transition Radiation Detector (TRD), and all
 588 those are embedded in a magnetic field of 0.5 T. The ITS is made by six layers of detectors,
 589 two for each type, from the interaction point outwards: Silicon Pixel Detector (SPD),
 590 Silicon Drift Detector (SDD) and Silicon Strip Detector (SSD). Contrary to the others
 591 LHC experiments, ALICE tracker is placed in a quite different environments: the expected
 592 dose is smaller by two order of magnitude and the rate of interactions is few MHz instead
 593 of 40 MHz, but the number of particles comes out of each interaction is higher (the SPS is
 594 invested by a density of particles of $\sim 100 \text{ cm}^{-2}$). The reconstruction of very complicated
 595 events with a large number of particles is a challenge, hence to segment and to minimize
 596 the amount of material, which may cause secondary interaction complicating further the
 597 event topology, is considered a viable strategy.

598 ITS2, upgraded during the LHC long shut down in 2019-20, was the first large-area
599 ($\sim 10 \text{ m}^2$ covered by 2.5 Gpixels) silicon vertex detector based on CMOS MAPS. The
600 detector employes the ALPIDE chip, developed by ALICE collaboration, fabricated in the
601 180 nm CMOS Imaging Sensor process of TowerJazz, whose design takes full advantage
602 of process feature which allows full circuitry within the pixel matrix. Thanks to the
603 reduction of the material budget, ITS2 obtained an amazing improvement both in the
604 position measurement and in the momentum resolution, improving the efficiency of track
605 reconstruction for particle with very low transverse momentum (by a factor 6 at $pT \sim$
606 0.1 GeV/c). Further advancements in CMOS MAPS technology are being aggressively
607 pursued for the ALICE ITS3 vertex detector upgrades (foreseen around 2026-27), with
608 the goals of further reducing the sensor thickness and improving the readout speed (which
609 now is completely asynchronous) of the devices, while keeping power consumption at a
610 minimum.

611 3.2 Other applications

612 Historically for imaging purpose the CCDs were the favoured device: they can be used as
613 single photon counter or integrating and collecting the charge released by more impinging
614 particles. The utilisation in the first case is similar to the tracking one, except that the
615 requirements are less tight, so much that two noteworthy of microchips originally meant
616 for detectors in particle physics at the LHC, and later employed in other fields are Medipix
617 and Timepix. They are read-out chips developed by the Medipix Collaborations since early
618 1990s. For two decades, different Medipix generations have been produced, having a rough
619 correlation with the feature size used: Medipix2 (1999) used 250 nm feature size CMOS
620 while Medipix3 (2005) 130 nm. For photons imaging other materials with higher atomic
621 charge than silicon could be preferred, as a high photon absorption efficiency is needed: it
622 was for this reason that Medipix2 was bump bonded to identically segmented sensors of
623 both silicon and GaAs.

624 The applications in scientific imaging vary from astrophysics and medical imaging and
625 dosimetry to more exotic domains as studies of protein dynamics, material science, art
626 authentication and archaeology. One of the most important employment of Medipix is as
627 X-ray single photon counting in industrial and medical radiography and in 3D computed
628 tomography². Thanks to a New-Zealand company, the MARS Bioimaging detector has
629 been fabricated, which is capable of resolving the photons energy and produce 3D coloured
630 images. Besides tracking in HEP (I have already cited the use of Timepix3 is in the beam
631 telescope of the LHCb VELO), an important use of Timepix is in dosimetry. **Timepix**
632 **Detector for Imaging in Ion Beam Radiotherapy- articolo e qualche info.** A small-Timepix
633 detector with the dimension of a USB can also be found at the International Space Station,
634 where it is exploited for radiation, principally made of heavy-ion, monitoring.

635 3.2.1 Applicability to FLASH radiotherapy

636 A possible new application of pixels detector is dosimetry or beam monitoring of charge
637 particles in high intensity radiography. Recently³ a promising method for RT at ultra high

²The analysis of the direction dependence of X-ray absorption is performed, for example, in order to obtain an image in Computed Tomography (CT)

³The first evidences have been observed on mice experiments in 1966 and in 2014 by the group of Favaudon and Vozenin. After this, many tests on cats and pigs have been performed, and also there has

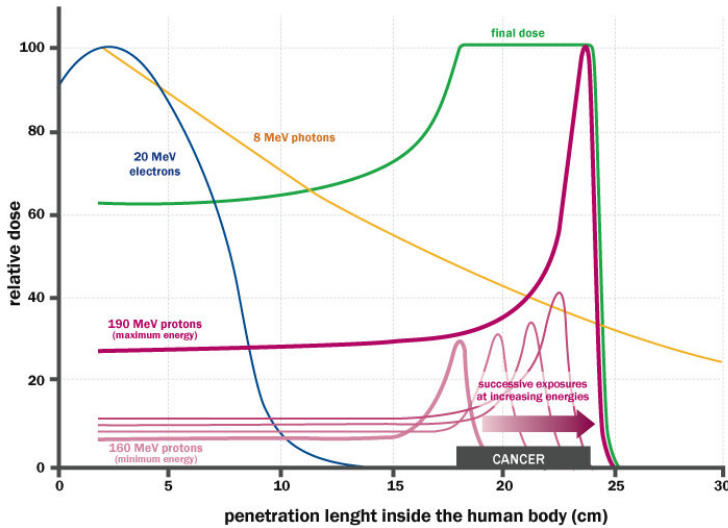


Figure 3.4: The Spread Out Bragg Peak (SOBP) curve (green), which is a constant dose distribution, is obtained from the superposition of many Bragg peak of hadrons with different energy.

638 dose rate (at least 40 Gy/s) and for this reason called FLASH-RT[9], instead of CONV-RT
 639 (0.03 Gy/s), came out. However, finding dosimeters suitable at ultra high dose rate is still
 640 an open issue since almost all standard online dosimeters have shown saturation problems.

641 Radiotherapy

642 The radiological treatment is a common method used in 60% of tumors both as palliative
 643 care and as treatment. It can be given before, after or during a surgery, (Intra operative
 644 radiation therapy-IORT) and many different types of radiations (photons, electrons,
 645 protons and ions, which mainly are hydrogen and carbon) can be used to irradiate the
 646 affected tissues. Exploiting the ionizing energy loss, that can be parametrized by the
 647 Linear Energy Transfer (LET), a biological damage can be delivered to the tissue: while α
 648 and β particles are high LET radiations with values in $100 \text{ keV}/\mu\text{m}$ to $200 \text{ keV}/\mu\text{m}$, x-rays
 649 and gamma-rays are low LET radiations with values in range $0.2 \text{ keV}/\mu\text{m}$ to $2 \text{ keV}/\mu\text{m}$. If
 650 x-ray photons, with energy in 4 MeV to 25 MeV are used, the ionization is caused by the
 651 Compton electrons and is more in the superficial layers of the tissue due to the exponential
 652 attenuation of the beam. The hardrons energy loss, instead, is strongly localized in
 653 the last region of the track, that is the Bragg peak, such as the the treatement typically
 654 requires the scanning of the target. The Relative Biological Effectiveness (RBE) of ions
 655 near th Bragg peak depends on their mass, and in particular it increases with the ion's
 656 mass; even though, too heavy ions generally increases the damage produced also in the
 657 entrance region. Carbon is considered the optimum between the two trends.

658 Electrons, instead, of energy in range of a dozen of MeV tend to spread out on a
 659 bigger region of a few centimeters in both the diameter and thickness. Using Very High
 660 Energy Electrons (VHEE) has been taken into account for irradiation of deeper tissues,
 661 however, to date, the FLASH effect has been tested and demostrated only using low-energy

been a clinical trial on a cutaneous tumor-patient

	CONV-RT	FLASH-RT
Dose rate	0.03 Gy/s	40 Gy/s
Intra pulse dose rate	100 Gy/s	106 Gy/s
Treatment duration	~minutes	$\lesssim 500$ ms
Dose Per Pulse	0.3 mGy	1 Gy to 10 Gy
Pulse width	3 μ s	$\sim 2 \mu$ s

Table 3.1: Typical value of treatment parameters

662 electrons.

663 FLASH effect

664 This treatment takes advantages of biological differences between tumors and healthy
 665 tissues: it is characterized by reducing normal tissue toxicity and maintaining equivalent
 666 tumor damage. The response to dose can be described by the survival fraction probability,
 667 describing the fraction of surviving cell as a function of the dose:

$$S(D) = S(0) e^{-(\alpha D + \beta D^2)} \quad (3.1)$$

668 where α and β respectively represents the rate of cell killing by single ionizing events and
 669 by double hits. Hence, at high doses the density of damages increases and the cells repair
 670 becomes more difficult. Even if the FLASH effect is not yet completely understood and
 671 the underlying mechanisms are not clear, it looks like there are two different recipes which
 672 are involved:

- 673 • **The dose rate:** higher dose rate produce bigger damages (fig. 3.5(a)) since this
 674 prevent cells from sparing.
- 675 • **The presence or absence of oxygen:** while hypoxic cells are very resistant to radi-
 676 ation, normal oxygenated cells are highly radiosensitive. This is because if molecules
 677 containing O_2 break due to the impinging radiation, then the oxygen can build Re-
 678 active Oxygen Species (ROS) (fig.3.5(b))

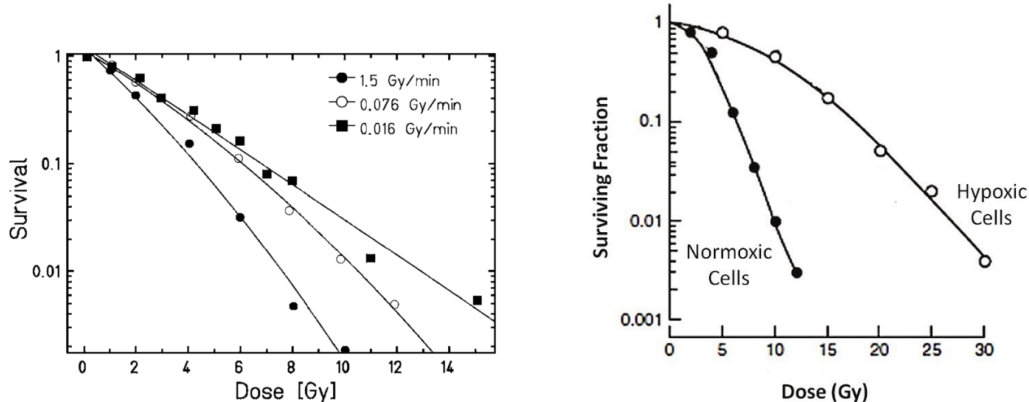


Figure 3.5: (a) Survival curve for different dose rate and (b) for different oxygen cell content

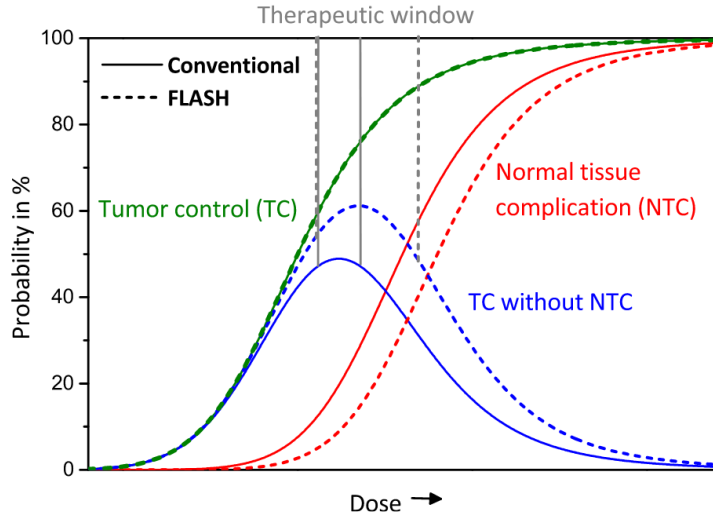


Figure 3.6: Illustration of dependence of TCP, NTCP and therapeutic window on dose, for CONV-RT ad FLASH-RT.

679 The Tumor Control Probability (TCP) and the Normal Tissue Complication (NTC) functions
 680 parametrize respectively the efficiency of damaging on the tumor after having released
 681 a certain dose and the probability of not affecting the healthy tissues. The intermediate
 682 zone between the increase of the TC and of the NTC is called therapeutic window, and
 683 the wider it is and the more effective the treatment is.

684 Dosimetric problems

685 Up to now, all online dosimeters have shown saturation problems at high DDP, differently
 686 from radiochromic films, which are the standard passive dosimeters and have shown a
 687 dose-rate independence up to 109 Gy/s. Even though the linear response in wide dynamic
 688 range, they do not provide any online dosimetric informations, since the time required to
 689 extract the physical value from the reading is not instantaneous⁴.

690 Ionization Chambers (ICs), which are the online reference dosimeter also according to
 691 law, at high level of radiation (already at dose per pulse two orders of magnitude lower
 692 than the ones used for FLASH-RT) show both problems of saturation and recombination.
 693 When a high density of ions and electrons is produced in the gas, a high counter electric
 694 field opposed to the drift one might be generated; if a neutral region build up, both the
 695 recombination of i/e pairs, with a subsequent photoemission and abrupt discharge can
 696 happen⁵. For low level of radiation a correction factors, k_{sat} , can be introduced and a
 697 dose measurement can still be done: with Dose Per Pulse (DDP) lower than 1 mGy the
 698 correction factor is <5%. Non sono sicurissima di aver capito davvero il punto per quanto
 699 riguarda i semiconduttori e gli scintillatori

700 In reference [10] are presented some results related with saturation problems at high
 701 DDP of different types of detectors. The dosimeters tested and their value at which satura-
 702 tion becomes are reported in table 3.2, while in figure 3.7 are reported the measurements.
 703 The DrR is then defined as the ratio between the signal response of each dosimeters at a

⁴COSA sono e più o meno come funzionano

⁵This is called Raether-Meek condition

Commercial detector	Detector type	saturation [Gy/p]
PTW TW34045 Advanced Markus EC	ionization chamber	0.3
PTW TM60017 Dosimetry Diode E	silicon diode	0.15
PTW TW60019 microDiamond	diamond	0.15
DoseVue DoseWireTM Series 100	scintillator fiber	11-26

Table 3.2: Results obtain in [10]

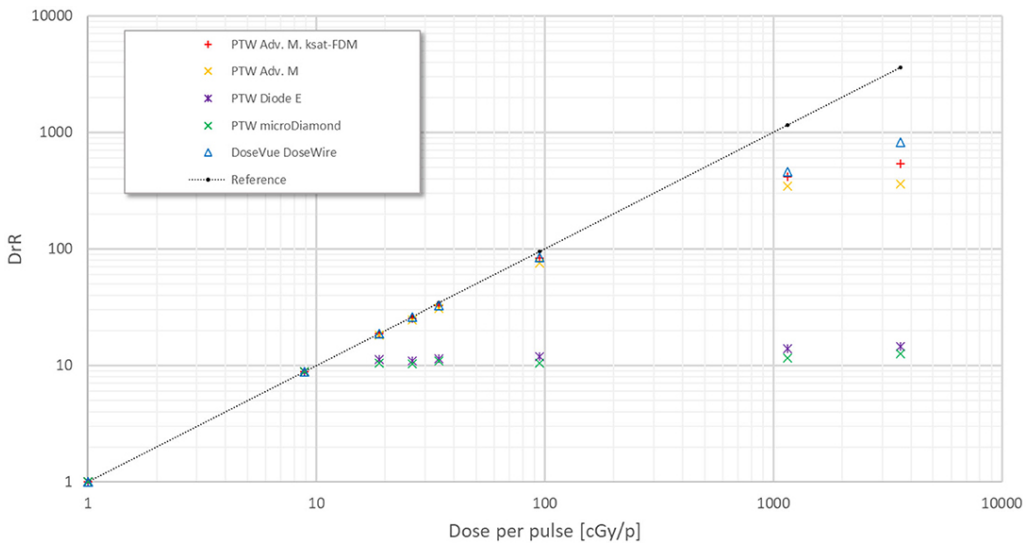


Figure 3.7: Saturation problems underlyed in [10].

704 fixed DDP of 1 cGy/p and is called dosimeter reading ratio (DrR):

$$DrR = \frac{R}{R|_{Dp=1cGy/p}} = \frac{R}{R_{ref}} \quad (3.2)$$

705 Then, for a saturation not affected by saturation problems DrR should be a straight line
 706 with a slope equal to 1; since the reference measurements of dose has been performed with
 707 radiochromic films (GAFCHROMIC EBT-XD), whose dose indipendence has been tested⁶
 708 in range from 0 Gy to 15 Gy, the dotted black line in figure 3.7 represents the reference
 709 measurement done with it.

710 Besides the linearity of the response, two other important requirements for beam mon-
 711 itoring in radiotherapy are both high temporal and space resolutions. Concerning time
 712 resolution I recall that MAPS could handle with rate up to hundreds of MHz, so the pos-
 713 sibility application of these detectors probably strictly depends on their particular usage.
 714 However MAPS might be well suited given that their spatial resolution and their thinness
 715 (they can be thinned down to about 50 μm), which is an obvious requirement for beam
 716 monitor.

⁶The radiochromic films calibration has been obtained by irradiating the films with dose values in range from 0 Gy to 15 Gy, by positioning the films in a polymethylmethacrylate (PMMA) phantom at R₁₀₀ depth, corresponding to 10 cm

⁷¹⁷ **Chapter 4**

⁷¹⁸ **TJ-Monopix1**

⁷¹⁹ TJ-Monopix1 is a small electrode DMAPS with fast R/O capability, fabricated by Tow-
⁷²⁰ erJazz foundry in 180 nm CMOS imaging process. It is part, together with prototypes
⁷²¹ from other series such as TJ-MALTA, of the ongoing R&D efforts aimed at developing
⁷²² DMAPS in commercial CMOS processes, that could cope with the requirements at ac-
⁷²³ celerator experiments. Both TJ-Monopix and TJ-MALTA series [11], produced with the
⁷²⁴ same technology by TowerJazz (the timeline of the foundry products is shown in figure
⁷²⁵ 4.1), are small electrode demonstrators and principally differ in the readout design: while
⁷²⁶ Monopix implements a column-drain R/O, an asynchronous R/O without any distribution
⁷²⁷ of BCID has been used by TJ-Malta in order to reduce power consumption.



Figure 4.1: Timeline in TowerJazz productions in 180 nm CMOS imaging process

⁷²⁸ Another Monopix series, but in 150 nm CMOS technology, has been produced by
⁷²⁹ LFoundry [12]. The main differences between the LF-Monopix1 and the TJ-Monopix1
⁷³⁰ (summarized in table 4.2), lay in the sensor rather than in the readout architecture, as
⁷³¹ both chips implements a fast column drain R/O with ToT capability [13][14]. Concerning
⁷³² the sensors, either are based on a p-type substrate, but with slightly different resistivities;
⁷³³ in addition LFoundry pixels are larger, thicker and have a large fill factor (the very deep n-
⁷³⁴ well covers ~55% of the pixel area). The primary consequence is that LF-Monopix1 pixels
⁷³⁵ have a higher capacity resulting in higher consumption and noise. As I discussed in section
⁷³⁶ 2.4.1, the fact that LF-Monopix has a large fill factor electrode is expected to improve its
⁷³⁷ radiation hardness. Indeed, a comparison of the performance of the two chips showed that
⁷³⁸ TJ-Monopix suffers a comparatively larger degradation of efficiency after irradiation, due
⁷³⁹ to the low electric field in the pixel corner; on the other hand, a drawback of the large fill
⁷⁴⁰ factor in LF-Monopix is a significant cross-talk.

	LF-Monopix1	TJ-Monopix1
Resistivity	$>2 \text{ k}\Omega\text{cm}$	$>1 \text{ k}\Omega\text{cm}$
Pixel size	$50 \times 250 \mu\text{m}^2$	$36 \times 40 \mu\text{m}^2$
Depth	$100\text{-}750 \mu\text{m}$	$25 \mu\text{m}$
Capacity	$\sim 400 \text{ fF}$	$\sim 3 \text{ fF}$
Preamplifier	charge	voltage
Threshold trimming	on pixel (4-bit DAC)	global threshold
ToT	8 bits	6 bits
Consumption	$\sim 300 \text{ mW/cm}^2$	$\sim 120 \text{ mW/cm}^2$
Threshold	$1500 e^-$	$\sim 270 e^-$
ENC	$100 e^-$	$\sim 30 e^-$

Table 4.1: Main characteristics of Monopix1 produced by TowerJazz and LFoundry [13][14]

741 The TJ-Monopix1 chip contains, apart from the pixels matrix, all the required support
 742 blocks used for configuration and testing:

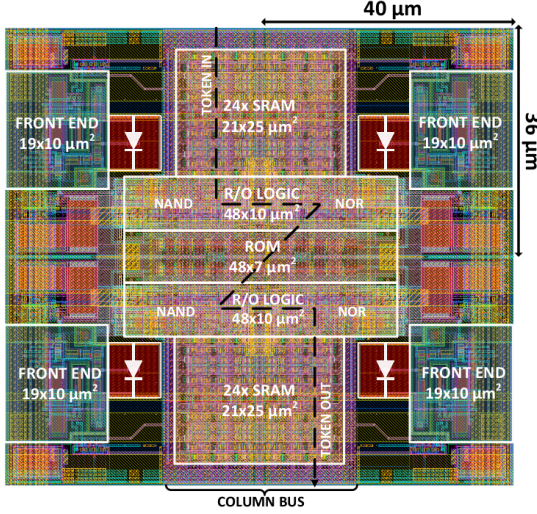
- 743 • the whole matrix contains 224×448 pixels, yielding a total active area approximately
 744 equal to 145 mm^2 over a total area of $1 \times 2 \text{ cm}^2$;
- 745 • at the chip periphery are placed some 7-bit Digital to Analog Converter (DAC), used
 746 to generate the analog bias voltage and current levels and to configuire the FE;
- 747 • at the EoC is placed a serializer to transferred datas immediately, indeed no trigger
 748 memory is implemented in this prototypes;
- 749 • the matrix power pads are distributed at the sides
- 750 • four pixels which have analog output and which can be monitored with an oscillo-
 751 scope, and therefore used for testing

752 Pixels are grouped in 2×2 cores (fig. 4.2a): this layout allows to separate the analog
 753 and the digital electronics area in order to reduce the possible interference between the
 754 two parts. In addition it semplifies the routing of data as pixels on double column share
 755 the same column-bus to EoC. Therefore pixels can be addressed through the physical
 756 column/row or through the logical column/row, as shown in fig. 4.2b: in figure is also
 757 highlighted the token propagaion path, whose I will discuss later.

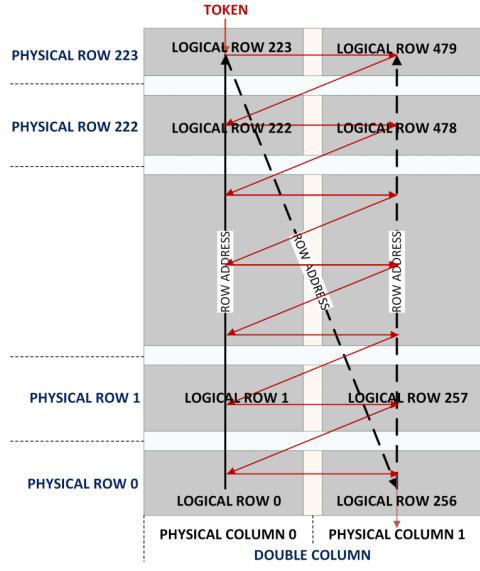
758 Concerning the integration7.7 of the chip in a readout path, TJ-Monopix1 chips have
 759 been wire-bonded on a dedicated carrier board , the Printed Circuit Board (PCB). Two
 760 other board between the DAQ and the chip: the General Purpose Analog Card (GPAC),
 761 which provides power supply channels, current/voltage bias sources and I/O buffer, and
 762 the MIO3 FPGA, which strictly interacts with the DAQ.

763 4.1 The sensor

764 As already anticipated, TJ-Monopix1 has a p-type epitaxial layer and a n doped small
 765 collection electrode ($2 \mu\text{m}$ in diameter); to avoid the n-wells housing the PMOS transistors
 766 competing for the charge collection, a deep p-well substrate, common to all the pixel FE



(a) Layout of a core containing 4 pixels. The analog FE and the digital part are separated in order to reduce cross-talk be



(b)

Parameter	Value
Matrix size	$1 \times 2 \text{ cm}^2$
Pixel size	$36 \times 40 \mu\text{m}^2$
Depth	25 μm
Electrode size	2 μm
BCID	40 MHz
ToT-bit	6
Power consumption	$\sim 120 \text{ mW/cm}^2$

Table 4.2

area, is used. TJ-Monopix1 adopts the modification described in section 2.4.2 that allows to achieve a planar depletion region near the electrode applying a relatively small reverse bias voltage. This modification improves the efficiency of the detector, especially after irradiation, however a simulation of the electric field in the sensor, made with the software TCAD (Technology Computer Aided Design), shows that a nonuniform field is still produced in the lateral regions of the pixel compromising the efficiency at the corner. Two variations to the process have been proposed in order to further enhance the transversal component of electric field at the pixel borders: on a sample of chip, which includes the one in Pisa, a portion of low dose implant has been removed, creating a step discontinuity in the deep p-well corner (fig. 4.3); the second solution proposed[MOUSTAKAS THESYS, PAG 58] consists in adding an extra deep p-well near the pixel edge. A side effect of the alteration in the low dose implant is that the separation between the deep p-well and the p-substrate becomes weak to the point that they cannot be biased separately to prevent the punchthrough.

Moreover, to investigate the charge collection properties, pixels within the matrix are split between bottom top half and bottom half and feature a variation in the coverage of the deep p-well: the electronics area can be fully covered or not. In particular the pixels

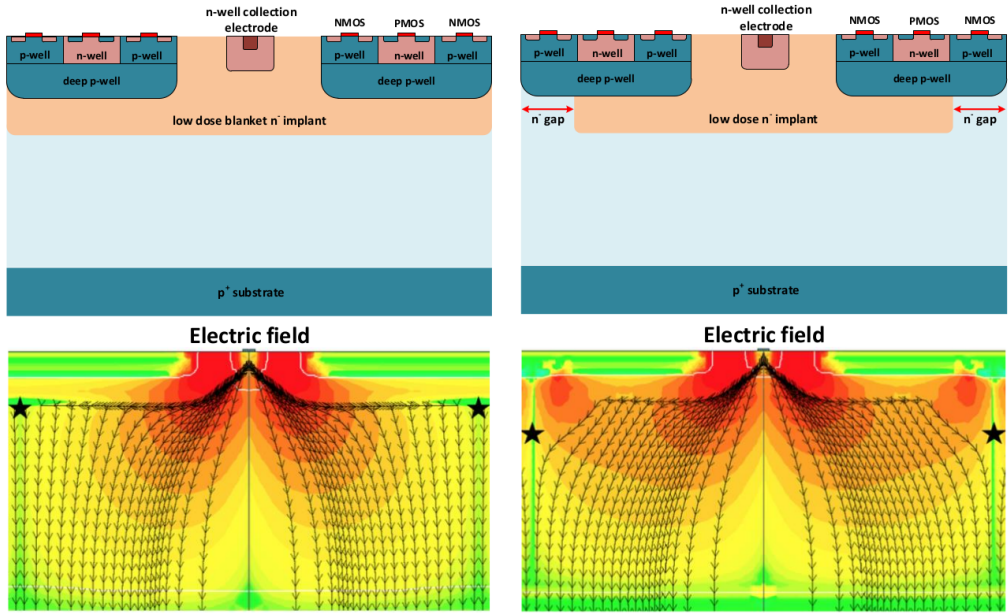


Figure 4.3: (a) The cross-section of a monolithic pixel in the TJ-Monopix with modified process; additionally in (b) a gap in the low dose implant is created to improve the collection of charge due to a bigger lateral component of the electric field. this point in figure is indicated by a star . transversal component of the electric field drops at the pixel corner

784 belonging to rows from 0 to 111 are fully covered (FDPW) and pixels belonging to rows
 785 from 112 to 223 have a reduced p-well (RDPW), resulting in a enhancement of the lateral
 786 component of the electric field.

787 4.2 Front end

788 One of the main advantage of this chip is the small collection electrode, which results in a
 789 small capacitance ($C_{in}=3\text{ fF}$) allowing for high input signal amplitude and single stage of
 790 amplification, which obviously improves the signal to noise ratio performance of the FE.
 791 Assuming a fully depleted epitaxial layer of $25\text{ }\mu\text{m}$, which corresponds approximately to
 792 a $20\text{ }\mu\text{m}$ of deep sensing volume, a MIP should produce $\sim 1600\text{ e}^-$, then:

$$V_{in} = \frac{1600\text{ e}^- \times 1.6 \cdot 10^{-19}\text{ C}}{3\text{ fF}} = 85\text{ mV} \quad (4.1)$$

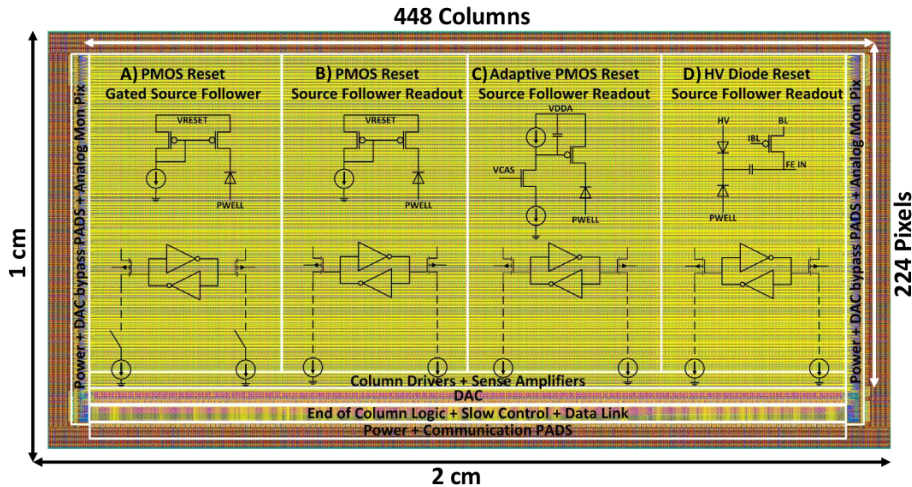
793 Secondly, a reset mechanism which slowly discharges the detector capacitance must be
 794 included in the circuit:

$$V_{in} = \frac{Q_s}{C_{in}} e^{-t/R_b C_{in}} \quad (4.2)$$

795 where R_b is the equivalent reset element. The general constraint which must be satisfied
 796 is that the discharge time $\tau = R_b C_{in}$ must be slower than the characteristic time of
 797 the amplifier, otherwise a signal loss could occurs. Traditionally the reset can be
 798 implemented in two different way: with a forward biased diode, that might be implemented
 799 by a simple p+ diffusion inside the well of the collection electrode n, or with a PMOS
 800 transistor. Despite of the semplicity of the diode reset, since it is a non-linear element,
 801 the discharge would depend on the quantity of charge Q generated on the n electrode,

802 prejudicing the linearity of the analog output (Q-ToT). To solve the issue, a PMOS reset
 803 is the method preferred in design such TJ-Monopix1 with analog output; the PMOS
 804 transistor, indeed, can acts as a constant current source and then used to discharge the
 805 sensor. Although the PMOS reset is capable of providing a constant current, it has to be
 806 manually re-tuned every time in order to restore the input DC baseline voltage; to do that
 807 a low-frequency feedback is used.

808 The matrix is split in four sections, each one corresponding to a different flavor of the
 809 FE, implemented in order to test more options.



804 Figure 4.4: TJ-Monopix1 has been developed in four different flavor. The flavor PMOS
 805 reset (B) is considered as the reference one.

806 All the flavors implement a source-follower double-column bus readout: the standard
 807 variation is the flavor B, that features a PMOS input reset (refered as "PMOS reset").
 808 Flavor A is identical to flavor B except for the realization of the source follower (it is a
 809 gated one): in the circuit of the gated versione there is a transistor more that operates on
 810 the baseline and on the feedback mechanism; this aim to reduce the power consumption
 811 and results in a higher signal baseline, and then in a lower effective threshold. C instead
 812 implements a novel leakage compensation circuit, with a PMOS reset configuration. More-
 813 over the collection electrode can be either DC-coupled to the readout electronics, as in
 814 flavors A, B, C, or AC-coupled through a metal-oxide-metal (MOM) capacitor, as in D
 815 is AC-coupled. The latter one allows applying a high bias voltage to the electrode n and
 816 for this reason the flavor D is also called "HV flavor". Unfortunately the "HV" suffer
 817 from a signal loss, which can achieve even the 50%, due to the additional parasitic capac-
 818 ity introduced at the input node. The HV voltage above which the breakdown begins is
 819 ~ 50 V; however at values bigger than 20 V, the gain does not increase anymore, since the
 820 depletion zone is already fully depleted.

821 4.2.1 ALPIDE-like

822 ALPIDE chips, developed by the ALICE collaboration, implemented a standard FE to the
 823 point that many CMOS MAPS detectors used a similar FE and are called "ALIPDE-like".
 824 Considering that both TJ-Monopix1 and ARCADIA-MD1 have an ALPIDE-like FE, I am
 825 going to explain the broad principles of the early FE stage. The general idea is of the
 826 amplification to transfer the charge from a bigger capacity[15], C_{source} , to a smaller one,

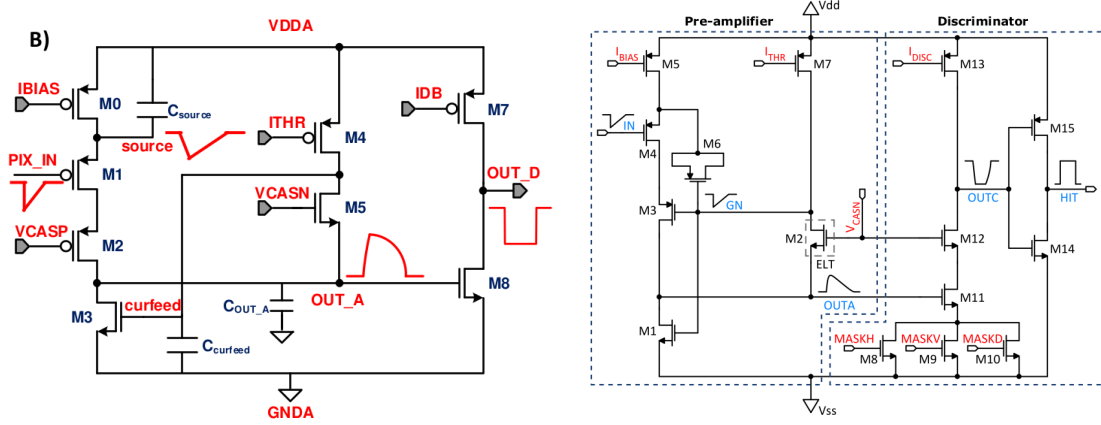


Figure 4.5

831 C_{out} : the input transistor M1 with current source IBIAS acts as a source follower and this
 832 forces the source of M1 to be equal to the gate input $\Delta V_{PIX_IN} = Q_{IN}/C_{IN}$.

$$Q_{source} = C_{source} \Delta V_{PIX_IN} \quad (4.3)$$

833 The current in M2 and the charge accumulates on C_{out} is fixed by the one on C_{source} :

$$\Delta V_{OUT_A} = \frac{Q_{source}}{C_{OUT_A}} = \frac{C_{source} \Delta V_{PIX_IN}}{C_{OUT_A}} = \frac{C_{Source}}{C_{OUT_A}} \frac{Q_{IN}}{C_{IN}} \quad (4.4)$$

834 A second branch (M4, M5) is used to generate a low frequency feedback, where VCASN
 835 and ITHR set the baseline value of the signal on C_{OUT_A} and the velocity to goes down
 836 to the baseline. **IL RUOLO DI CURVFEED NON L'HO CAPITO.** Finally IDB defines
 837 the charge threshold with which the signal OUT_A must be compared: depending on if
 838 the signal is higher than the threshold or not, the OUT_D is high or low respectively.

839 The actual circuit implemented in TJ-Monopix1 is shown in figure 4.5: the principal
 840 difference lays in the addition of disableing pixels' readout. This possibility is uttermost
 841 important in order to reduce the hit rate and to avoid saturating the bandwidth due to the
 842 noisy pixels, which typically are those with manufacturing defects. In the circuit transis-
 843 tors M8, M9 and M10 have the function of disabling registers with coordinates MASKH,
 844 MASKV and MASKD (respectively vertical, orizontal and diagonal) from readout: if all
 845 three transistors-signals are low, the pixel's discriminator is disabled. Compared with a
 846 configurable masking register which would allow disableing pixels individually, to use a
 847 triple redundancy reduces the sensistivity to SEU but also gives amount of intentionally
 848 masked ("ghost") pixels. This approach is suitable only for extremely small number N of
 849 pixel has to be masked: if two coordinate projection scheme had been implemented, the
 850 number of ghost pixels would have scale with N^2 , if instead three coordinates are used,
 851 the N's exponential is lower than 2 (fig. 4.6)

852 Foto dell'oscilloscopio per far vedere cosa fanno i parametri

853 4.3 Readout logic

854 TJ-Monopix1 has a triggerless, fast and with ToT capability R/O which is based on a
 855 column-drain architecture. On the pixel are located two Random Access Memory (RAM)
 856 cells to store the 6-bit LE and 6-bit TE of the pulse, and a Read-Only Memory (ROM)

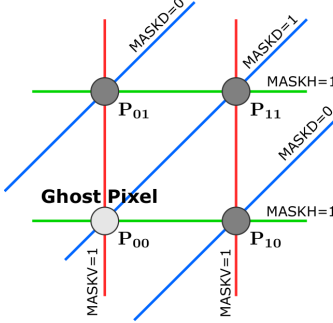


Figure 4.6

Parameter	Meaning	
IBIAS	mainly controls the rise time	yes
IDB	sets the discriminator threshold	yes
ITHR	sets the velocity of the return to the baseline	yes
ICASN	sets the baseline of the signal	yes
VRESET	sets the gain of the preamplifier	yes
IRESET	sets the gain of the preamplifier	no

Table 4.3: FE parameters which must be setted through the DAQ. "Function" means that higher parameter implies higher value

857 containing the 9-bit pixel address. Excluded these memories, TJ-Monopix1 hasn't any
 858 other buffer: if a hit arrives while the pixel is already storing a previous one, the new
 859 data get lost. After being read, the data packet is sent to the EoC periphery of the
 860 matrix, where a serializer transfers it off-chip to an FPGA (4.7). There a FIFO is used
 861 to temporarily stored the data, which is transmitted to a computer through an ethernet
 862 cable in a later time.

863 The access to the pixels' memory and the transmission of the data to the EoC, following
 864 a priority chain, is managed by control signals and is based on a Finite State Machine
 865 (FSM) composed by four state: no-operation (NOP), freeze (FRZ), read (RD) and data
 866 transfer (DTA). The readout sequence (??) starts with the TE of a pulse: the pixel
 867 immediately tries to grab the column-bus turning up a hit flag signal called *token*. The
 868 token is used to control the priority chain and propagates across the column indicating
 869 what pixel that must be read. To start the readout and avoid that the arrival of new hits
 870 disrupt the priority logic, a *freeze* signal is activated, and then a *read* signal controls the
 871 readout and the access to memory. During the freeze, the state of the token for all pixels
 872 on the matrix remains settled: this does not forbid new hits on other pixels from being
 873 recorded, but forbids pixels hit from turning on the token until the freeze is ended. The
 874 freeze stays on until the token covers the whole priority chain and gets the EoC: during
 875 that time new token cannot be turned on, and all hits arrived during a freeze will turn
 876 on their token at the end of the previous freeze. Since the start of the token is used to
 877 assign a timestamp to the hit, the token time has a direct impact on the time resolution
 878 measurement; this could be a problem coping with high hits rate.

879 The analog FE circuit and the pixel control logic are connected by an edge detector
 880 which is used to determine the LE and the TE of the hit pulse(fig. 4.9): when the TE

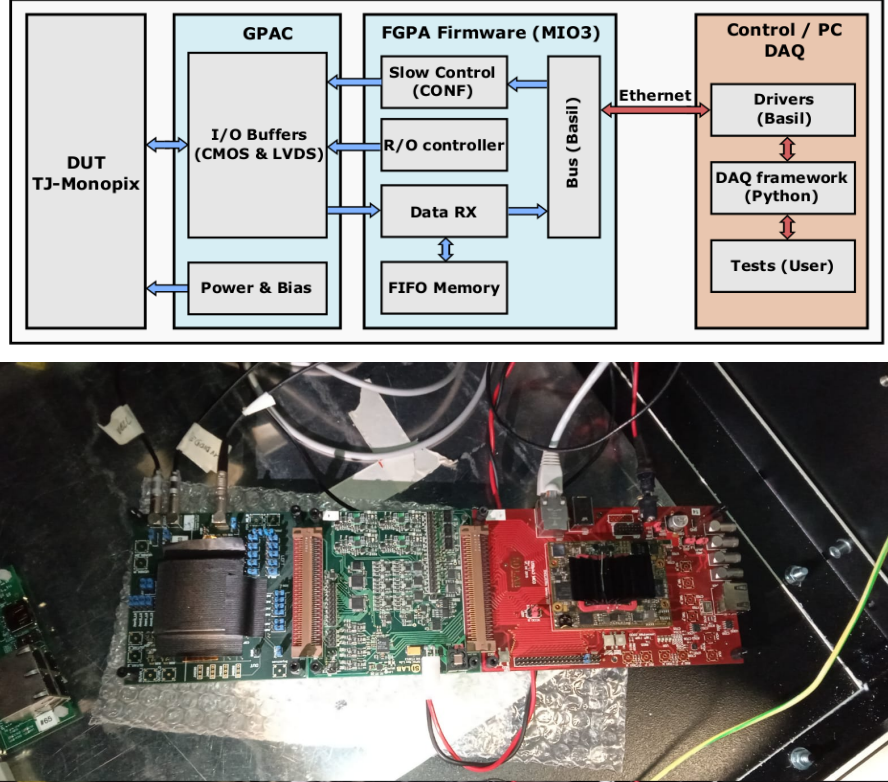
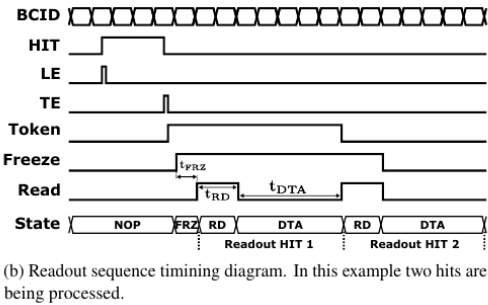


Figure 4.7: Main caption



(b) Readout sequence timing diagram. In this example two hits are being processed.

Figure 4.8: Readout timing diagram: in this example two hits are being processed

is stored in the first latch the edge detector is disabled and, if the **FREEZE** signal is not set yet, the readout starts. At this point the **HIT** flag is set in a second latch and a **Token** signal is produced and depending on the value of **Token** in the pixel can be read or must wait until the **Token in** is off. In figure an OR is used to manage the token propagation, but since a native OR logic port cannot be implemented with CMOS logic, a sum of a NOR and of an inverter is actually used; this construct significantly increases the propagation delay (the timing dispersion along a column of 0.1-0.2 ns) of the token and to speed up the circuit optimized solution are often implemented. When the pixel become the next to be read in the queue, and at the rising edge of the **READ** signal, the state of the pixel is stored in a D-latch and the pixel is allowed to use the data bus; the **TE** and the **HIT** flag latches are reset and a **READINT** signal that enable access of the RAM and ROM cells is produced.

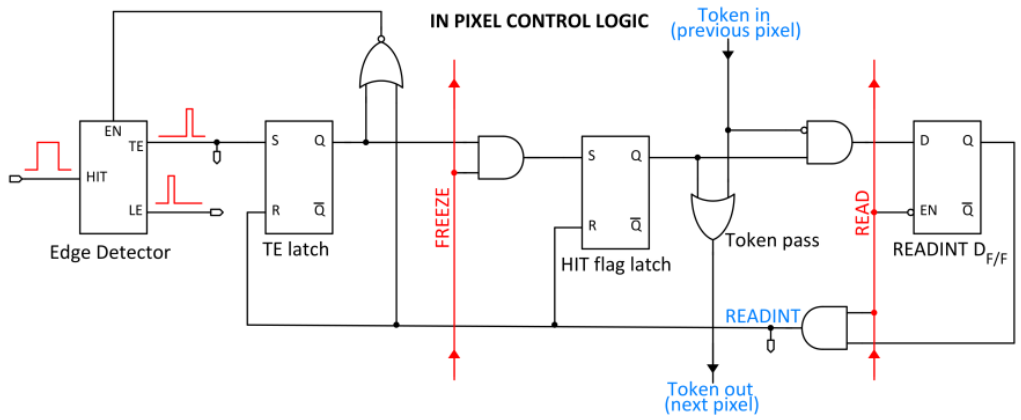


Figure 4.9

893 The final data must provide all the hits' information: the pixel address, the ToT and
 894 the timestamp. All those parts are assigned and appended at different time during the
 895 R/O chain:

- 896 • **Pixel address:** while the double column address (6-bit) is appended by the EoC
 897 circuit, the row address (8-bits for each flavor) and the physical column in the doublet
 898 (1-bit) are assigned by the in-pixel logic
- 899 • **ToT:** is obtained offline from the difference of 6-bits TE and 6-bits LE, stored by
 900 the edge detector in-pixel; since a 40 MHz BCID is distributed across the matrix,
 901 the ToT value is range 0-64 clock cycle which corresponds to 0-1.6 μ s
- 902 • **Timestamp:** The timestamp of the hit correspond to the time when the pixel set
 903 up the token; it is assigned by the FPGA, that uses the LE, TE and a 640 MHz
 904 clock to derive it. For all those hits which arrived while the matrix is frozen, the
 905 timestamp is no more correlated with the time of arrival of the particle

906 When the bits are joined up together the complete hit data packet is 27-bit.

907 **Chapter 5**

908 **Arcadia-MD1**

909 [16] [17]

910 Breve introduzione analoga a Monopix1 in cui descrivo brevemente la "timeline" da
911 SEED Matisse a Md1 e Md2

912 Tutti i minid, siano essi v1 o v2, sono Alpide like. Le differenze tra Alpide e bulk driven
913 sono un po' più complesse di quanto hai scritto. Si tratta proprio di due architetture di-
914 verse. Il primo amplifica il segnale attraverso il trasferimento di carica tra due capacità.
915 Se sei interessata ai dettagli, è spiegato molto bene in questo articolo: "Front end op-
916 timization for the monolithic active pixel sensor of the ALICE Inner Tracking System
917 upgrade" Nel bulk driven invece il guadagno è dato dal rapporto tra due transconduc-
918 tanze. Anche qui, se desideri approfondire te lo posso spiegare, ma preferibilmente a voce
919 in una stanza zoom :) Inoltre ci sono altre differenze, il bulk driven è più sensibile alle
920 cadute di tensione sul ground (che ahimè è esattamente ciò che accade nei dimostratori
921 che abbiamo ora, a causa dell'anomalo consumo di corrente dal digitale, altro baco che
922 abbiamo corretto nella terza sottomissione). Il bulk driven però permette di impostare
923 una tensione al diodo di 1V, contro gli 800 mV dell'Alpide, cosa che non saprei ripeterti
924 perché, ma Lucio dovrebbe dirci che è un pregio. Anche i livelli di tensione nei nodi interni
925 dei due front-end differiscono e il meccanismo di clipping che funzionava per l'Alpide non
926 è applicabile al bulk driven. Di conseguenza abbiamo un bias in più (ICLIP) nel secondo
927 flavour per controllare il clipping. Nell'Alpide il clipping c'è, ma l'architettura usata per-
928 mette di non aver bisogno di un bias esterno, anche se in una versione di Alpide di ALICE
929 hanno scelto di controllare comunque la corrente di clip esternamente, per una maggiore
930 flessibilità. Infine alcuni bias che hanno lo stesso nome nei due flavour, perché svolgono la
931 stessa funzione, differiscono nel valore di configurazione di default.

932 Tra i wafer fabbricati finora ci sono 3 valori di spessore attivo nominale (lo spessore
933 effettivo può variare di qualche micron ripetto a quello nominale): 48um, 100um e 200um.
934 In allegato un'immagine con le cross section.

935 **5.1 The sensor**

936 ARCADIA-MD1 is an LFoundry chip which implements the technology 110 nm CMOS
937 node with six metal layer **??**. The standard p-type substrate was replaced with an n-type
938 floating zone material, that is a technique to produce purified silicon crystal. (pag 299
939 K.W.).

940

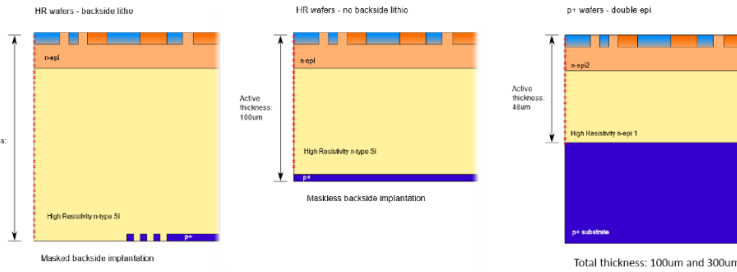


Figure 5.1

941 Wafer thinning and backside lithography were necessary to introduce a junction at the
 942 bottom surface, used to bias the substrate to full depletion while maintaining a low voltage
 943 at the front side.

944 C'è un deep pwell per - priority chainseparare l'elettronica dal sensore; per controllare il
 945 punchthought è stato aggiunto un n doped epitaxial layer having a resistivity lower than
 946 the substrate.

947 It is part of the cathegory of DMAPS Small electrode to enhance the signal to noise
 948 ratio.

949 It is operated in full depletion with fast charge collection by drift.

950 Prima SEED si occupa di studiare le prestazioni: concept study with small-scale test
 951 structure (SEED), dopo arcadia: technology demonstration with large area sensors Small
 952 scale demo SEED(sensor with embedded electronic developement) Quanto spazio dato
 953 all'elettronica sopra il pwell e quanto al diodo. . .

954 5.2 Readout logic and data structure

955 5.2.1 Matrix division and data-packets

956 The matrix is divided into an internal physical and logical hierarchy: The 512 columns are
 957 divided in 16 section: each section has different voltage-bias + serializzatori. Each section
 958 is devided in cores () in modo che in ogni doppia colonna ci siano 1Pacchetto dei dati 6
 959 cores. ricordati dei serializzaatori: sono 16 ma possono essere ridotti ad uno in modalità
 spazio

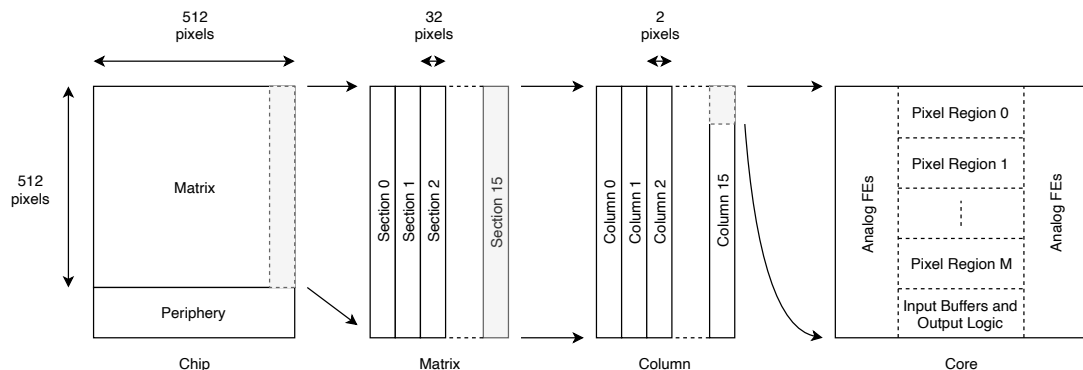


Figure 5.2

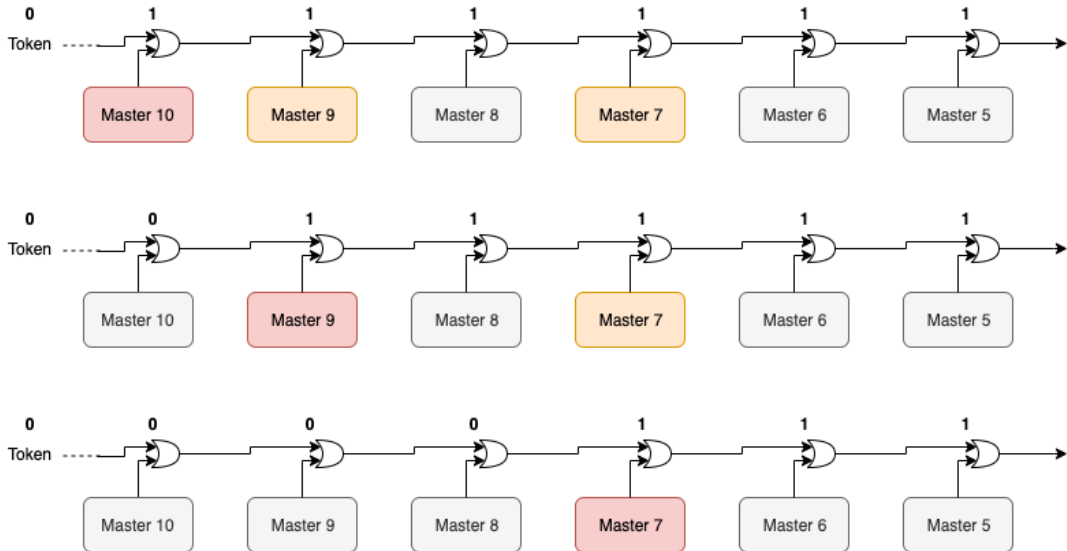


Figure 5.3

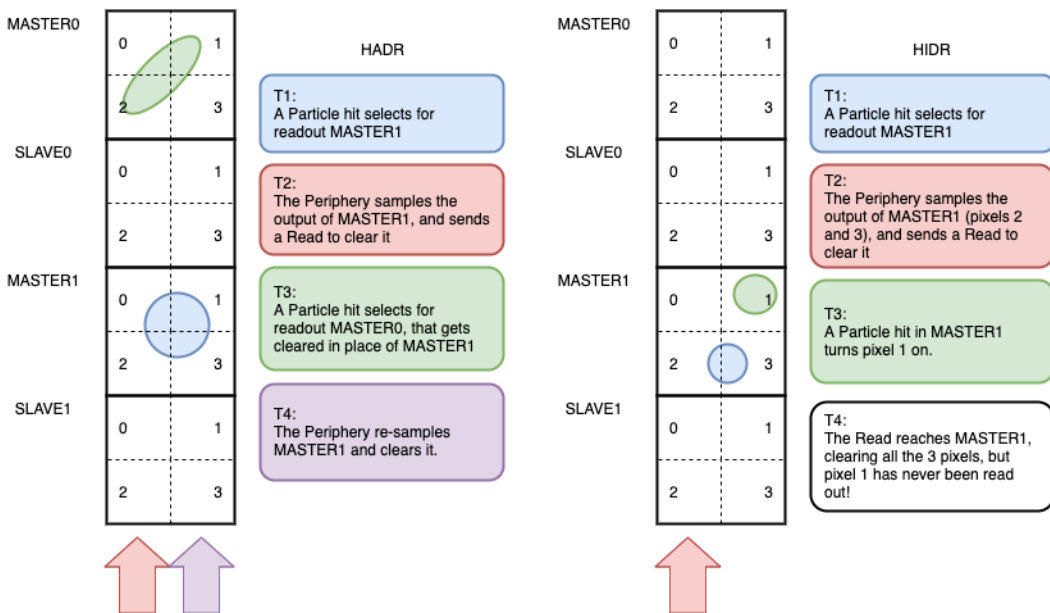


Figure 5.4

961 Questa divisione si rispecchia in come sono fatti i dati: scrivi da quanti bit un dato è
 962 fatto e le varie coordinate che ci si trovano dentro; devi dire che c'è un pixel hot e spieghi
 963 dopo a cosa serve, e devi accennare al timestamp

964 "A core is simply the smallest stepped and repeated instance of digital circuitry. A
 965 relatively large core allows one to take full advantage of digital synthesis tools to imple-
 966 ment complex functionality in the pixel matrix, sharing resources among many pixels as
 967 needed.". pagina 28 della review.

968

969 TABELLA: con la gerarchia del chip Matrix (512x512 pixels) Section (512x32 pixels)
 970 Column (512x2) Core (32x2) Region (4x2)

971 Nel chip trovi diverse padframe: cosa c'è nelle padframe e End of section.

972 "DC-balance avoids low frequencies by guaranteeing at least one transition every n

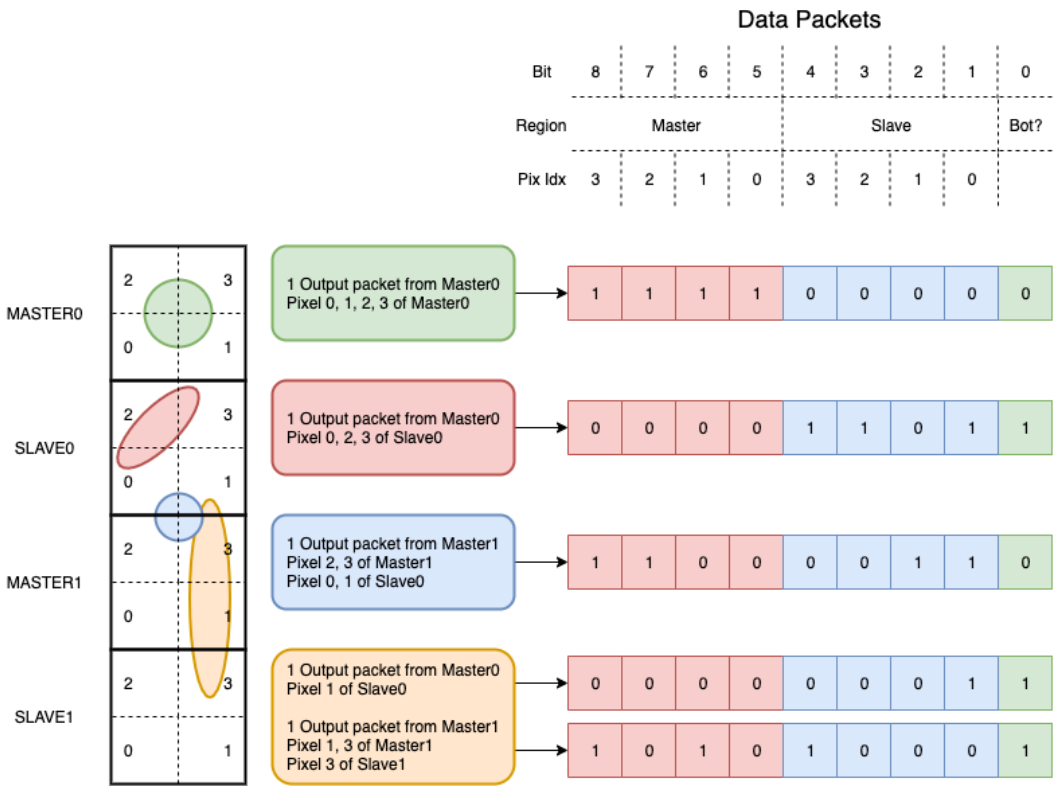
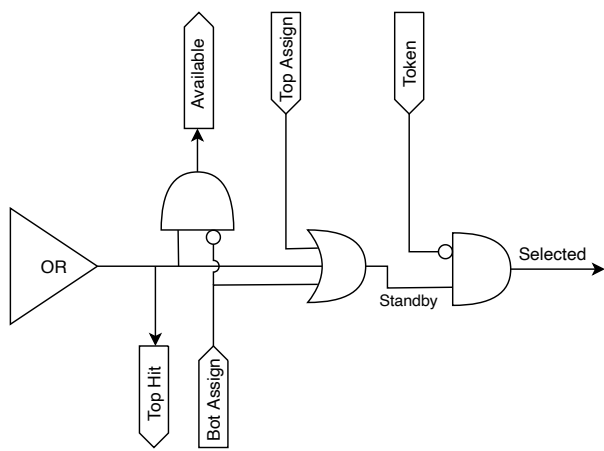


Figure 5.5

Master Region



Slave Region

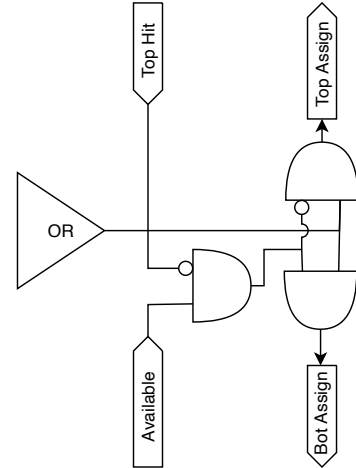


Figure 5.6

973 bits; for example 8b10b encoding n = 5"

974 **Chapter 6**

975 **Characterization**

976

- 977 • rifai il conto della lunghezza di attenuazione. Ho trovato (presentazione Luciano
- 978 Mus) 29 um per ka e 37 um per kb.
- 979 • Con il PMOS la configurazione del FE di default è: e richiama i significati delle
- 980 variabili.
- 981 • parla dell HV

982 **6.1 TJ-Monopix1 characterization**

983 **6.1.1 Threshold and noise: figure of merit for pixel detectors**

984 A characterization of threshold and noise is typically necessary since these values have an
985 impact on the operating conditions and on the performance of the chips, so much that
986 the signal to threshold ratio may be considered as the figure of merit for pixel detectors
987 rather than the signal to noise ratio. The mean minimum stable threshold evolved through
988 different generation of chips: in the 1st generation it was around 2500 e^- while in the 3rd
989 (corresponding to nowadays chips) is less than 500 e^- . This allows in thinner sensors with
990 smaller signals: from $16\,000\text{ e}^-$ produced in $200\text{ }\mu\text{m}$, the signal expected moved down to
991 2000 e^- produced in $25\text{ }\mu\text{m}$. According with this, the threshold of TJ-Monopix1 is around
992 500 e^- .

993 Obviously the threshold has to be located between the noise peak around the baseline
994 and the signal distribution, in particular it has to be low enough to mantain a high signal
995 efficiency, but also high enough to cut the noise: for a low threshold many pixels can fire
996 at the same time and a positive feedback can set off a chain reaction eventually, causing
997 all the other pixels to fire. Thus, the noise sets a lower bound to the threshold: if an
998 occupancy $\leqslant 10^{-4}$ is required, for example, this correspond to the Gaussian 1-sided tail
999 fraction for 3.7σ . In this case, if the noise is 100 e^- (resonable), the threshold must be
1000 higher than $3.7 \times 100\text{ e}^-$. Typically this argument sets only a minimal bound to the
1001 threshold since the variation with time and from pixel to pixel have to be taken into
1002 account: the temperature, the annealing (for example, the radiation damages in the oxide
1003 layer causes shift of MOSFET threshold voltage) and the process parameters variation
1004 across the wafer (as for example process mismatch between transistors).

Given that the first stage of amplification is the most crucial, since in the following stages the signal amplitude is high compared to additional noise, the noise is valued at the preamplifier input node. Then, the noise is parameterized as Equivalent Noise Charge (ENC), which is defined as the ratio between the noise N at the output expressed in Volt and the out voltage signal S produced by 1 e⁻ entering in the preamplifier:

$$ENC = \frac{N_{out}[V]}{S_{out}[V/e^-]} = \frac{V_{noise}^{RMS}}{G} \quad (6.1)$$

with G expressed in V/e⁻; as the gain increases, the noise reduces . **Servirebbe una misura**
Considering the threshold dispersion a requirement for the ENC is:

$$ENC < \sqrt{(T/3.7)^2 - T_{RMS}^2(x) - T_{RMS}^2(t)} \quad (6.2)$$

where the T is the threshold setted, T_{RMS} is the threshold variation during time (t) and across the matrix (x); a typical reasonable value often chosen is 5 ENC.

Because of the changing of the 'real' threshold, the possibility of changing and adapting the setting parameters of the FE, both in time and in space is desiderable: these parameters are usually set by Digital to Analog Converter (DAC) with a number of bit in a typical range of 3-7. Unfortunately DAC elements require a lot of space that may be not enough on the pixel area; therefore, the FE parameters are typically global, which means that they are assigned for the whole chip, or they can be assigned for regions the matrix is divided into. The former case corresponds to TJ-Monopix1's design in which 7 bits are used for a total 127-DAC possible values, while the latter corresponds to the ARCADIA-MD1's one, **where quanti bit??**. An other possibility, for example implemented in TJ-Monopix2, is allocate the space on each pixel for a subset of bits, then combinig the global threshold with a fine tuning. If so, the threshold dispersion after tuning is expected to be inversely proportional to the tuning DAC number of bits and thus be improved a lot:

$$\sigma_{THR,tuned} = \frac{\sigma_{THR}}{2^{nbit}} \quad (6.3)$$

where σ_{thr} is the RMS of the threshold spread before tuning.

To measure the threshold and noise of pixels a possible way is to make a scan with different known injected charge: the threshold corresponds to the value where the efficiency of the signal exceeds the 50%, and the ENC is determined from the width of this edge. Following this path, I have used the injection circuit available on the chip to inject 100 pulses for each input charge for a fixed threshold. The injection comes on a capacity at the input of the FE circuit, whose mean value is 230 aF and from which the conversion factor from DAC units to electrons can be obtained: for the PMOS flavor, for example, since the DAC are biased at 1.8 V, the Least significant Bit (LSB) corresponds to a voltage of 14.7 mV from which the charge for LSB 1.43 e⁻/mV and the conversion factor therefore is 20.3 e⁻/DAC. While this value is equivalent for all the PMOS flavor, the HV flavor is expected to have a different conversion factor, ~ 33 e⁻/DAC, beacuse of the different input capacity.

Besides the charge, also the duration and the period of the injection pulse can be set; it is important to make the duration short enough to have the falling edge during the dead time of the pixel (in particular during the FREEZE signal) in order to avoid the undershoot, coming at high input charge, triggering the readout and reading spurious hits. Since the injection circuit is coupled in AC to the FE, if the falling edge of the pulse is sharp enought to produce ad undershoot, this can be seen as a signal.

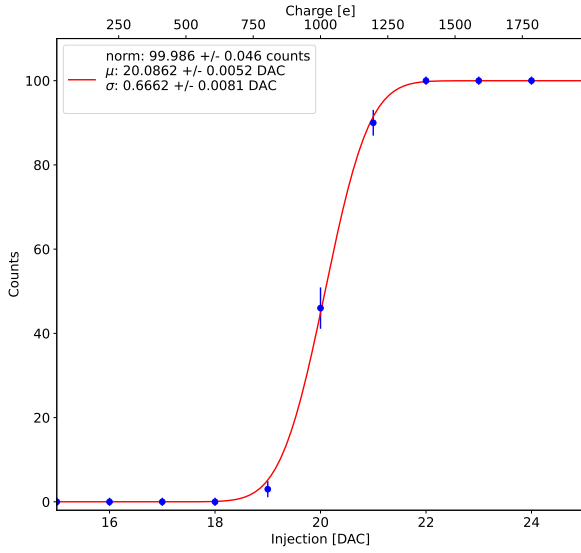


Figure 6.1: S-curve for pixel (10, 10) of the PMOS flavor (flavor 1) with IDB fixed at 40 DAC. The conversion of charge injected from DAC to electrons has been done assuming a conversion factor of 20 e⁻/DAC.

	DAC units	electrons
Threshold	24.529 ± 0.049	511.0 ± 1.0
Threshold dispersion	1.848 ± 0.033	36.96 ± 0.66
Noise	0.8222 ± 0.0043	16.444 ± 0.086
Noise dispersion	0.0975 ± 0.0030	1.95 ± 0.06

Table 6.1: Flavor PMOS, IDB fixed at 40 DAC

1045 Assuming a gaussian noise, the efficiency of detecting the signal can be described
1046 through a modification of the error function:

$$f(x, \mu, \sigma) = \frac{1}{2} \left(1 + \text{erf} \left(\frac{x - \mu}{\sigma \sqrt{2}} \right) \right) \quad (6.4)$$

1047 **with:** where the threshold and the ENC corresponds to the μ and σ . Therefore I perform
1048 a fit of the counts detected using the function in equation 6.4. In figure 6.1 there is an
1049 example with IDB equal to 40 DAC of fit for a pixel belonging to the flavor B, while in
1050 table 6.1 and figure ?? there are the histograms and the maps of the parameters of the
1051 scurve-fit. As expected, the flavor PMOS reset gated (A), thanks to the transistor which
1052 change the baseline value, has a lower threshold and noise

1053 Small threshold variations has been observed in the first biasing section (columns from
1054 0 to 14) with IDB=40 DAC; the same structure appears more evident at other different
1055 IDBs, as for example 100 DAC **Plot of the average threshold per column al variare di IDB**.
1056 The systematic threshold variation across the biasing group has not a known motivation,
1057 but one could certainly be the transistor mismatch of the biasing DAC registers IDB
1058 and ICASN, which both adjust the effective threshold (I recall that ICASN regulate the
1059 baseline, and in this measurements it was set to the minimin possible value).

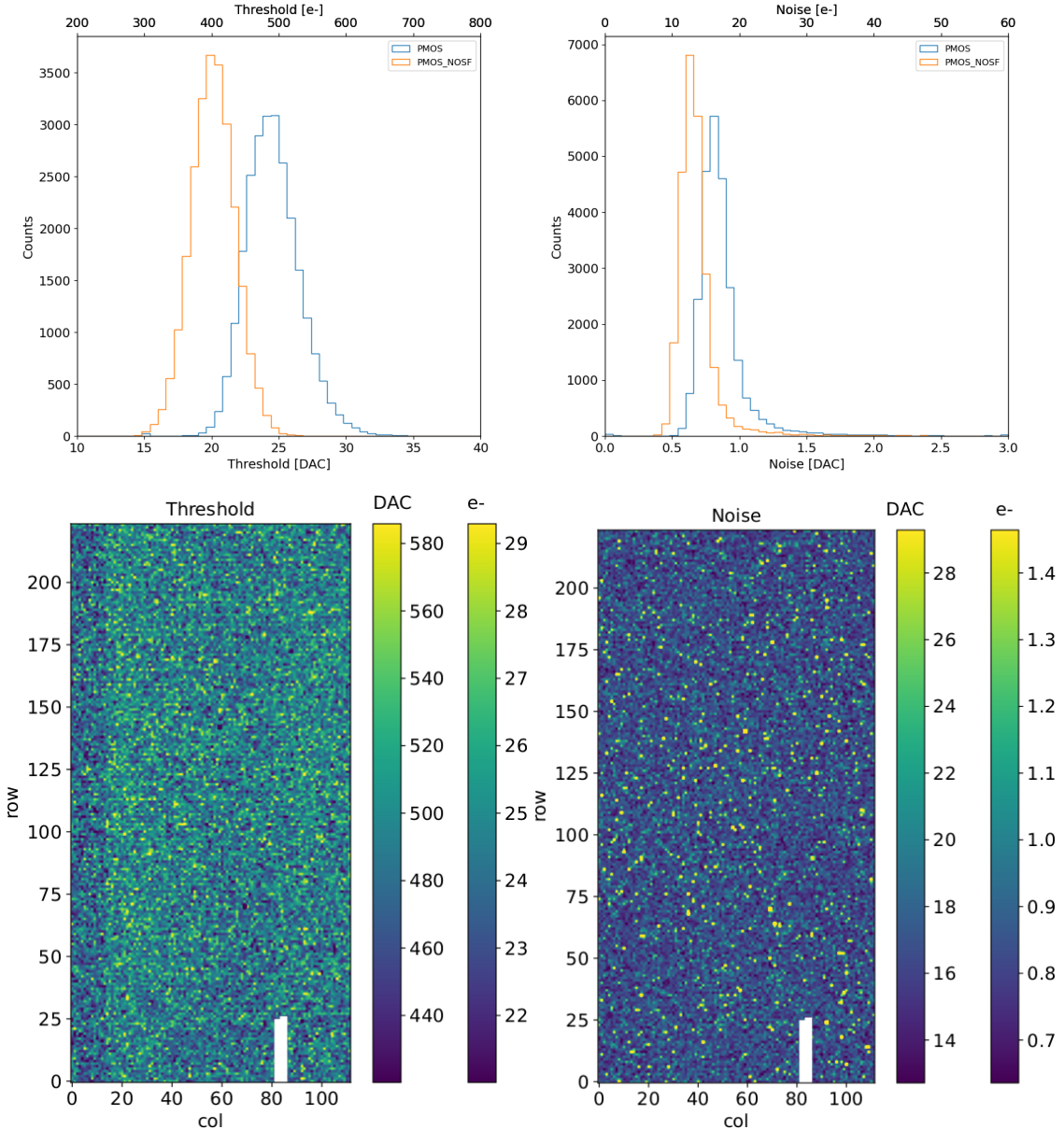


Figure 6.2: Histograms of the threshold (a) and the noise (b) found fitting the s-curve of all flavor with IDB fixed at 40 DAC. Below there are the maps of the threshold (a) and the noise (b), respectively, found fitting the s-curve with IDB fixed at 40 DAC for the PMOS flavor (B). The white pixels have the injection circuit broken.

1060 To verified the trend of the threshold as a function of the front end parameter IDB and
 1061 find its dynamic range, I have permormed different scans changing the IDB: I have injected
 1062 the whole matrix and found the means and the standard deviation of the distributions. The
 1063 results are shown in figure 6.3: the blue points are the mean threhsold found whithin the
 1064 matrix, while in green is shown the width of the threshold distribution, aka the threshold
 1065 dispersion. While the threshold increases, the ENC decreases of $\sim 4 \text{ e}^-$,which is $\sim 1/3$ of
 1066 the noise at IDB=40 DAC.

1067 Then, to evaluet the operation and the occupancy of the chip at different threshold
 1068 I have made long acquisitions of noise at different IDB and check how the number of
 1069 pixel masked changes with the threshold. The masking algorithm I have used search for

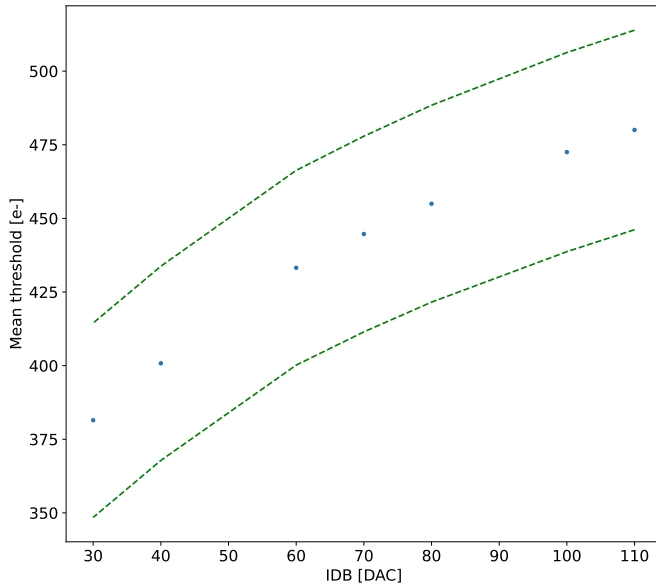


Figure 6.3: Flavor PMOS (B) with Psub-Pwell biased at -6 V. Threshold measured in electrons vs the register which sets the threshold, IDB.

1070 pixels with rate >10 Hz and mask them. With such algorithm, in our standard condition,
 1071 IDB=40 DAC, a very low noise hit rate is intentionally achieved masking only **dozen of**
 1072 **pixels?** of the whole flavor, and other **quanti** are unintentionally masked.

1073 6.1.2 Linearity of the ToT

1074 I have already said in chapter 4 that TJ-Monopix1 returns an output signal proportional to
 1075 the charge released by a particle in the epitaxial layer, which is the Time over Threshold;
 1076 the ToT is saved as a 6-bit variable and then has a dynamic range equal to 0-64, which
 1077 corresponds to 0 μ s to 1.6 μ s assuming a clock frequency of 40 MHz. When a pulse is longer
 1078 than 1.6 μ s the counter rolls back to zero and there is no way to distinguish that charge
 1079 from a lower one with the same ToT: that is the rollover of the ToT (??(a)).

1080 In order to associate the ToT (in range 0-64) to the charge, a calibration of the signal
 1081 is necessary. Assuming the linearity between ToT and the charge, Q can be found:

$$Q [DAC] = \frac{(ToT [au] - q [au])}{m [au/DAC]} \quad (6.5)$$

1082 where m and q are the fitted parameters of the calibration. It is important to keep in mind
 1083 that the main application target of TJ-Monopix1 is in the inner tracker detector of HEP
 1084 experiments, then the main feature is the efficiency, then a rough calibration of the signal
 1085 to charge is fine. The ToT information can be used both to better reconstruct the charge
 1086 deposition in cluster in order to improve the track resolution, and for particle identification,
 1087 especially for low momentum particles which do not reach the proper detectors.

1088 The study of the output signal is made possible via the injection: since the pulses are
 1089 triangular, the ToT is expected to be almost linear depending on the injection charge value.
 1090 To verify this statement and study the deviations from linearity I've fit the ToT versus the

	PMOS 0	PMOS 1	PMOS 2	HV
Slope [au/DAC]	0.75566 ± 0.00149	0.57145 ± 0.00025		
Slope dispersion [au/DAC]	0.03841 ± 0.00037	0.01685 ± 0.00016		
Intercept [au]	-11.6070 ± 0.0089	-10.824 ± 0.019		
Intercept dispersion [au]	1.5176 ± 0.0063	1.225 ± 0.013		

Table 6.2: Mean calibration parameters for all flavor and their dispersion on the matrix.

charge injected for all pixel within the matrix. In figure ??(b) there is an example of fit for a pixel belonging to the flavor B, while in figure 6.5 there are the histograms and the maps of the parameters of the line-fit for all flavors with IDB fixed at 40 DAC. Here again a difference between biasing section appears: since the slope of the ToT is related with the gain of the preamplifier (increasing the gain also increases the ToT), the mismatch is probably due to the transistor contributing to the amplification stage.

Before performing the fit I have calculated the mean value of the ToT of the pulses recorded for each pulse amplitude and I used the mean ToT as value for the fit. The aim of the calibration obviously is finding a relation only in the range 0-64 without taking into account the rolling over hits: therefore, to prevent the rollover data from reducing the mean ToT introducing a bias in the mean value, I cut and I did not consider them. If a signal bigger than the $1.6 \mu\text{s}$ is expected in the usage of the detector, the threshold must be raised or the gain reduced, making the expected output signal in range 0-64. In figure ??(b) are shown both the fits with a line (red) and with a second order polynomial (green): at the bounds of the ToT range values deviate from the line model. Since the deviation is low than 1% and it only interest the region near the 0 and the 64, in first approximation it is negligible.

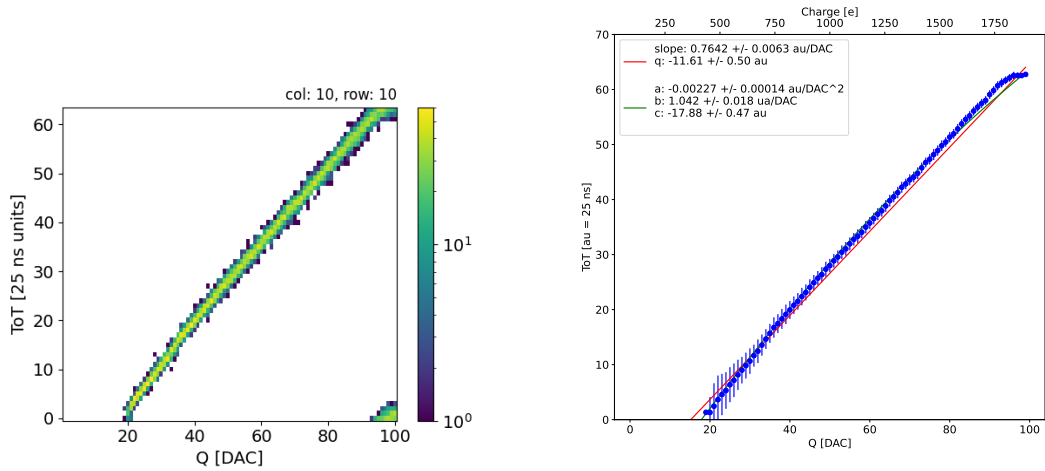


Figure 6.4: The figures refer to pixel (10,10) of the PMOS-reset flavor (1) with IDB fixed at 40 DAC for the PMOS flavor (B). (a) Histogram of the injection pulses: the ToT is in range 0-64 since it is represented by 6 bit, so when achieving the 64 it rolls over back to the zero. (b) Mean ToT vs the the charge: the mean has been calculated cutted the rolling hits.

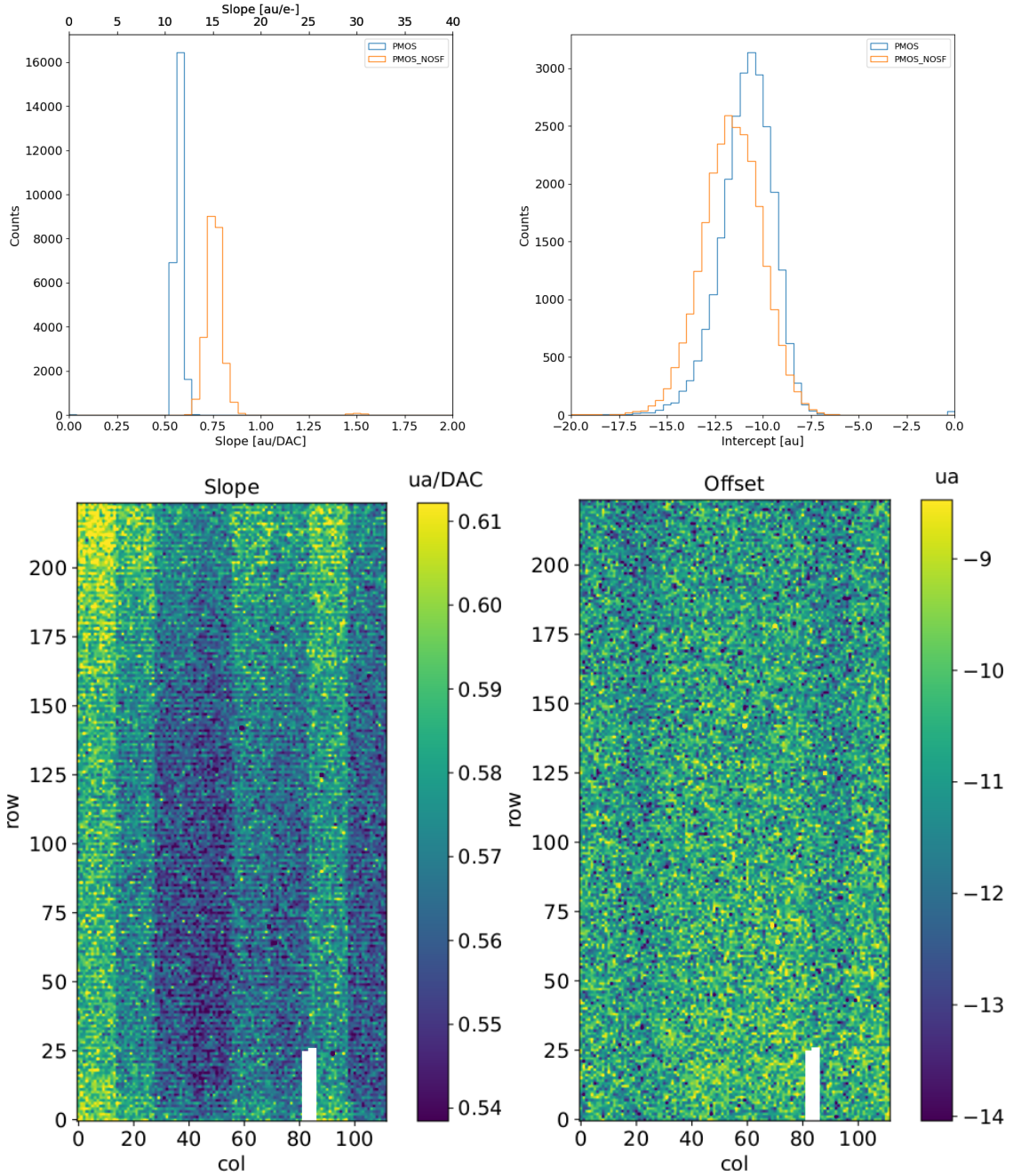


Figure 6.5: Histograms of the calibration parameters, slope (a) and offset (b), found fitting the ToT with a line, for all flavor and with IDB fixed at 40 DAC. Maps of the calibration parameters, slope (a) and offset (b), found fitting the ToT with a line, with IDB fixed at 40 DAC

6.1.3 Calibration of the ToT

Considering that the charge injected in the FE goes to fill capacitor which is different from pixel to pixel, the true charge injected does not correspond to what expected assuming C equal to 230 aF, the nominal value. Accordingly to that, a verification of the value provided and an absolute calibration of this capacity and of the conversion factor F is needed to have a correspondence of the signal in electrons; assuming C 230 aF, F is expected to be

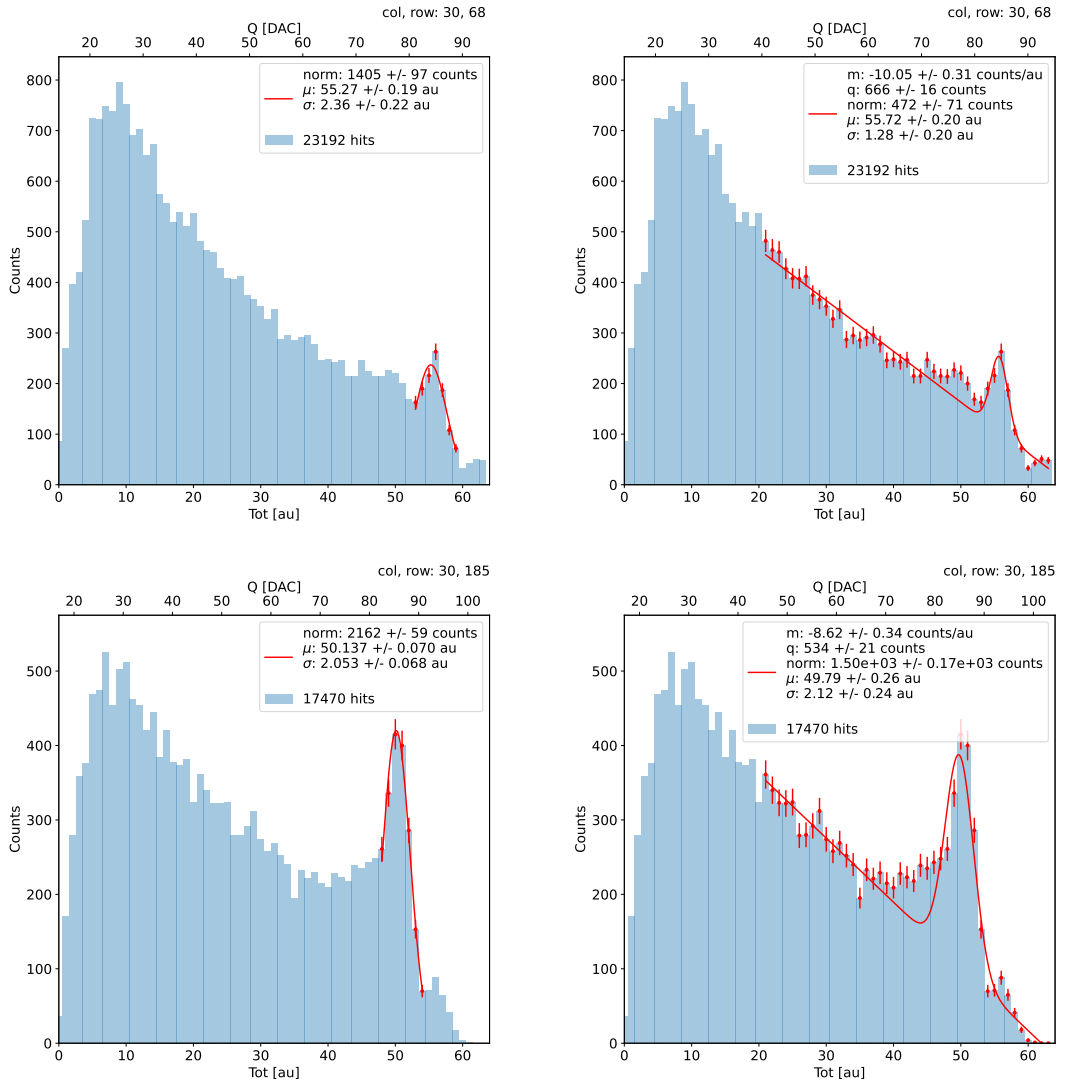


Figure 6.6: due pixel per far vedere la differenza tra i fit. Sottolinea che in rosso ci sono i bin fittati. La doppia scala utilizza le info trovate nel paragrafo precedente per il dato pixel in questione. Per avere una corrispondenza grezza in elettroni basta moltiplicare per 20 e- / dac.

1114 20 e-/DAC, and is defined as:

$$F[e- / DAC] = \frac{1616 e-}{Q [DAC]} \quad (6.6)$$

1115 For this purpose a Fe55 radioactive source has been employed; the Fe55 is an extremely
 1116 important radionuclide in the calibration of X-ray spectrometers, proportional counter
 1117 and scintillator detector since it emits two X-photons during the electron capture
 1118 decay: the first one (K_α) at 5.9 keV and the second one (K_β) at 6.5 keV. The K_α photon,
 1119 which does photoelectric effect in the silicon, has an absorption length $\lambda=7 \mu\text{m}$ to $8 \mu\text{m}$,
 1120 and the probability of being absorbed in the $25 \mu\text{m}$ thick epitaxial layer is ~ 0.95 . The
 1121 electron emitted has an energy equal to the photon one, so recalling that the mean energy
 1122 needed to produce a couple electron-vacuum is 3.65 eV, the signal produced by the Fe55
 1123 source is expected to be 1616 e-. In figures ?? and ?? are shown two histograms of the

1124 ToT spectrum of the Fe55 source for two different pixels. The peak corresponds to the
 1125 events with completely absorption of the charge produced in the depleted region, while
 1126 the long tail on the left to all the events with partial absorption due to charge sharing
 1127 among neighbors pixels. In order to reduce the charge sharing, the pixel dimension in
 1128 TJ-Monopix2 has been reduced down to $30 \times 30 \mu\text{m}^2$. The events on the right side of the
 1129 peak, instead, corresponds to the K_β photons. Looking at the histograms for pixel (30,
 1130 185) and (30,69) a significant difference in the peak to tail ratio leaps out. This difference
 1131 in the efficiency of detecting the signal can be related with the position of the pixel in
 1132 the matrix: in particular pixels in the upper part of the matrix (rows 112-224) have a
 1133 more prominent peak, while in pixels in the lower part (rows 0-111) there is a higher
 1134 partial absorption. I recall now that there is a slightly difference in the structure of the
 1135 low dose-epi layer (??) among the rows in the matrix, in particular pixels in rows 112-224
 1136 are supposed to have a higher efficiency in the pixel corner.

1137 For the calibration I have need to establish the peak position; to do that I perform a
 1138 fit of the ToT histogram of each pixels. As fit functions I test both the solutions below:

$$f(x, N, \mu, \sigma) = \frac{N}{\sigma\sqrt{2\pi}} e^{-\frac{1}{2}\left(\frac{(x-\mu)}{\sigma}\right)^2} \quad (6.7)$$

$$f(x, m, q, N, \mu, \sigma) = m x + q + \frac{N}{\sigma\sqrt{2\pi}} e^{-\frac{1}{2}\left(\frac{(x-\mu)}{\sigma}\right)^2} \quad (6.8)$$

Nel primo caso ho fissato pochi pixel attorno a picco: il range è stato determinato ..

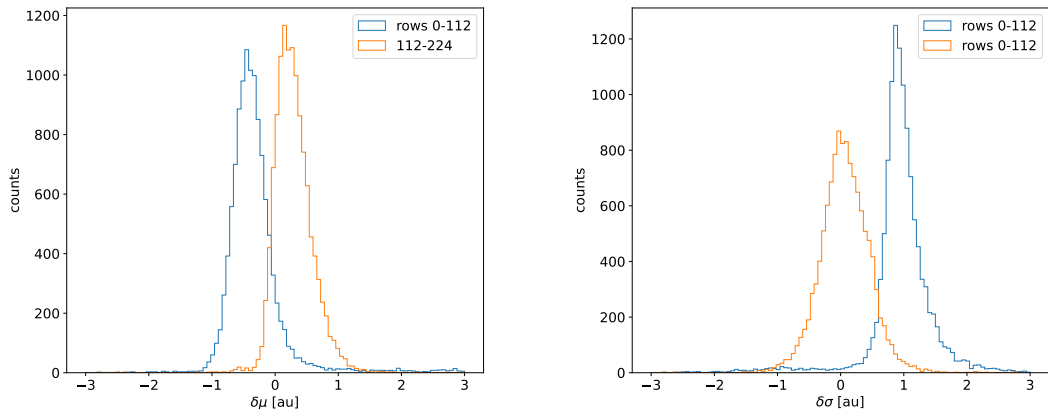


Figure 6.7: Here there are shown the defference between the parameters μ and σ fitted with only a gaussian and with a gaussia plus a line. When $\mu < 0$ the fit function 6.7 has given a worst peak (shifted on the left); when $\sigma < 0$, 6.8 has given a worst peak width (larger sigma)

1139
 1140 **controlla. Nel secondo caso invece il range è.. Controlla sullo script** Even if the difference
 1141 in the peak position between the two cases is not really relevant (6.7) being of the order
 1142 of 0.8-1.5 %, it still introduces a systematic effect moving the peak on the left beacuse of
 1143 the contribution of the tail. Indeed, we know that the sharp edge on the right corresponds
 1144 to the complete absorption of the photon, so excluding the little bump on the right, the
 1145 more the fitted parameter is on the right, the better the fit is. Moreover, there is also
 1146 systematic effect on the peak width, infact the worst fit also gives an overestimation of

1147 the peak width. Even looking at the χ^2 , the fit function 6.7 seems so be the better choise,
1148 except for a sample of pixels on the lower part of the matrix, the one with lower efficiency.

1149 Mappa del ferro da cui, come descritto enll'equazione si ricava la capacity. La struttura
1150 a bande della capacità ha origine nel plot... e quindi nella calibrazione. Andando a vedere
1151 gli istogrammi di queste due variabili si vedono dei picchi. C'è qualche struttura nella
1152 matrice che condiziona il funzionamento delle righe? Larghezza della gaussiana: fai il
1153 discorso a cosa contribuisce ad un picco così largo. è compatibile con quanto ti aspetti?
1154 The voltage fluctuation around the peak is caused by the number fluctuation of generated
1155 carriers (Fano noise) and the noise introduced by the detector (sensor and front-end pre-
1156 amplifier).The ENC can be estimated from the standard deviation of the Kalpha voltage
1157 distribution. $ENC = \sqrt{\sigma_{FE}}$ (sigma misurata- quella che ti aspetti dal fattore di Fano). E
1158 è compatibile con quanto trovato? se non fosse compatibile rimaneggia questa frase:
is added from the system (test setup) at the analog monitoring pixel output.

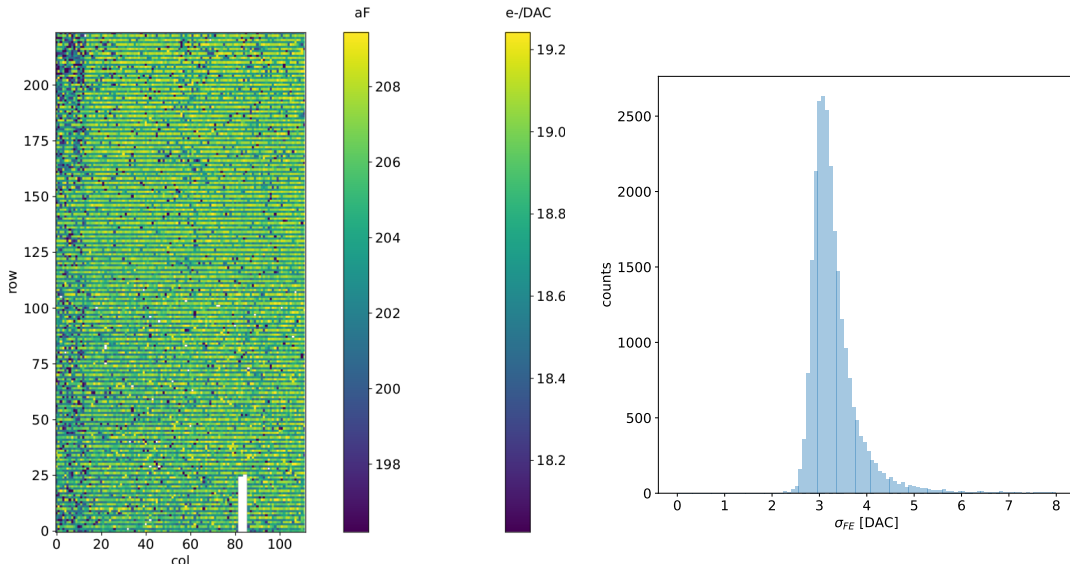


Figure 6.8

1159

1160 6.1.4 Changing the bias

1161 In order to study the behavior of the sensor changing the bias, I perform some injection
1162 scans in different configurations. The thickness of the depletion has to be considered
1163 indeed an important parameters for the efficiency of the signal, and in particular it affects
1164 the charge released by a particle which cross the sensor (since the signal is proportional to
1165 the thickness of the epitaxial layer). Given that the chip under examination has a gap in
1166 the low dose epi-layer (look at chapter 4.1) we were not able to change independently the
1167 bias of the substrate (PSUB) and of the p-well (PWELL), but they must be kept at the
1168 same value, differently from other chips, where on which some test has been performed, as
1169 reported in figure 6.9. A 2D map of the measured output voltage amplitude and resulting
1170 gain in the case of the PMOS and HV are reported.

1171 In order to test the behavior of the chip when not completely depleted, I have performed
1172 an injection scan with PSUB/PWELL bias at 0 V, -3 V and -6 V, and some acquisitions
1173 with the Fe55 source. The results of the measurements are reported in table 6.3 and in
1174 figure ???. Turning down the bias, the depletion region narrows and the efficiency reduces,

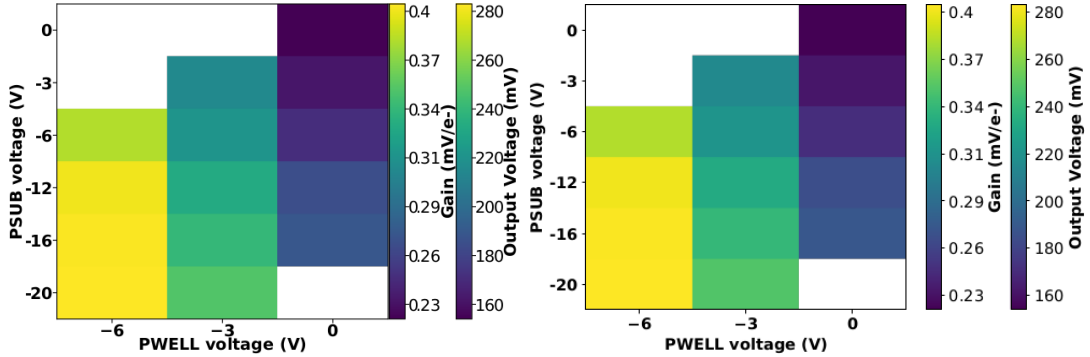


Figure 6.9: 2D map of the output voltage amplitude and gain with respect to the p-well and p-substrate in the case of the PMOS reset front-end (B)

	-6 V	-3 V	0 V
Threshold [DAC]	20.04 ± 1.6	21.0 ± 1.6	24.5 ± 1.8
Noise [DAC]	0.613 ± 0.075	0.625 ± 0.078	0.822 ± 0.098
Slope [au/DAC]	0.726 ± 0.027	0.707 ± 0.028	0.573 ± 0.021
Offset [au]	-10.8 ± 1.9	-11.2 ± 1.8	-11.1 ± 1.5

Table 6.3: The errors are the standard deviations of the corresponding distributions. The conversion factor from DAC to electrons is $\sim 20 \text{ e}^-/\text{DAC}$.

in particular in the pixel corner; in particular the threshold increases of $\sim 1/4$, the noise of $\sim 1/3$ and the slope, which parameterizes the linearity of the analog output and strictly depends on the gain, decreases of $\sim 1/4$. In figure 6.10(b) are reported the values of the K_α peak position, the normalization of the events above the peak and the rate, everything has been normalized to the value at the reference condition, which is with PSUB/PWELL at -6 V. In order to evaluate the peak position and the normalization I have fit the spectrum in the region on the right with a gaussian. Looking at the spectrum, an other characteristics seems to appear: at lower bias the peak width is bigger than in a full depletion mode. This could be due at a bigger capacity, which influence the noise.

6.1.5 Measurements with radioactive sources

In order to completely validate the operation of the whole sensor¹, I have made some acquisitions with radioactive source, in particular I have used Fe55, Sr90, which is a β^- emittitor with electron endpoint at 0.546 MeV, and cosmic rays, which are supposed to be mostly MIP. In the acquisitions with Sr90 and cosmic rays, I specifically focused on the events with charge sharing and with more hits than one per events, that are clusters.

The definition of cluster I chose is built only on the time of arrival of hit, in particular I established that all particles with the same timestamp belong to the same cluster. This obviously is a coarse requirement but it gave me the opportunity of using a simple and fast clustering algorithm, which is fine when the random coincidence probability is negligible. Defining R_1 and R_2 as the two events rate, and τ as the dead time of the detector, the

¹As I will explained in chapter ?? these measurements are fundamental also to be compared with the spectrum seen at the testbeam

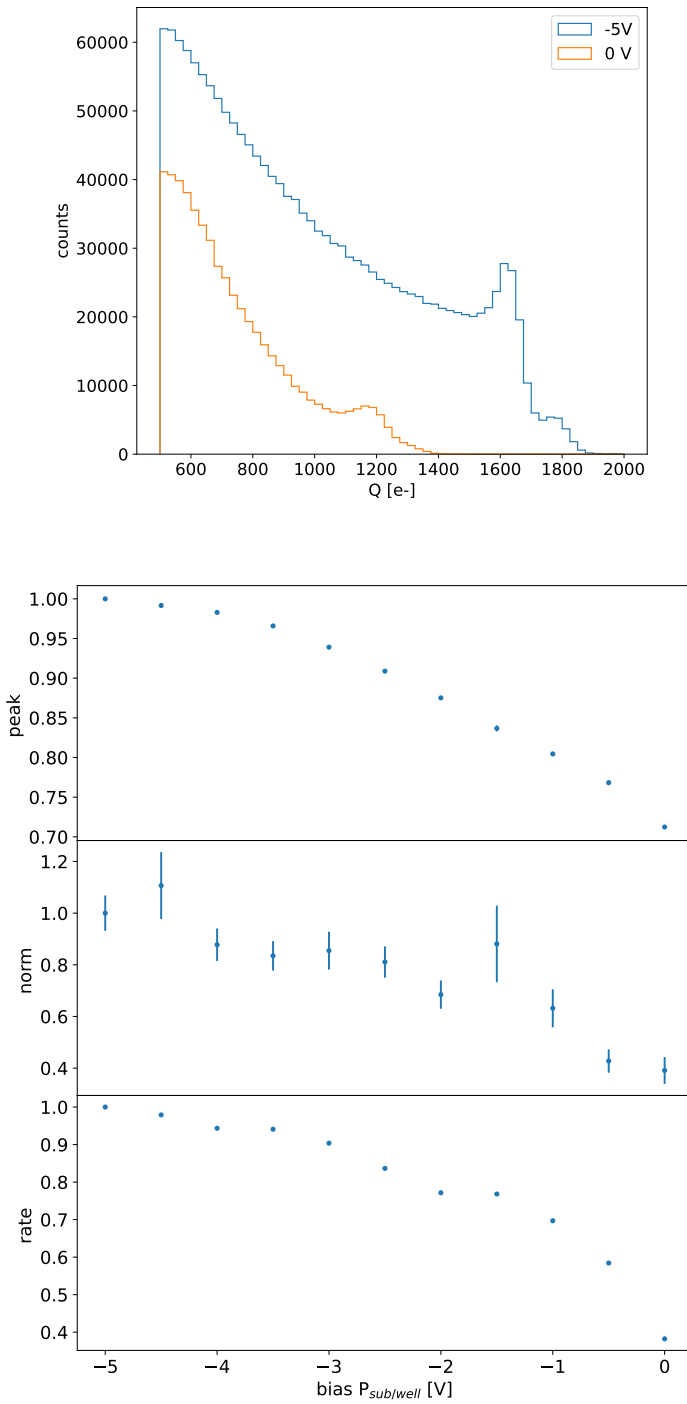


Figure 6.10: Two acquisition with the Fe55 source at different bias.

random coincidence rate can be found:

$$R_{coinc} = R_1 \times R_2 \times \tau \quad (6.9)$$

As I am going to prove in the next section, the dead time strictly depends on the occupancy of the matrix, even though we can assume a dead time of $\sim 1 \mu\text{m}$, which corresponds to the mean dead time per pixel. However, if in an event a particle hit two different pixels producing a cluster, the total dead time simply doubles. Then, assuming a rate of noise

1200 of \sim Hz on the whole matrix and being the mean rate of the , the random coincidence of
 1201 two hits coming from Fe-noise, Sr-noise, CR-noise and noise-noise are respectively

1202 In figure ?? I report the histograms of the number of pixels in the cluster and of the
 1203 dimension of clusters, defined in terms of the max and min coordinates on the matrix as:

$$d = \sqrt{(y_{max} - y_{min})^2 + (x_{max} - x_{min})^2} \quad (6.10)$$

1204 quello che si nota è che lo Sr fa cluster più grandi mediamente, che arrivano anche a 22
 1205 hit.

1206 Below I have also attached a sample of hitmap of events produced by the three different
 1207 sources.

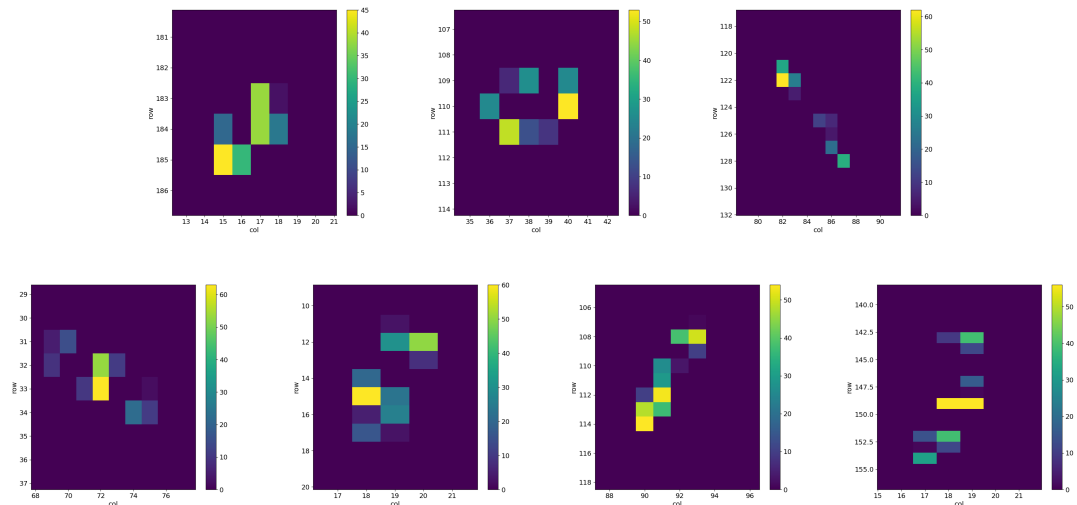


Figure 6.11

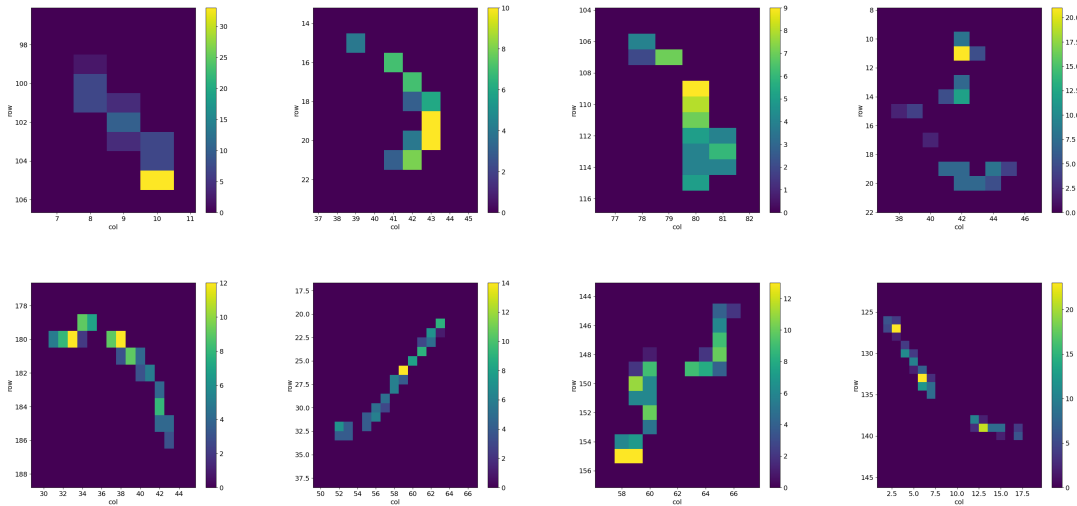


Figure 6.12

- 1208 • PLOT delle hit per cluster
 1209 • esempio di hitmap di cluster

1210 • sostituisci in carica in un file del ferro, guarda somma dei cluster, stessa cosa per Sr
1211 e MIP

1212 • Spiega che con il flavor HV abbiamo una perdita di segnale, fai vedere uno spettro
1213 di delle misure dell'8 marzo.

1214 The signal generated by electrons is similar to the one generated by minimum ionizing
1215 particle (MIPS) **dovrei mettere qualche conto per giustificare questa affermazione**, and the
1216 spectrum is expected to follow a Langau-Gauss distribution. **nelle acquisizioni dei CR ho**
1217 **selezionato solo i cluster, per tagliare via il rumore.**
1218 , looking at the cluster dimension and the cluster charge.

1219 6.1.6 Dead time measurements

1220 The hit loss is due to analog and digital pile up: the first one occurs when a new hit
1221 arrives during the pre-amplifier response, the second instead when the hit arrives while
1222 the information of the previous hit has not yet been transferred to the periphery. Since
1223 the pre-amplifier response has a characteristic time \sim ToT, the dead time τ_a introduced by
1224 it will be at most 1.6 μ s; using the IRESET and VRESET FE parameters the reset time
1225 can be lowered down, but a **IRESET, puoi diminuire il tempo di scarica.** Regarding the
1226 latter contribution instead, since only one hit at a time can be stored on the pixel's RAM,
1227 until the data have completed the path to get out, the pixel is paralyzed. Moreover since
1228 there is no storage memory included on TJ-Monopix1 prototypes, the digital dead time
1229 τ_d almost corresponds to the time needed to transmit the data-packets off-chip.

1230 The exportation of data from pixel to the EoC occurs via a 21-bits data bus, therefore
1231 only one clock cycle is needed and the dead time bottleneck is rather given by the
1232 bandwidth of the serializer which transmits data off-chip from the EoC. In our setup the
1233 serializer operates at 40 MHz, thus to transmit a data packet (27-bit considering the ad-
1234 dition of 6 bits to identify the double-column at the EoC) at least 675 ns are needed. For
1235 what we have said so far, the R/O is completely sequential and therefore is expected a
1236 linear dependence of the reading time on the number of pixels to read:

$$\tau = 25 \text{ ns} \times (\alpha N + \beta) \quad (6.11)$$

1237 where α and β are parameters dependent on the readout chain setting.

1238 To test the linearity of the reading time with the number of pixels firing and to measure
1239 it, I have used the injection circuit which allows me choosing a specific hit rate: I made
1240 a scan injecting a fix number of pulses and each time changing the number of pixels
1241 injected. Indeed the injection mode allows fixing not only the amplitude of the pulse,
1242 which corresponds to the charge in DAC units, but also the time between two consecutive
1243 pulses (DELAY) and the width (WIDTH). The hit rate then corresponds to :

$$R = \frac{25 \text{ ns}}{(DELAY + WIDTH)} \quad (6.12)$$

1244 where WIDTH is equal to 60 counts.

1245 Unfortunately a high random hit rate on the matrix cannot be simulated by the in-
1246 jection because of the long time (\sim ms) needed to set the pixel registers of the injection;
1247 then I was forced to specify at the start of the acquisition the pixels to inject on, and for
1248 convenience I chose those on a same column. In figure 6.13 is shown the dependence of

Parameter	Value [DAC]	Value [μs]
START_FREEZE	64	1.6
STOP_FREEZE	100	2.5
START_READ	66	1.65
STOP_READ	68	1.7

Table 6.4: Default configuration of the R/O parameters

1249 the efficiency on the DELAY parameter in two different cases. For the 5 pixels example
 1250 the efficiency goes down the 90% at a DELAY of ~ 185 clock counts, which corresponds
 1251 to $6.125 \mu\text{s}$ and to a rate of 160 kHz , while in the 10 pixels example, the efficiency goes
 1252 under the 100% at ~ 380 clock counts, which corresponds to $11 \mu\text{s}$ and to a rate of 90 kHz .
COME MAI SONO DIVERSE LE CURVE? From the efficiency curves I have then looked

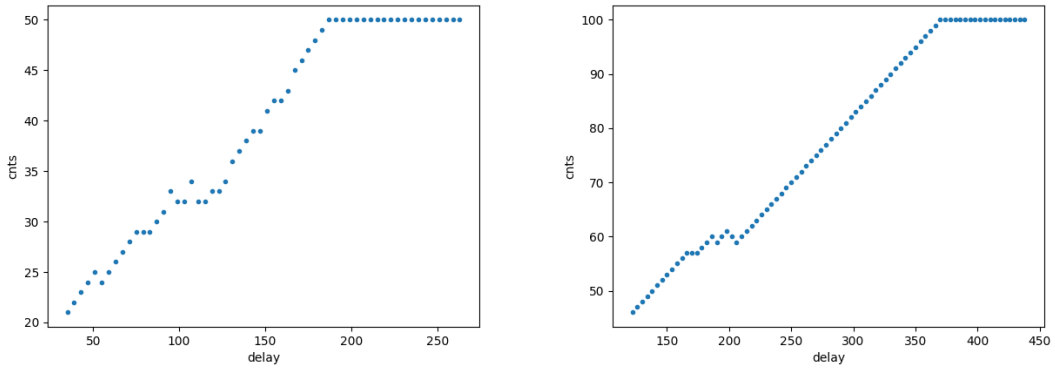


Figure 6.13: Efficiency vs the DELAY parameters. (a) I made a scan injecting 5 pixels with 50 pulses for each DELAY configuration and (b) 10 pixels with 100 pulses for each DELAY

1253 for the time when the efficiency decreases. In figure 6.14(a) is shown the dead time per
 1254 pixels as a function of N with different R/O parameters configuration, the meaning of
 1255 which is explained in chapter 4.3. The default value suggested by the designer of the chip
 1256 are reported in table 6.4; moving too much the readout parameters from the default ones,
 1257 the readout does not work properly, and no hits can be read at all. The problem probably
 1258 stays in the firmware setting of the readout which are specially fixed for our chip **Sul**
 1259 **repository, nei commenti ci sono altri valori possibili per il FREEZE, ma avevamo detto**
 1260 **che probabilmente sono relativi ai setting di altri chip.** Despite the single pixel reading
 1261 time does not depend on the position on the pixel matrix, whithin a clock count which
 1262 is $\sim 25 \text{ ns}$, and it is equal to 106 clock counts, since the τ_d critically depends on the pixel
 1263 position on the matrix: in particular the reading sequence goes from row 224 to row 0,
 1264 and from column 0 to column 112, making the pixel on the bottom right corner the one
 1265 with the longest dead time.

1266 Furthermore to test that there is no dependece of the digital readout time from the
 1267 charge of the pulse, I have try to change the amplitude of the pulse injected, but the
 1268 parameters found were consistent with the default configuration ones. No difference in the
 1269 α and β coefficients has been observed between the two case. **In realtà non mi torna perché**

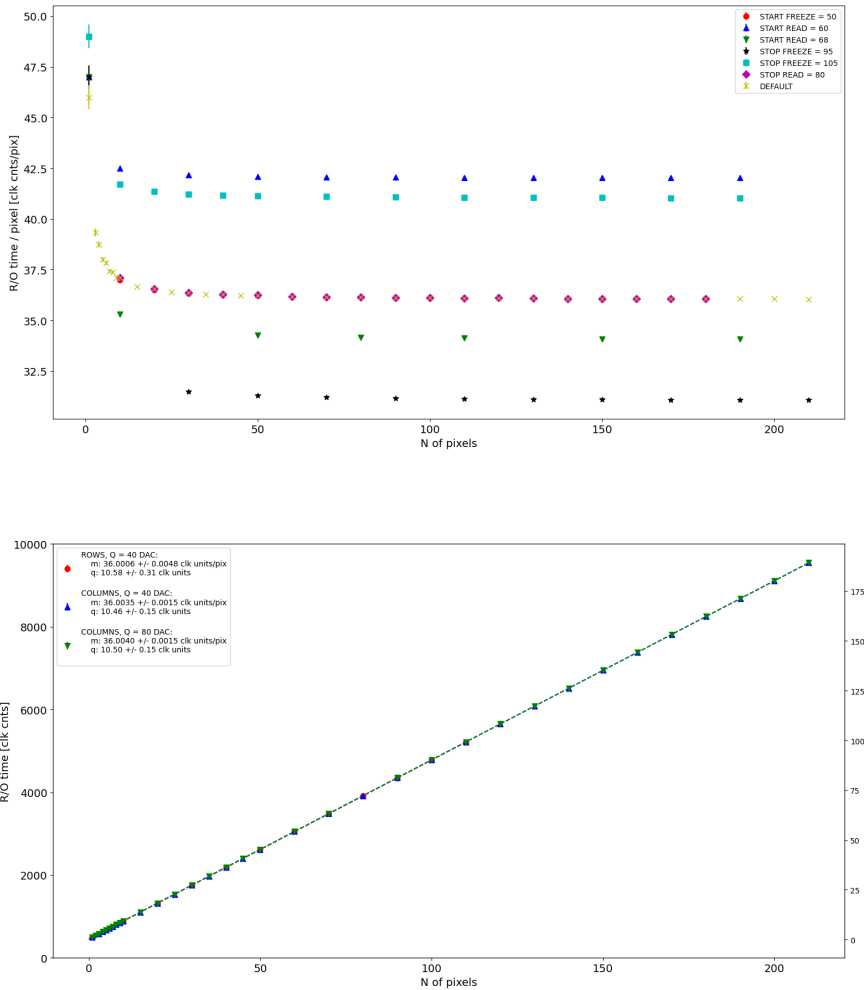


Figure 6.14: (a) Readout time per pixel as a function of the number of pixel injected obtained with different FE setup. (b) Readout time as a function of the number of pixels injected obtained injecting pulses with amplitude of 80 DAC (green), of 40 DAC on the same row (red) and on the same column (blue).

1271 il FREEZE dovrebbe iniziare n cicli di clock dopo il TE, ed il TE dipende ovviamente dal
 1272 ToT, quindi mi sarei aspettata una differenza tra i due. Referring to eq.6.11, the factor
 1273 α is proportional to the difference (STOP_FREEZE - START_READ), while the offset β
 1274 lies between 5 and 15 clock counts.

1275 Per avere una misura veritiera del tempo morto e del hit loss si dovrebbe iniettare
 1276 casualmente input events are produced by a random hit generator with a specified hit
 1277 rate, hence following a Poisson distribution. Inoltre faccio notare che il tempo morto
 1278 è così lungo perchè c'è parallelizzazione e neppure un buffer (cosa tipicamente prevista
 1279 quando li si inserisce nei rivaltori). Ad esempio Obelix, per l'upgrade di Belle2 avrà un
 1280 buffer a fine matrice.

1281 6.2 ARCADIA-MD1 characterization

1282 Unfortunatly we have found out that the chip we received was not completely functional,
1283 then we have been able to make on it only a few electrical and software test. We have
1284 then verified the comunicacion of the chip with the DAQ, testing the operations of the
1285 FPGA and the breackout board (BB). The problem occurs when the chip is biased, in
1286 particular, when the HV voltage is lowered down 0 V, the sensor requires too much power
1287 and a too high current draw sets. We have discussed the problem with the designers of
1288 the chip whose helped us indentifying the motivation of the break: the chip has been
1289 glued using too much conductive tape and hence have a short-circuit between the sides
1290 and the back, which makes impossible the biasing. Unfortunately, since both the sensor
1291 and the FE require at least -10 V to work properly, no measurement was possible except
the acquisition of the noise in the FE circuit.

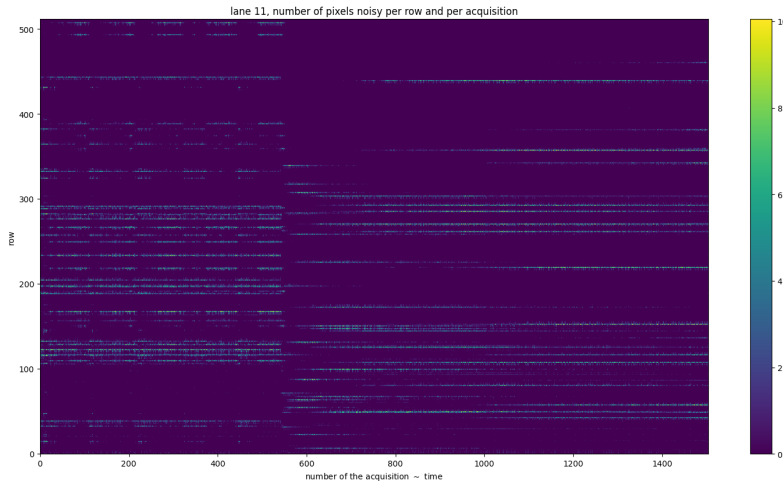


Figure 6.15: Noise in the front end circuit depending on the bias road across the matrix was recorded.

1292
1293 We received then another chip, a minid2, that is a "mini demonstrator" from the
1294 second submission. The two chips have the same charateristics but the minid2 is smaller
1295 than the MD1, in particular it only have 32×512 pixels, instead of 512×512 . **scrivi il
1296 problema della prima sottomissione.**

1297 An exhaustive characterization and testing of the new chip have been going on in the
1298 clean room on the INFN, and I am going to show here only some preliminary results. Up
1299 to now we used the injection circuit in order to make a threshold scan on a few pixels:
1300 differently from the TJ-Monopix1's charaterization where we performed a scan changing
1301 the injection charge of the pulse, with the minid2 we have instead changed the threshold
1302 (whose register is VCASN) keeping the charge of the pulse fixed. For each threshold we
1303 inject 100 pulses of amplitude $10 \mu\text{s}$. The dependece of the efficiency on the threshold for
1304 two pixels is shown in figure 6.16.

1305 **Anche se il comportamento è globalmente ragionevole, con l'efficienza che sale quando
1306 si abbassa la soglia, viene il sospetto che non stiamo polarizzando bene il sensore e il
1307 FE dato che anche raggiunto i centi conteggi, si hanno delle fluttuazioni intorno a questo
1308 valore. Inoltre notiamo che abbassando ulteriormente la soglia si osserva un aumento delle**

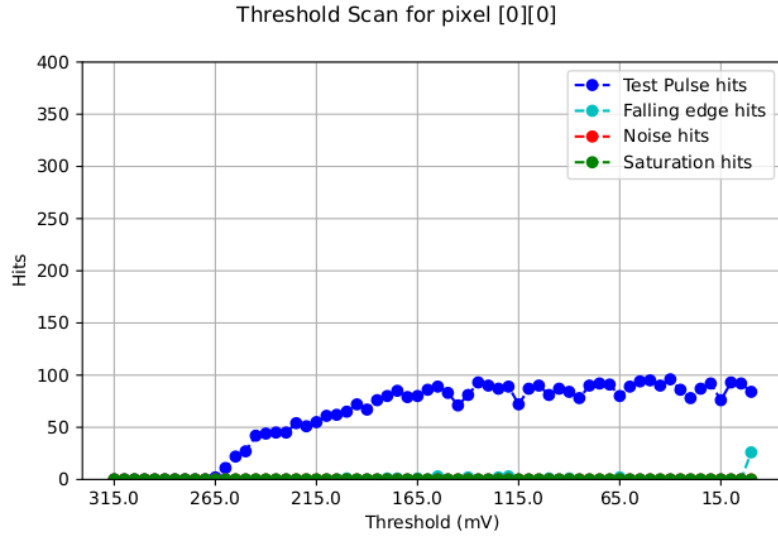


Figure 6.16

1309 hit, dovuto al fatto che si inizia a triggerare sul rumore.

1310 commenta sul fatto che non è stabile anche molto sopra la soglia. Forse è dovuto al
 1311 bias? oppure l'impulso ha qualche problema (non abbiamo settato la durata ecc..)? Che
 1312 valore ha in elettroni?

1313 Substantial differences have been observed in both the efficiency and the threshold
 1314 among the sections, with VCASN=40 DAC; this suggests that with this particular FE
 1315 configuration there is a big threshold dispersion on the matrix. The hitmap of an ac-
 1316 quisition with the Fe55 source is shown in figure 6.17: the whole MD1 matrix with only
 1317 the bottom region (32 rows) working is represented in (a), while in (b) there is a zoomed
 1318 hitmap. The rate seen within the region 8 (green region in the figure (a)) is compatible
 1319 with the rate of the same radioactive source measured with TJ-Monopix1, that it ~ 3.3 kHz.
 1320 Looking to the Sr90 acquisitions (fig.6.18) many clusters and tracks can be immidiately
 1321 distiguished, confirming what observed with TJ-Monopix1.

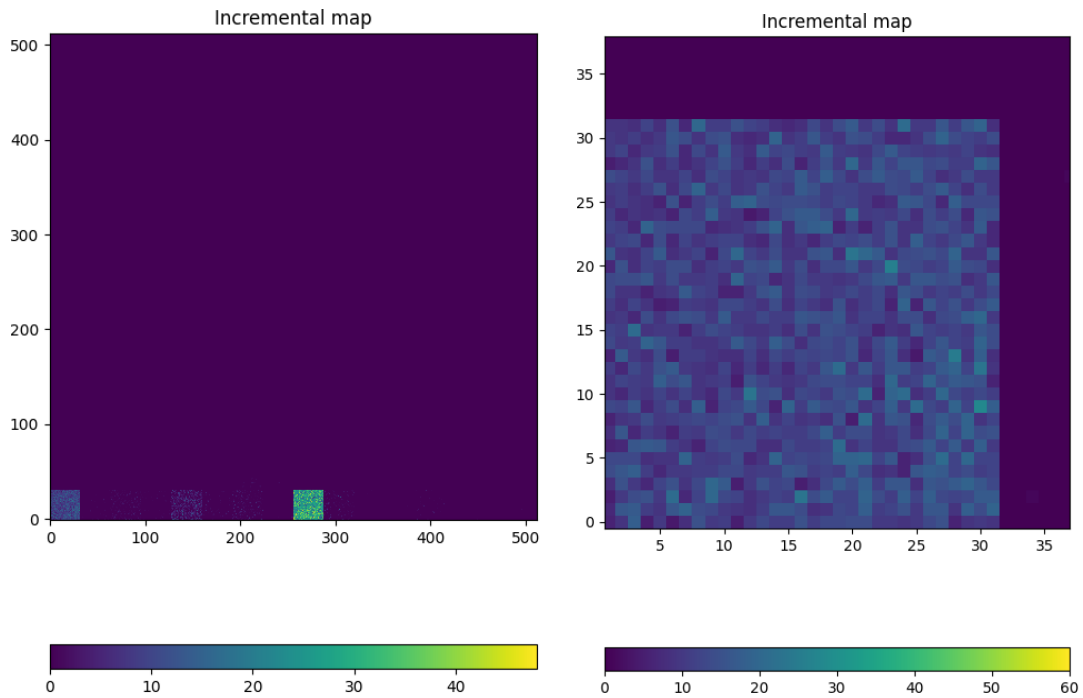


Figure 6.17: Fe55 acquisition with VCASN=40 DAC. (a) All the matrix 512×512 is plotted even if the minid2 has only the rows in range 0-32. (b) A zoom on the first section (col 0-32).

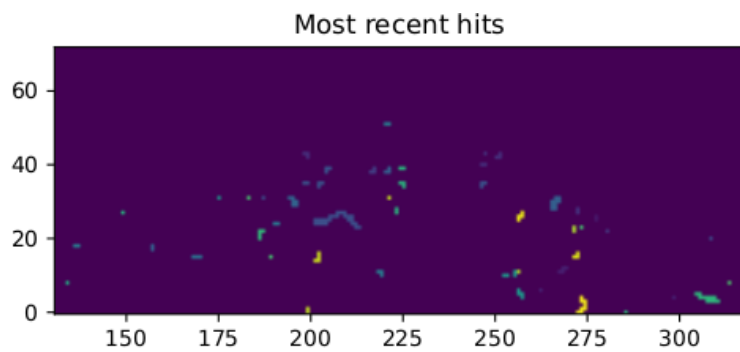


Figure 6.18: Sr90 acquisition with VCASN=40 DAC. The different colours are related with the time of arrival of the hits: in yellow the most recent hits, while in blue the old ones.

₁₃₂₂ **Chapter 7**

₁₃₂₃ **Test beam measurements**

₁₃₂₄ At PRF smaller than 100 Hz, all the dosimeters analyzed have a shorter signal collection
₁₃₂₅ time with respect to the repetition time of the pulses (maggiore uguale 10 ms), and,
₁₃₂₆ consequently, the saturation is influenced only by the dose-per-pulse (duration of the
₁₃₂₇ pulse is around 2.5 us)

₁₃₂₈ During August 2022 a testbeam took place in Santa Chiara hospital in Pisa, where a
₁₃₂₉ new accelerator designed for both medical research and R&D in FLASH-RT, and for this
₁₃₃₀ reason called "ElectronFlash", have been installed a few months ago.

₁₃₃₁ The motivation of the testbeam measurements were testing TJ-Mopopix1 in condition
₁₃₃₂ different from the one foreseen during the design and also testing the mechanical and the
₁₃₃₃ DAQ setup for other future measurement. TJ-Monopix1 is supposed to be employed for
₁₃₃₄ tracking in HEP experiments while our goal was testing the possibility of integrating the
₁₃₃₅ charge released by more particles at ultra high hit rate achievable with the accelerator.
₁₃₃₆ **Una frase di disclaimer sul fatto che non siamo riusciti a testare quello che volevamo.**

₁₃₃₇ In medical physics the dose is indeed the standard parameter to characterize the beam
₁₃₃₈ because of its obvious relation with the damage caused in the patient: firstly the oncolo-
₁₃₃₉ gists prescribe a certain dose taking into account the efficacy of the treatment and then
₁₃₄₀ the medical physicists, on the basis of simulations, decide the energy and the intensity of
₁₃₄₁ the beams to dispense the prescribed dose amount. By the point of view of the instrumen-
₁₃₄₂ tation and the testing on it, a more common and useful parameter is instead the rate or
₁₃₄₃ the fluence of particles. The conversion between the two quantity can be found thinking to
₁₃₄₄ the definition of dose: it is the concentration of energy deposited in tissue as a result of an
₁₃₄₅ exposure to ionizing radiation. Assuming total absorption of electrons in water, defined
₁₃₄₆ by law as the ordinary reference medium, the dose can be expressed as:

$$D[Gy] = \frac{NE[eV]}{\rho[g/cm^3]A[cm^2]x[cm]} \quad (7.1)$$

₁₃₄₇ After having applied the conversion of the energy from eV to J and noticed that $E/\rho x$
₁₃₄₈ roughly corresponds to the stopping power S of electrons in water, a simple estimation of
₁₃₄₉ the dose released in water is:

$$D[Gy] = 1.602 \cdot 10^{-10} N[cm^{-2}] S[MeV cm^2/g] \quad (7.2)$$

₁₃₅₀ **7.1 Apparatus description**

₁₃₅₁ The accelerator is placed in a bunker inside the hospital: to shield the outdoor from
₁₃₅₂ ionizing radiation the bunker has very thick walls of cementum and both the control units

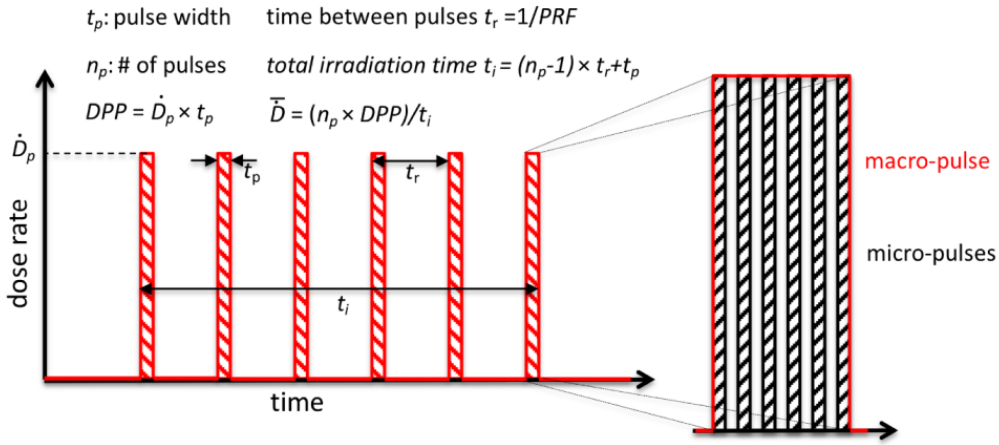


Figure 7.1: Typical beam structure of a beam with the standard characteristic quantity

\bar{D}	Dose rate (mean dose rate for a multi-pulse delivery)	0.005-10000 Gy/s
\dot{D}	Intra pulse dose rate (dose rate in a single pulse)	0.01-1 10^6 Gy/s
DDP	Dose in a single pulse	0.04-40 Gy
PRF	Pulse repetition frequency (number of pulses delivered per unit of time)	1-350 Hz
t_p	Pulse width	0.2-4 μ s
n	Number of pulses	single/pulse train

Table 7.1: The parameters that can actually be set by the control unit are the PRF, DDP, t_p and n (in particular singular irradiation or pulse train), while the other changes consequently.

1353 of the accelerator and of the detector were placed outside the bunker. For practicability
 1354 reasons the power supply were the only device to be placed inside the bunker.

1355 7.1.1 Accelerator

1356 The ElectronFlash accelerator is an electron Linear Accelerator (LINAC) with two energy
 1357 configurations, at 7 MeV and 9 MeV, and it can reach ultra high intensity (40 Gy/pulse)
 1358 keeping the possibility of accessing many different beam parameters and changing them
 1359 independently from each other. This characteristic is fundamental for research in FLASH-
 1360 RT, both for the medical aspects and for the studies on detectors; for example is not really
 1361 clear the dependence of the efficacy of the FLASH effect on the whole dose parameters.
 1362 ElectronFlash is **almost the only one** in the world having this characteristic, **ricontrolla sulla**
 1363 **review, c'era qualcosa che puoi dire.** The accelerator implements a standard beam struc-
 1364 **ture for RT with electrons (fig. 7.1), that is a macro pulse divided in many micropulses;**
 1365 the parameters used to set the dose and their range of values settable by the control unit
 1366 is reported in table 7.1.

1367 The accelerator is provided of a set of triod cannons \sim 1.2 m long and with diameters
 1368 from 1 cm to 12 cm and a collimator that can be used as beam shaper to produce a
 1369 squircle shape. The triode, which is made by plexiglass, must be fix to the gun during the
 1370 irradiation and is needed for producing an uniform dose profile (fig.7.2) which is desired
 1371 for medical purpose via the scattering of electrons with the plexiglass.

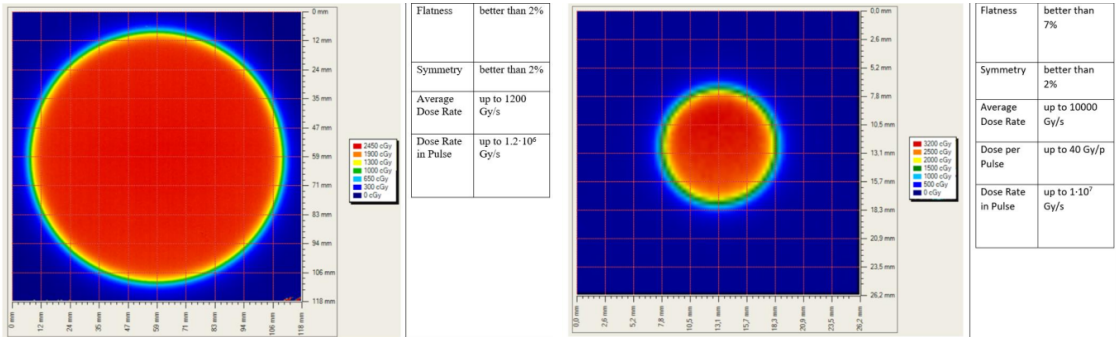


Figure 7.2: Two example of x-y isodose curves for two different triodes, 10 cm and 1 cm respectively, reported by the producer in the manual with the specific of the accelerator (S.I.T. - Sordina IORT Technologies S.p.A.). With the smaller collimator the dose rate in pulse is comparatively higher.

1372 7.1.2 Mechanical carriers

1373 The tested detector consists in one chip, the Device Under Test (DUT), mounted on a
 1374 board and connected to FPGA with same arrangement of figure 7.7. These have been
 1375 positioned vertically in front of the triode on a table specifically built for the testbeam.
 1376 The tree board have been enclosed in a box of alluminium with a window on the DUT
 1377 and with the required holes at the side to enable the biasing via cables and the connection
 1378 with the DAQ provided via ethernet cable. A trigger signal coming from the control unity
 1379 and syncronize with the pulses emitted from the beam has been also sent to the FPGA.
 1380 This signal cannot be considered a trigger signal, since being a prototypes TJ-Monopix1
 1381 has been designed to be triggerless, but the time of arrival of this signal, which is saved
 1382 by the FPGA, can allow the reconstruction of the of the arrival of the bunch during the
 1383 analysis.

1384 In order to shield the sensor from the whole particles emitted from the gun, two
 1385 alluminium collimators have been fabricated: one has been positioned at the triode exit
 1386 while the other in front of the DUT. The collimators are $t=32$ mm thick and have a
 1387 diameter d equal to 1 mm: assuming a beam divergence bigger than $d/t=1/32 = 1.8^\circ$,
 1388 which is the case, the collimator at the triode output was supposed to work as a point
 1389 source and to reduce the rate on the DUT of a factor at least $4 \cdot 10^{-4}$. The second one,
 1390 being near the DUT, was instead supposed to shield the sensor from the electrons which
 1391 have passed the first one, except for a region of 1 mm^2 configurable using **come si chiamano**
 1392 **quei cacciavitini per settare la posizione?**.

1393 7.2 Measurements

1394 Because of the dead time of TJ-Monopix1 it is not possible resolving the bunch sub-
 1395 structure and almost no one pixel can read more than a hit per bunch. I recall, indeed,
 1396 that the dead time per pixel depends on the location on the priority chain for the readout
 1397 and for each pixel $\lesssim 1 \mu\text{s}$ (fig. 7.7) are needed; therefore only a few pixels at the top of
 1398 the priority chain (at the upper left of the matrix) can fire a second time, since they in
 1399 principle can be read the first time before the end of the pulse (assuming a pulse duration
 1400 in $2 \mu\text{s}-4 \mu\text{s}$) and then can be hit again.

1401 Since resolving the single electron track is impossible, a way this sensor could be used

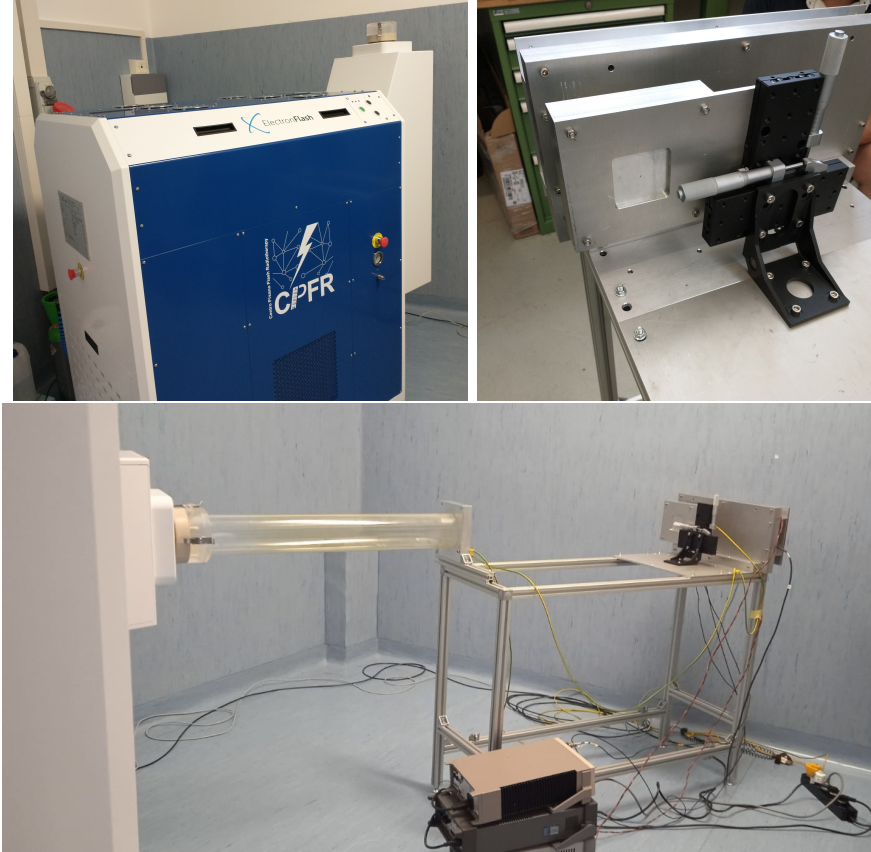


Figure 7.3: Experimental set up. (a) Electron flash accelerator: gantry rotante che consente un orientamento del fascio da 0° 90° (orizzontale / verticale) in tempo reale monitorato da un inclinometro integrato. the gun can be rotated from 90° to 0° (vertical/orizontal). (b) Collimator and DUT box. (c) Whole structure: we used the 10 cm diameter and 1.2 m long triode; the DUT which is in the box behind the two collimators is connected to the power supply units.

in such context is reducing its efficiency and taking advantage of the analog pile up and of the linearity of the analog output (ToT), in order to see a signal produced not by the single particle but by more electrons. Reducing the efficiency and the sensibility of the sensor is essential in order to decrease the high charge signal produced in the epitaxial layer: if the sensor is completely depleted the collection efficiency is closer to 1% and if the whole charges produced by a MIP, $80 \text{ e}^-/\mu\text{m}$ about, are collected, the saturation limit is soon reach. Then a condition where there is a partial recombination of the center electron-hole created in the bulk is desiderable. On the other hand, the smaller the output signal value and the higher the rate the detector can cope with: indeed, the rollover constitutes a limit for the usage of the analog output. With the standard configuration of the FE parameters and the epitaxial layer completely depleted, a MIP produces a ToT out of range of representation of 6-bit; so as to obtain smaller output signals one can operate on the reduction of the gain of the preamplifier or on the pulse velocity of returnig to the baseline. Recalling the results in section 6.1.4, I have shown that concerning the PMOS flavor 1, reducing the bias from -6 V to 0 V brings a reduction of efficiency down to 40 %, and a reduction in the gain of a factor $\sim 1/3$, while the reduction of the gain of the preamplifier allows a reduction of **circa 10, ma da controllare**.

1419 In order to taking advantage of the analog pile up and integrating the charge, for
 1420 semplicity assume of two electrons, the second one must hit the pixel before the ToT goes
 1421 under the threshold. The general condition is then $\overline{\Delta T} < \overline{ToT}$, but if a high $P_\mu(n \geq 1)$ is
 1422 required, a lower $\overline{\Delta T}$ may be desired:

$$P(n \geq 1) = \sum_{n=1}^{\infty} \frac{e^{-\mu} \mu^n}{n!} = 1 - P(0) = 1 - e^{-\mu} \quad (7.3)$$

1423

$$\mu = \frac{\overline{ToT}}{\overline{\Delta T}} \quad (7.4)$$

1424 If a $P_\mu(n \geq 1) = 99\%$ then the $\overline{\Delta T}$ must be $\sim 0.22 \overline{ToT}$. The ToT is in range [0,64] but
 1425 since the rollover must be avoided, the \overline{ToT} must be lower than 32, and then the minimum
 1426 rate on the pixel must be 1.25 MHz.

1427 During the testbeam many runs have been performed, spanning the energy, the dose
 1428 per pulse and the four possible configurations with/without the collimators. We have used
 1429 the PMOS flavor 1 in the standard configuration: we have biased the PWELL and PSUB
 1430 at -6 V and set the standard default FE parameters reported in table ???. During all the
 1431 acquisitions we have used pulses with t_p of 4 μm and with the smallest PRF settable, which
 1432 is 1 Hz, in order to start in the most conservative working point exluding the digital pile
 1433 up of events from different bunch: even if the whole matrix turns on and there are 25000
 1434 hits, the total readout time corresponding to 25 ms is still lower than the time between two
 1435 consecutive pulses. The readout starts with the trailing edge of the first pulse going down
 1436 the threshold, ~ 50 clk = 1.25 μs after this moment the FREEZE signal is sent to the whole
 1437 matrix, and the trasmittion of the data to the EoC begins. The hits read are the ones
 1438 whose TE occurred during the 50 clk counts; the ones, instead, whose TE occur during the
 1439 FREEZE are stored in the pixel memory and read during a second readout. Obviously
 1440 since the readout of the fist sub-pulse finishes much later than the bunch ends up, each
 1441 pixel can be store only one hit. An example of the two sub-pulses is shown in figure ???:
 1442 in the acquisition we injected 5 pulses with both the collimators mounted on the table.
 1443 Looking at the spectrum **si vede che lo spettro del secondo pulse ha una coda più lunga a
 1444 destra: questo è dovuto al fatto che le hit con tot lungo hanno il TE che cade durante il
 1445 FREEZE e quindi vengono lette durante il secondo impulso.** On the other hand the 2D
 1446 histograms, being uniform and not showing disomogenities, suggest that the collimators
 1447 do not shield all the particles: this was due to a photon background higher than expected.
 1448 When we have put aside the collimators, instead, the fluence was too high that **the whole
 1449 matrix turns on in 50 clk counts; then the 2 pulses substructure no more appears (fig. 7.6).**
 1450 **CONTROLLA PERCHÈ PORTEBBE ESSERE UNA CAZZATA**

1451 After the testbeam a simulation of the emission of electrons from the accelerator and
 1452 their path across the triode and the collimators has been developed via Geant-4 **come si
 1453 ringrazia il lavoro di qualcuno in maniera formale?**. The high background we saw although
 1454 the collimators were mainly produced by electrons Bremsstrahlung during the transition
 1455 through the alluminium collimators. **dalla simulazione si è visto che nessun elettrone
 1456 arriva sul chip quando ci sono montati i collimatori, mentre nel caso senza collimatori gli
 1457 eventi sono sostanzialmente tutti elettronni (frazione di fotoni prodotti in aria è?).** The
 1458 photons' simulated spectrum in the three configurations are shown in figure ???. **confronto
 1459 con quello che vedo nello spettro sopra: dati.**

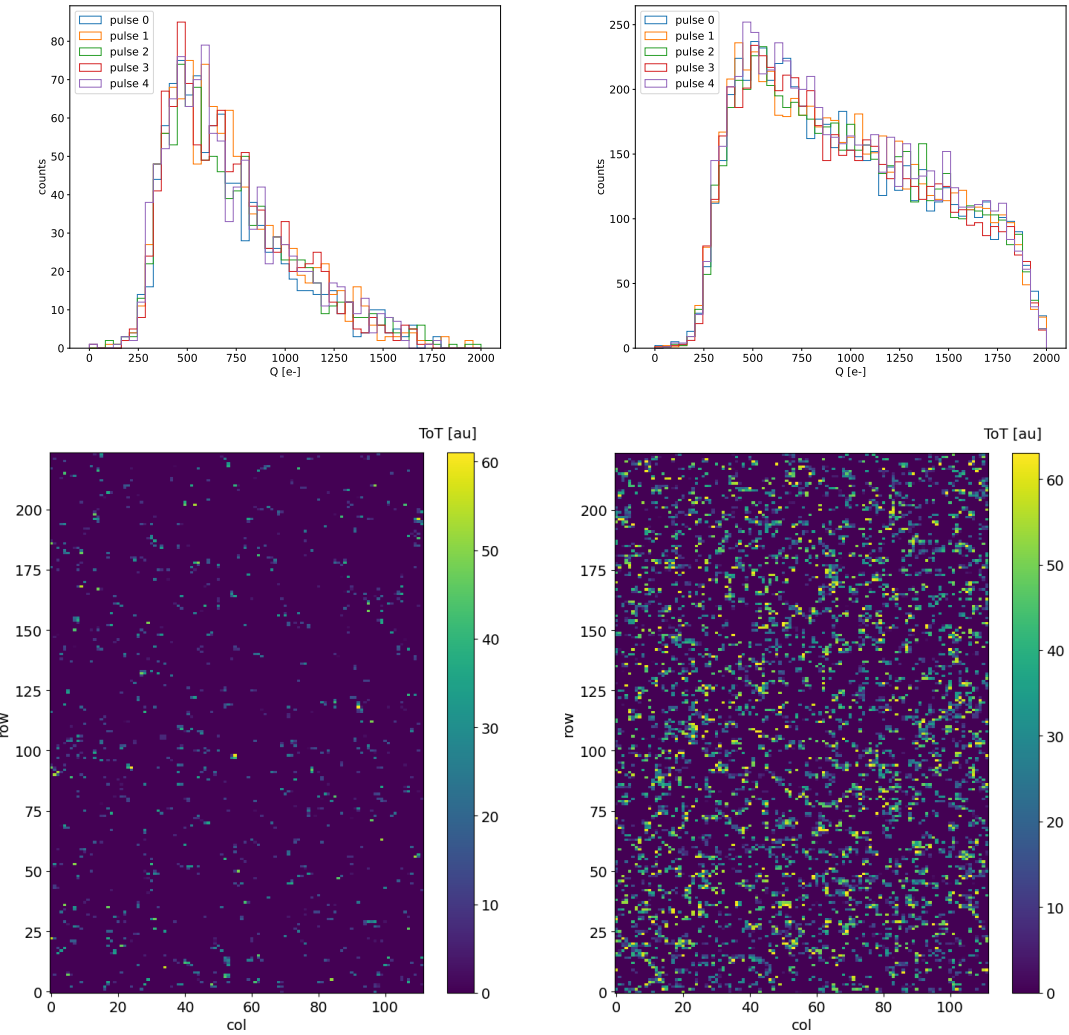


Figure 7.4: Acquisition with both the collimators: 5 pulses at DDP=0.07 Gy. (a) Spectrum of the charge released in the sensor: to apply the conversion I used the information found in the previous chapter. (b) 2D histogram of the ToT of the hits arrived in the sub-pulses.

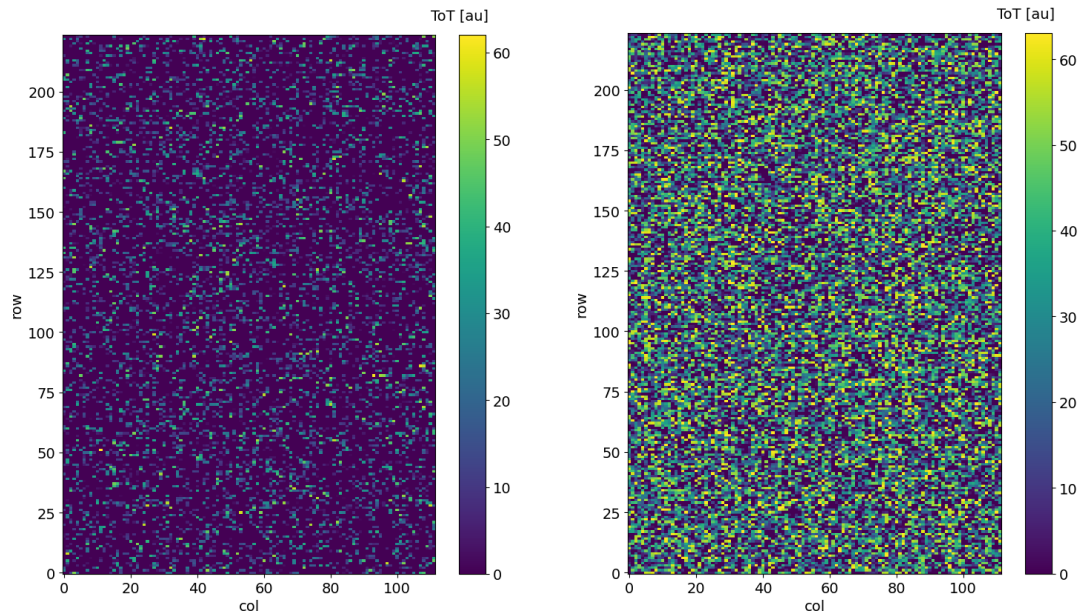


Figure 7.5: Acquisition with both the collimators: 5 pulses at DDP=0.6 Gy. 2D histogram of the ToT of the hits arrived in the sub-pulses. Compared with the previous maps, since the DDP is much higher, more pixels turn on.

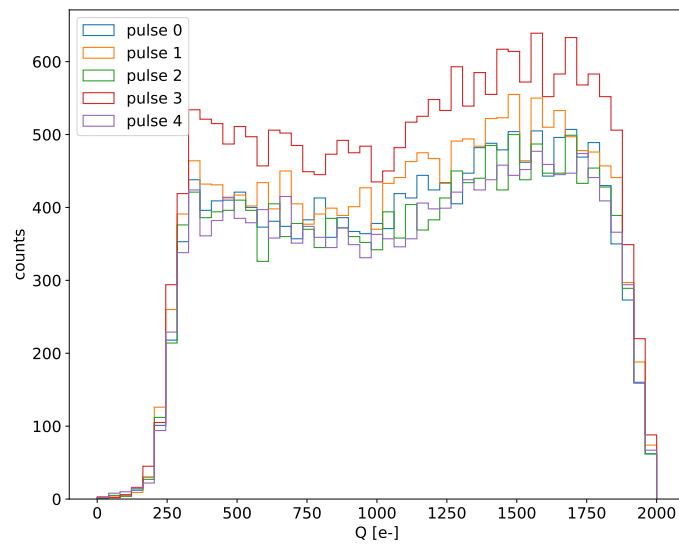


Figure 7.6: Acquisition without any collimator: 5 pulses at DDP=0.04 Gy.

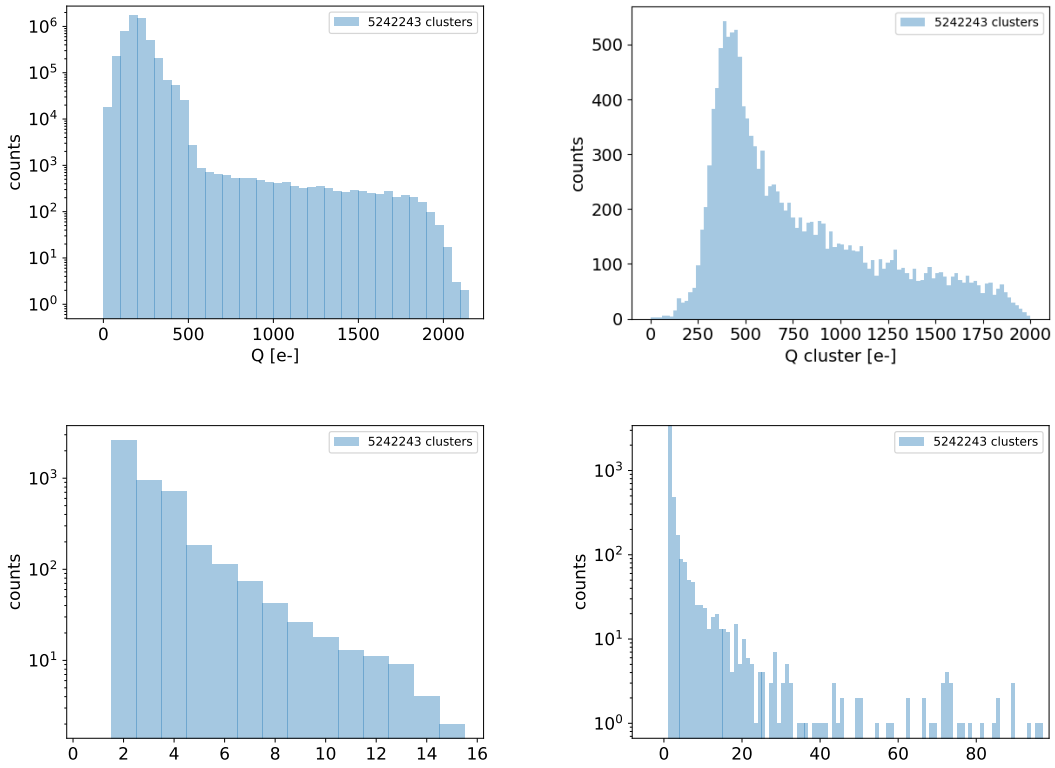


Figure 7.7: plot dei raggi cosmici da rigenerare

- 1461 • plot n di eventi che vedo con le diverse configurazioni
- 1462 • simulazione surya
- 1463 • confronta con misure dello spettro che vediamo senza e con collimatori.

1464 7.2.1 MIP spectrum using cosmic rays as source

1465 Since a MIP should produce about 2 ke- in the epitaxial layer, it should provide a signal
 1466 that in our conditions (full depletion and high gain) rolls over: in this situation making
 1467 prediction on the spectrum expected for MIPs becomes hard. Therefore, in order to
 1468 compare the spectrum observed at the testbeam with one certainly produced by MIP I
 1469 have made some acquisitions without any radioactive source, in order to look at the cosmic
 1470 ray events. To be confident with having selected MIPs from cosmic rays and cut the noise, I
 1471 have selected only the events with multiple hits: these events are mainly clusters produced
 1472 by the same impinging particle since the random coincidence probability is very low. In
 1473 fact the cosmic rays and noise rates on the whole matrix are respectively 0.02 Hz and
 1474 $\sim\text{Hz}$, the dead time in such a low occupancy condition can be always approximated with
 1475 $1\text{ }\mu\text{m}$ (this is not completely true for multiple hits events for which the priority chain
 1476 should be considered), the random coincidence rate is 10^{-8} Hz . Come mai lo spettro in
 1477 lab è diverso da quello visto con gli elettroni da 9 MeV al santa chiara? Chiedi a Surya il
 1478 rate visto sul detector senza collimatori.

1479 **Appendix A**

1480 **Pixels detector: a brief overview**

1481 **A.1 Radiation damages**

1482 Radiation hardness is a fundamental requirement for pixels detector especially in HEP
1483 since they are almost always installed near the interaction point where there is a high
1484 energy level of radiation. At LHC the ϕ_{eq} per year in the innermost pixel detector is
1485 $10^{14} n_{eq}/cm^2$; this number reduces by an order passing to the outer tracker layer [2] pag
1486 341 Wermes. Here the high fluence of particles can cause a damage both in the substrate
1487 of the detector and in the superficial electronics.

1488 The first one has a principal non ionizing nature, due to a non ionizing energy loss
1489 (NIEL), but it is related with the dislocation of the lattice caused by the collision with
1490 nuclei; by this fact the NIEL hypothesis states that the substrate damage is normalized to
1491 the damage caused by 1 MeV neutrons. Differently, surface damages are principally due
1492 to ionizing energy loss.

1493 **DUE PAROLE IN PIÙ SUL SURFACE DAMAGE** A charge accumulation in oxide
1494 (SiO_2) can cause the generation of parasitic current with an obvious increase of the 1/f
1495 noise. Surface damages are mostly less relevant than the previous one, since with the de-
1496velopment of microelectronics and with the miniaturization of components (in electronic
1497 industry 6-7 nm transistors are already used, while for MAPS the dimensions of compo-
1498nents is around 180 nm) the quantity of oxide in circuit is reduced.

1499 Let's spend instead two more other words on the more-relevant substrate damages:
1500 the general result of high radiation level is the creation of new energy levels within the
1501 silicon band gap and depending on their energy-location their effect can be different, as
1502 described in the Shockley-Read-Hall (SRH) statistical model. The three main consequence
1503 of radiation damages are the changing of the effect doping concentration, the leakage
1504 current and the increasing of trapping probability.

1505 **Changing of the effective doping concentration:** is associated with the cre-
1506ation/removal of donors and acceptors center which trap respectively electrons/holes from
1507 the conduction band and cause a change in effective space charge density. Even an in-
1508version (p-type becomes n-type¹) can happen: indeed it is quite common at not too high
1509 fluences ($\phi_{eq} 10^{12-13} n_{eq} cm^{-2}$). A changing in the doping concentration requires an adjust-
1510ment of the biasing of the sensor during its lifetime (eq.2.2) and sometimes can be difficult
1511 keeping to fully deplete the bulk.

1512 **Leakage current:** is associated with the generation-recombination centers. It has

1L'INVERSIONE OPPOSTA NON CE L'HAI PERCHÈ?

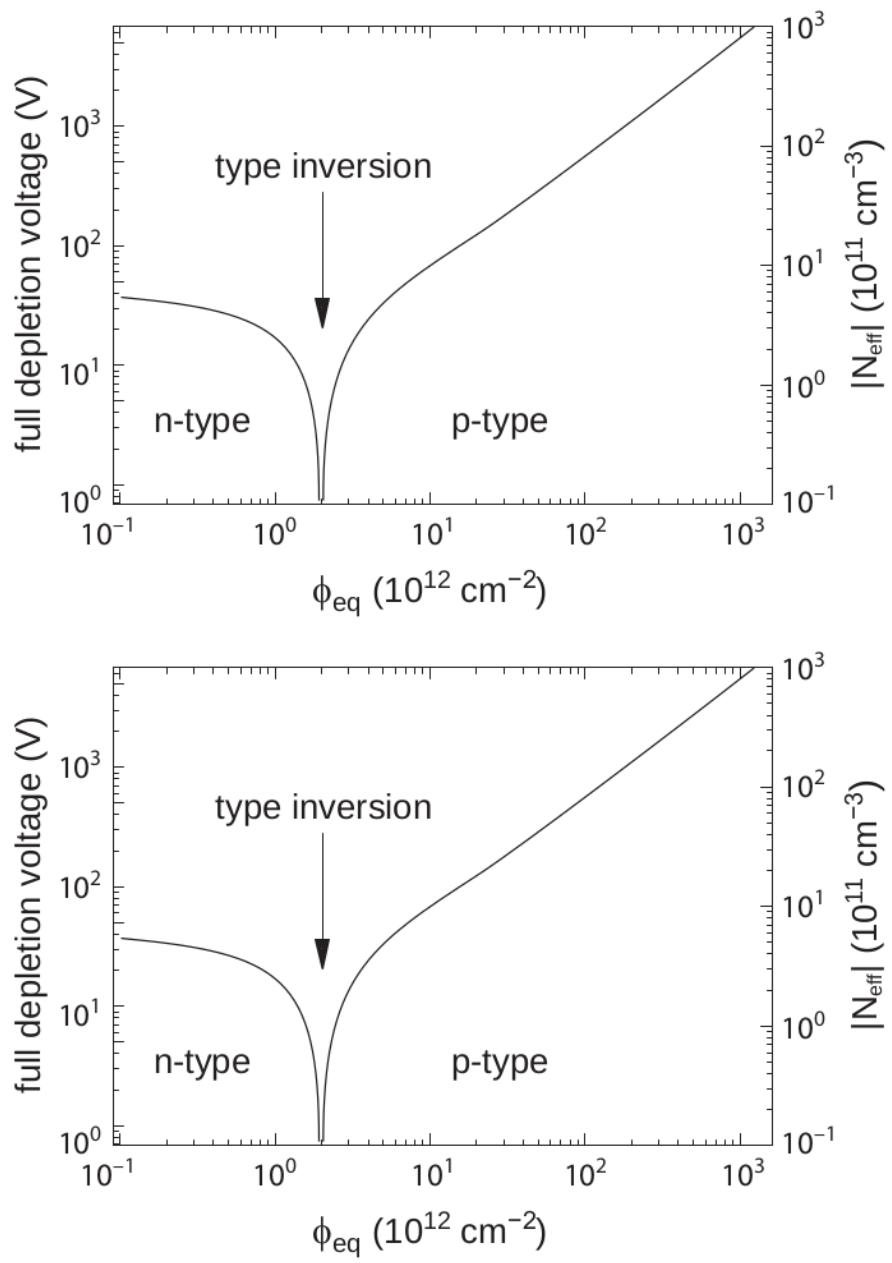


Figure A.1: 1b

1513 a strong dependence with the temperature ($I_{leak} \propto T^2$), whose solution is therefore to
1514 operate at lower temperature.

1515 **Increase of trapping probability:** since the trapping probability is constant in the
1516 depleted region, the collected charge decreases exponentially with the drift path. The
1517 exponential coefficient, that is the mean trapping path, decreases after irradiation and
1518 typical values are 125-250 μm and must be compared with the thickness of the depleted
1519 region which () corresponds to the mean drift path.

1520 Different choices for substrate resistivity, for junctions type and for detector design are
1521 typically made to fight radiation issues. Some material with high oxygen concentration
1522 (as crystal produced using Czochralki (Cz) or float-zone (Fz) process (**CONTROLLA**
1523 **LA DIFFERENZA TRA I DUE**)) for example, show a compensation effect for radiation
1524 damage; another example is the usage of n+ -in-p/n sensors (even if p+ -in-n sensors are
1525 easier and cheaper to obtain) to get advantage of inversion/to have not the inversion (since
1526 they are already p-type). After inversion the n+p boundary, coming from n+ in-n, but to
1527 keep using the sensor the depletion zone still must be placed near the diode.

1528 Single Event Upset, in sostanza è quando un bit ti cambia valore (da 0 a 1 o viceversa)
1529 perché una particella deposita carica nell'elettronica che fa da memoria registro/RAM/....
1530 Questo tipo di elettronica ha bisogno di un sacco di carica prima che il bit si "fippi"
1531 (cambi valore), infatti tipicamente per avere un SEU non basta una MIP che attraversa
1532 esattamente quel pezzo di chip in cui è implementata la memoria, ma un adrone che faccia
1533 interazione nucleare producendo più carica di quanto farebbe una MIP. Questo metodo pur
1534 essendo più comodo richiede less amount of area ha però come drawback che il registro può
1535 essere soggetto a SEU problema non trascurabile in acceleratori come HL-LHC adronici

1536

Bibliography

- 1537 [1] W. Snoeys et al. “A process modification for CMOS monolithic active pixel sensors
1538 for enhanced depletion, timing performance and radiation tolerance”. In: (2017).
1539 DOI: <https://doi.org/10.1016/j.nima.2017.07.046>.
- 1540 [2] H. Kolanoski and N. Wermes. *Particle Detectors: Fundamentals and Applications*.
1541 OXFORD University Press, 2020. ISBN: 9780198520115.
- 1542 [3] E. Mandelli. “Digital Column Readout Architecture for 10.1109/NSSMIC.2009.5402399
1543 the ATLAS Pixel 0.25 um Front End IC”. In: (2002).
- 1544 [4] M. Garcia-Sciveres and N. Wermes. “A review of advances in pixel detectors for
1545 experiments with high rate and radiation”. In: (2018). DOI: <https://doi.org/10.1088/1361-6633/aab064>.
- 1547 [5] C. Marinas. “The Belle-II DEPFET pixel detector: A step forward in vertexing in the
1548 superKEKB flavour factory”. In: (2011). DOI: [doi:10.1016/j.nima.2010.12.116](https://doi.org/10.1016/j.nima.2010.12.116).
- 1549 [6] J. Baudot. “First Test Results Of MIMOSA-26, A Fast CMOS Sensor With Inte-
1550 grated Zero Suppression And Digitized Output”. In: (2010). DOI: [doi:10.1109/NSSMIC.2009.5402399](https://doi.org/10.1109/NSSMIC.2009.5402399).
- 1552 [7] A. Dorokhov. “High resistivity CMOS pixel sensors and their application to the
1553 STAR PXL detector”. In: (2011). DOI: [doi:10.1016/j.nima.2010.12.112](https://doi.org/10.1016/j.nima.2010.12.112).
- 1554 [8] Giacomo Contin. “The STAR MAPS-based PiXeL detector”. In: (2018). DOI: <https://doi.org/10.1016/j.nima.2018.03.003>.
- 1556 [9] Nolan Espplen. “Physics and biology of ultrahigh dose-rate (FLASH) radiotherapy:
1557 a topical review”. In: (2020). DOI: <https://doi.org/10.1088/1361-6560/abaa28>.
- 1558 [10] Fabio Di Martino et al. “FLASH Radiotherapy With Electrons: Issues Related to
1559 the Production, Monitoring, and Dosimetric Characterization of the Beam”. In:
1560 *Frontiers in Physics* 8 (2020). ISSN: 2296-424X. DOI: [10.3389/fphy.2020.570697](https://doi.org/10.3389/fphy.2020.570697).
1561 URL: <https://www.frontiersin.org/articles/10.3389/fphy.2020.570697>.
- 1562 [11] M. Dyndal et al. “Mini-MALTA: Radiation hard pixel designs for small-electrode
1563 monolithic CMOS sensors for the High Luminosity LHC”. In: (2019). DOI: <https://doi.org/10.1088/1748-0221/15/02/p02005>.
- 1565 [12] M. Barbero. “Radiation hard DMAPS pixel sensors in 150 nm CMOS technology
1566 for operation at LHC”. In: (2020). DOI: <https://doi.org/10.1088/1748-0221/15/05/p05013>.
- 1568 [13] K. Moustakas et al. “CMOS Monolithic Pixel Sensors based on the Column-Drain
1569 Architecture for the HL-LHC Upgrade”. In: (2018). DOI: <https://doi.org/10.1016/j.nima.2018.09.100>.

- 1571 [14] I. Caicedo et al. “The Monopix chips: depleted monolithic active pixel sensors with
1572 a column-drain read-out architecture for the ATLAS Inner Tracker upgrade”. In:
1573 (2019). DOI: <https://doi.org/10.1088/1748-0221/14/06/C06006>.
- 1574 [15] D. Kim et al. “Front end optimization for the monolithic active pixel sensor of the
1575 ALICE Inner Tracking System upgrade”. In: *JINST* (2016). DOI: doi:10.1088/
1576 1748-0221/11/02/C02042.
- 1577 [16] L. Pancheri et al. “A 110 nm CMOS process for fully-depleted pixel sensors”. In:
1578 (2019). DOI: <https://doi.org/10.1088/1748-0221/14/06/c06016>.
- 1579 [17] L. Pancheri et al. “Fully Depleted MAPS in 110-nm CMOS Process With 100–300-
1580 um Active Substrate”. In: (2020). DOI: 10.1109/TED.2020.2985639.